QUANTUM SIMULATION OF THE PERIODIC QUANTUM RABI MODEL AT DEEP STRONG COUPLING

Dissertation
zur
Erlangung des Doktorgrades (Dr. rer. nat.)
der
Mathematisch-Naturwissenschaftlichen Fakultät
der
Rheinischen Friedrich-Wilhelms-Universität Bonn

vorgelegt von

Geram Hunanyan

aus
Jerewan, Armenien

Bonn 2023

Angefertigt mit der Genehmigung der Mathematisch-Naturwissenschaftlichen Fakultät
der Rheinischen-Friedrich-Wilhelms-Universität Bonn

1. Gutachter: Prof. Dr. Martin Weitz
2. Gutachter: Prof. Dr. Michael Köhl

Tag der Promotion: 05.12.2023
Erscheinungsjahr: 2024

Abstract

The quantum Rabi model (QRM) stands as perhaps the most fundamental framework describing qubit-light interaction. While observations of many experiments can already be described within the Jaynes-Cummings model, which represents the limit of the quantum Rabi model in the weak coupling regime, establishing experimental investigations for high coupling strengths, where the full Hamiltonian has to be considered, remains a challenge. This is most prominent for the case of deep strong coupling, where the coupling strength between the qubit and the light field is the dominating energy in the system, giving rise to counter-intuitive effects such as creating excitations out of the vacuum.

In this work, experiments realizing a quantum simulation of the periodic quantum Rabi model (pQRM), which is a generalization of the original quantum Rabi model applicable to cold atoms in a periodic lattice potential, are reported. A bosonic field mode is realized by the harmonic trapping potential of an optical dipole trap for ultra-cold rubidium atoms, and a qubit two-level system is encoded in the Bloch band structure of a superimposed optical lattice potential. Overlaying these two potentials onto a rubidium Bose-Einstein condensate induces a coupling strength equivalent to 6.5 times the characteristic energies within the system. The mapping between the two systems becomes evident through the introduction of the Bloch ansatz, where the experimentally simulated system within the first Brillouin zone fully reflects the dynamics of the quantum Rabi model. However, stepping beyond this range gives rise to a quantum simulation of a periodic variant of the quantum Rabi model (pQRM), which constitutes the central focus of this thesis. At long interaction times, collapse and revival of the excitation number, as well as a revival of the initial state are experimentally observed.

The reported quantum simulation of the periodic quantum Rabi model demonstrates the phase-coherence of Schrödinger cat-like states far in the deep strong coupling regime. Interestingly, the realized Hamiltonian maps onto superconducting fluxonium qubit systems. Further prospects of this work include applications in atom-based quantum information processing.

Publications

Quantum Rabi Dynamics of Trapped Atoms Far in the Deep Strong Coupling Regime
J. Koch, G. Hunanyan, T. Ockenfels, E. Rico, E. Solano and M. Weitz
Nature Communications **14** (2023), p. 954, (doi.org/10.1038/s41467-023-36611-z)

Periodic Quantum Rabi Model with Cold Atoms at Deep Strong Coupling
G. Hunanyan, J. Koch, S. Moll, E. Rico, E. Solano and M. Weitz
Submitted for publication (arXiv:2307.06956v1)

Contents

Introduction

The first description of matter-field interaction was introduced as the semi-classical Rabi model by Isidor Isaac Rabi in the year 1936 [1, 2], where the interaction between a rapidly varying weak magnetic field and the orientation of an atom possessing a nuclear spin was described. Four years later, the so called Bloch-Siegert shift [3], named after Felix Bloch and Arnold Siegert, was introduced for an alternating field shifting the resonance of the two-level system.

A full quantum mechanical picture, where both the two-level system and the field mode are quantized, was put forward in the year 1963 by Edwin Thompson Jaynes and Fred Cummings [4], where in addition to the phenomena of so-called Rabi oscillations [5], which can be explained using the semi-classical approach, pure quantum mechanical effects such as the collapse and revival of the qubit's eigenstate are explained [6, 7]. The Jaynes-Cummings model (JCM), which in fact is a special case describing the so called *strong coupling* regime (SC) of the more general quantum Rabi model (QRM), is valid when the coupling strength between atoms and the electromagnetic field is larger than the decoherence rate, predicting the emergence of hybrid matter-light eigenstates [8–14]. Other than the Jaynes-Cummings model, the more general quantum Rabi model is valid for all coupling regimes. When the coupling strength becomes comparable or even exceeds the driving field frequency, the rotating wave approximation (RWA) breaks down and additionally to the co-rotating terms also the counter-rotating terms (CRT) have to be included. It is here, where despite its simplicity, the analytical solution of the full quantum Rabi model was not discovered for a long time [15], which includes counter-intuitive effects such as an excitation creation out of the vacuum. Taking into account the parity symmetry of the system, an analytical solution for the quantum Rabi model was achieved in 2011 by Daniel Braak [16]. The resulting coupling regimes are typically classified based on the relative coupling strength, which is obtained by dividing the coupling strength by the harmonic field frequency.

With increasing coupling between the field mode and the two-level system, one moves beyond the strong coupling regime and enters the *ultrastrong coupling* regime (USC), where various experimental realizations show the counter-rotating term's influence on to the system dynamics [17–21]. If the coupling strength is further increased to dominate all energies within the system, the so called *deep strong coupling* regime (DSC), which is known and characterized by the prominent role of counter-rotating terms in driving the system's dynamics [13, 22]. Experimentalists are just starting to explore this extreme parameter regime, where the drastic rise of excitation numbers in prepared vacuum states [23–26] is predicted. Recent experimental work in our group, reports coupling strengths which encompass 6.5 times the driving field mode, marking the highest experimentally realized *perturbative* deep strong coupling regime (pDSC), where among other observables, collapse and revival patterns of initially prepared vacuum states have been demonstrated [27, 28].

Quantum Simulation Using Quantum Systems

"Nature isn't classical, dammit, and if you want to make a simulation of nature, you'd better make it quantum mechanical, and by golly, it's a wonderful problem, because it doesn't look so easy." - being a quote from Richard Feynman in the year of 1981 [29], lays the main idea behind quantum simulation using a system which operates based on the principles of quantum mechanics itself. In the currently researched field of quantum physics, this idea finds representation through a plethora of quantum systems. These systems span a wide spectrum, encompassing trapped ion systems [30–33], superconducting qubits [34–38], quantum dots [39–43], photonic Bose-Einstein condensates (pBEC) [44], and neutral atoms in optical lattices [45–48].

Among these, neutral atoms in optical lattices, which are used in this work as a platform for quantum simulation, stand out as a powerful tool due to their experimental controllability and versatile applications. In this approach, the atoms are cooled to a degenerate quantum state and loaded into periodic potentials. Such systems offer the capability to simulate a wide array of quantum phenomena, ranging from condensed matter systems [49] to phenomena like superfluidity and the Mott insulator transition [50], as well as non-equilibrium quantum dynamics [51].

In this work, the motion of ultra-cold rubidium atoms is examined under the influence of a combined harmonic and periodic potential. This setup serves as a quantum simulation of Rabi dynamics, operating well within the deep strong coupling regime, where the coupling strength encompasses 6.5 times the driving field mode. The experimental approach involves the harmonic potential of an employed optical dipole trap simulating the driving field mode. Additionally, an optical four-photon lattice [52] is utilized, where its dispersion relation contributes to the formation of a qubit within the two lowest bands. Using this configuration, it becomes feasible to achieve an analog realization of the quantum Rabi model, where the optical dipole trap's far-off-resonance laser frequency is utilized to create a deep potential with minimal scattering effects and the optical lattice potential's tunability spans across five orders of magnitude. A distinction must be made here regarding the observed time in quantum simulation. When the dynamics are confined within the so-called first Brillouin zone, a good agreement with the predicted model can be found [27]. Exiting this limit leads to the emergence of a periodic variant of the quantum Rabi model [28]. Previous work concerning short interaction times, where both models coincide, has been realized within the framework of J. Koch's doctoral thesis [53], while the present study focuses on long interaction times beyond the range of the first Brillouin zone, where the periodic quantum Rabi model (pQRM) applies.

Analyzing the atom trajectories enables the extraction of various observables, such as expectation values of the mean position, mean momentum and the resulting bosonic excitation number, which are now also conducted for longer interaction times. Furthermore, by surpassing sub-cycle temporal dynamics and achieving coupling strengths realized in our analog setup, a measurement of collapse and revival patterns in an initially prepared vacuum state in quantum Rabi dynamics is demonstrated for the first time.

Structure of the Thesis

In this doctoral thesis, following this introductory chapter, a theoretical description of the basic principles of Bose-Einstein condensation is given. Subsequently, magneto-optical trapping and forced evaporation cooling in optical dipole traps is introduced as experimental methods to reach quantum degeneracy. Lastly, theoretical foundations for ultra-cold neutral atoms in optical lattice potentials are introduced, where the dispersion relation of multi-photon lattices is derived.

In the second theoretical chapter, the quantum Rabi Hamiltonian is introduced, including a spectral classification of the model, which reveals different regimes of the system. Subsequently, the quantum Rabi Hamiltonian is derived from the experimental system Hamiltonian using the Bloch ansatz. Is is at this point, where restricting the temporal dynamics in the experiment to the first Brillouin zone, successfully describes the (usual) quantum Rabi model, while on the other hand, when this limitation is lifted and longer interaction times are observed, the systems dynamics are described by the periodic quantum Rabi model, exceeding the first Brillouin zone. To illustrate similarities and differences between these two models, numerical simulations are used to showcase various observables, including the bosonic excitation number. At last, a digression into superconducting qubit systems is performed, where it is shown, that the system Hamiltonian can be directly mapped onto a fluxonium system.

After introducing the theoretical framework of this thesis, an overview of the experimental apparatus is provided. This includes a detailed presentation of the experimental setup, encompassing the ultra-high vacuum chamber, the magneto-optical trap, the single focused optical dipole trap, and the optical lattice setup. The section concludes by presenting the experimental cycle employed for the creation and manipulation of a rubidium Bose-Einstein condensate.

The last chapter, encompassing the experimental results of the quantum simulation, is divided into two sections. The first section involves characterization measurements of the optical dipole trap's oscillation frequency and the Bloch oscillations between momentum states, which resemble the qubit frequency of the two-level system. Given the extended interaction times observed, coherence characteristics are examined using a generalized scheme of a Ramsey-Bordé interferometer. By incorporating these preparatory measurements the characteristic expectation values of the quantum Rabi dynamics become observable. Notably, the emergence of collapse and revival patterns for an initially prepared vacuum state, superimposed with varying strengths of the qubit splitting, is considered as evidence for the presence of deep strong coupling.

Finally a summary along with an outlook concludes this thesis.

CHAPTER 1

Ultra-cold Atoms in Optical Lattice Potentials

This chapter contains theoretical principles relevant for the generation of an atomic Bose-Einstein condensate (BEC). Following the approach of many textbooks on statistical mechanics [54], first the phase transition of a non-interacting dilute atomic gas is described, and then extended to a model with weak atom-atom interactions by introducing the Gross-Pitaevskii equation and the Thomas-Fermi approximation [55, 56]. Subsequently, the theoretical principles for the experimental methods, such as implemented magneto optical trapping and evaporative cooling to reach the critical parameters will be presented. As a concluding part of the chapter, a brief overview of the generation of two- and four-photon lattices is given.

1.1 Principles of Bose-Einstein Condensation

In nature the distinction between *fermions*, which have half-integer values of spin, obeying the Pauli exclusion principle, where no two fermions can occupy the same quantum state simultaneously and *bosons*, which have integer values of spin and exhibit collective behavior at low temperatures has important implications for many physical quantum phenomena. Bose-Einstein condensation occurs when the macroscopic occupation of the ground state reaches a critical phase space density [57, 58]. While for a low dimensional photonic gas this can be achieved by increasing the number of light particles in the system [44], for atomic ensembles the transition is usually achieved by reaching the critical temperature, upon which the lowest state is then macroscopically populated.

1.1.1 The Non-interacting Bose Gas

In the following the equilibrium properties of a trapped non-interacting Bose gas will be discussed based on the concepts and insights in [56]. For this the mean occupation number of a single-particle state ν is described by the Bose distribution function:

$$\langle n(\varepsilon_\nu) \rangle = \frac{1}{e^{\beta(\varepsilon_\nu - \mu)} - 1} = \frac{1}{\zeta^{-1} e^{\beta \varepsilon_\nu} - 1} \tag{1.1}$$

Here, $\beta = {}^{1}\!/_{k_B T}$ is the inverse thermal energy including the Boltzmann constant k_B and the temperature T, ε_ν denotes the energy of the single-particle state and μ the chemical potential. Rewriting equation (1.1) in terms of the fugacity $\zeta = e^{\beta\mu}$ enables the characterization of different regimes of the distribution. The non-physical case of $\langle n(\varepsilon_\nu) \rangle < 0$ leads to a lower limit for the ground state energy $\varepsilon_0 > \mu$, hence implying $\zeta > 0$ for all energies

ε_ν. Considering the case for high temperatures, meaning $\zeta \to 0$, equation (1.1) transforms to the classical Boltzmann distribution:

$$\langle n(\varepsilon_\nu)\rangle \simeq e^{-\beta\varepsilon_\nu} \tag{1.2}$$

The opposite case for low temperatures, where $\zeta \to 1$, the Bose-Einstein distribution transforms into $\langle n_0\rangle = {}^1\!/\!{}_{(\zeta^{-1}-1)}$. In the following, quantities for a non-interacting BEC consisting of particles trapped in a non-isotropic harmonic potential

$$U(\mathbf{r}) = \frac{1}{2}m(\omega_x^2 x^2 + \omega_y^2 y^2 + \omega_z^2 z^2) \tag{1.3}$$

will be presented, where m depicts the particles mass and $\omega_x, \omega_y, \omega_z$ represent respective trap frequency components. The corresponding energy spectrum of the harmonic oscillator

$$\varepsilon_\nu = \varepsilon_{n_x,n_y,n_z} = \hbar(n_x\omega_x + n_y\omega_y + n_z\omega_z) + \varepsilon_0, \tag{1.4}$$

where $\varepsilon_0 = {}^1\!/\!{}_2\hbar(\omega_x + \omega_y + \omega_z)$ denotes the ground state energy, can be deployed into equation (1.1) and gives rise to the total atom number $N = \sum_\nu \langle n(\varepsilon_\nu)\rangle$ consisting of the ground state population N_0 and the thermal population in the excited states N_{th}

$$N = N_0 + N_{\text{th}} = \langle N_0\rangle + \sum_{n_x,n_y,n_z\neq 0} \frac{1}{e^{\beta\varepsilon_{n_x,n_y,n_z}} - 1}. \tag{1.5}$$

If $\hbar\bar{\omega} \ll k_B T$, an integral can be used for the equation above, yielding

$$N_{\text{th}} = \zeta(3)\left(\frac{k_B T}{\hbar\bar{\omega}}\right)^3 \tag{1.6}$$

where $\zeta(3) \approx 1.2$ is the Riemann ζ function and $\bar{\omega} = (\omega_x\omega_y\omega_z)^{1/3}$ depicts the harmonic oscillator frequency. For the case that $N = N_{\text{th}}$ the critical temperature T_c^0 (visualization in Figure 1.1) can be calculated to

$$T_c^0 = \frac{\hbar}{k_B}\bar{\omega}\left(\frac{N}{\zeta(3)}\right)^{1/3} = 0.94\frac{\hbar}{k_B}\bar{\omega}N^{1/3}. \tag{1.7}$$

Another quantity, which can be derived from equation (1.6) is the condensate fraction $\eta = {}^{N_0}\!/\!{}_N = {}^{(N-N_{\text{th}})}\!/\!{}_N$

$$\eta = 1 - \left(\frac{T}{T_c^0}\right)^3, \tag{1.8}$$

which from an experimentalists perspective is particularly interesting, since combining the measurement of η and the atom number N directly yields the temperature from equation (1.7).

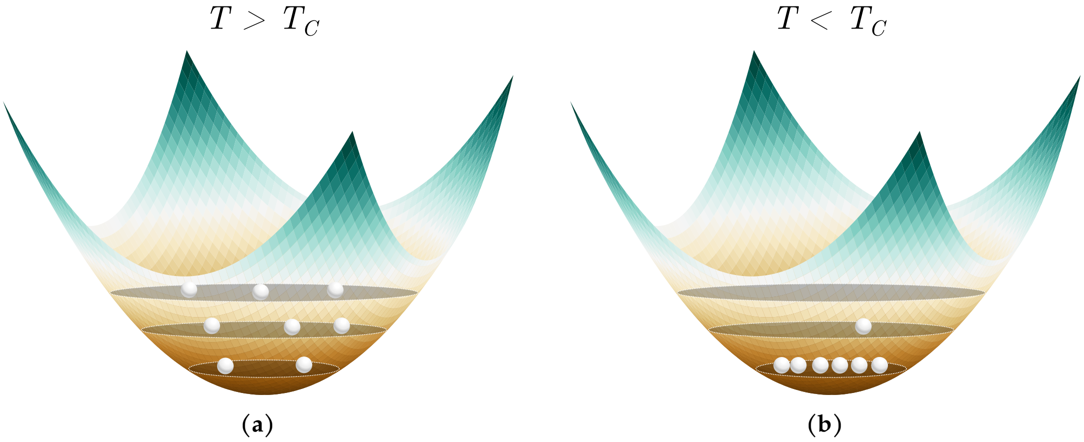

Figure 1.1: Schematic occupation distribution of a Bose-gas in a harmonic potential with the energy splitting depicted as gray planes. For the case of $T > T_C$ (a) the majority of atoms occupy higher energetic states, where for reaching the threshold of $T < T_C$ (b) a macroscopic occupation of the ground state occurs.

1.1.2 Introducing the Role of Interactions

After using the single particle picture to describe the critical temperature and condensate fraction for a non-interacting gas, the systems dynamics is expanded by introducing interactions between a pair of bosons at position **r** and **r′**. The following many-body Hamiltonian in second quantization [55] writes as

$$\begin{aligned}\hat{H}_{\mathrm{BB}} &= \int d\mathbf{r}\hat{\Psi}^\dagger(\mathbf{r},t)\left(-\frac{\hbar^2}{2m}\Delta + U(\mathbf{r})\right)\hat{\Psi}(\mathbf{r},t)\\ &+\frac{1}{2}\int\int d\mathbf{r}d\mathbf{r}'\hat{\Psi}^\dagger(\mathbf{r},t)\hat{\Psi}^\dagger(\mathbf{r}',t)\hat{V}_{\mathrm{int}}(\mathbf{r}-\mathbf{r}')\hat{\Psi}(\mathbf{r},t)\hat{\Psi}(\mathbf{r}',t),\end{aligned}\tag{1.9}$$

where, $\hat{\Psi}^\dagger(\mathbf{r},t)$ and $\hat{\Psi}(\mathbf{r},t)$ are creation and annihilation field operators and $\hat{V}_{\mathrm{int}}(\mathbf{r}-\mathbf{r}')$ denotes the interaction potential of a pair of bosons. The Heisenberg equation yields the time evolution of the field operators

$$i\hbar\frac{\partial}{\partial t}\hat{\Psi}(\mathbf{r},t) = \left[\hat{\Psi}(\mathbf{r},t),\hat{H}_{\mathbf{BB}}\right].\tag{1.10}$$

Using a mean field approach as introduced in [59], enables the analytical calculation of the ground state properties to describe the superfluidity of a weakly interacting BEC, where the field operator is decomposed into energy modes ν

$$\hat{\Psi}(\mathbf{r},t) = \sum_\nu \psi_\nu(\mathbf{r},t)\hat{a}_\nu\tag{1.11}$$

with $\hat{a}_\nu$ being the annihilation operator for a particle in the mode ν and the single particle wave function $\psi_\nu(\mathbf{r},t)$. When the ground state is populated, the creation- and annihilation operators $\hat{a}_0$ and $\hat{a}_0^\dagger$ can be well approximated by the ground state occupation number N_0 as $\hat{a}_0^\dagger = \hat{a}_0 = \sqrt{N_0}$. With this, equation (1.11) transforms into $\hat{\Psi}(\mathbf{r},t) = \sqrt{N_0}\psi_0(\mathbf{r},t) + \sum_{\nu\neq 0}\psi_\nu(\mathbf{r},t)\hat{a}_\nu$, where the ground- and excited state's wave functions are separated into two terms.

1.1.3 The Gross-Pitaevskii Equation

Moving on further characterization of the dynamics of the BEC, based on [55, 60, 61] the Gross-Pitaevskii equation will be presented. Decomposing the field operator $\hat{\Psi}(\mathbf{r},t)$ into a complex function, which denotes the condensate wave function with the condensate density equation $n_0(\mathbf{r},t) = |\Phi(\mathbf{r},t)|^2$ yields

$$\hat{\Psi}(\mathbf{r},t) = \Phi(\mathbf{r},t) + \hat{\Psi}', \tag{1.12}$$

where $\hat{\Psi}'$ is a perturbation term describing the condensates excitation. For low temperatures this term can be neglected and equation (1.9) can be simplified to a nonlinear Schrödinger equation [55]

$$i\hbar\frac{\partial}{\partial t}\Phi(\mathbf{r},t) = \left(-\frac{\hbar^2}{2m}\Delta + U(\mathbf{r}) + \int \hat{V}_{\text{int}}(\mathbf{r}-\mathbf{r}')|\Phi(\mathbf{r}',t)|^2)\right)\Phi(\mathbf{r},t). \tag{1.13}$$

Applying the s-wave limit [62], which simplifies the interaction potential $\hat{V}_{\text{int}} = g\delta(\mathbf{r}-\mathbf{r}')$ to the mean-field shift $g|\Phi(\mathbf{r},t)|^2$, the Gross-Pitaevskii equation (GPE) can be written as

$$i\hbar\frac{\partial}{\partial t}\Phi(\mathbf{r},t) = \left(-\frac{\hbar^2}{2m}\Delta + U(\mathbf{r}) + g|\Phi(\mathbf{r},t)|^2\right)\Phi(\mathbf{r},t). \tag{1.14}$$

Separating the mean field $\Phi(\mathbf{r},t) = \phi(\mathbf{r})e^{-i\mu t/\hbar}$, where $\phi(\mathbf{r})$ is the ground state wave function, normalized to the condensate particle number $N_0 = \int d\mathbf{r}|\phi(\mathbf{r})|^2$ and the exponential term denotes the time evolution with the ground state energy μ, the GPE transforms into its time-independent form

$$\left(-\frac{\hbar^2}{2m}\Delta + U(\mathbf{r}) + g|\phi(\mathbf{r})|^2\right)\phi(\mathbf{r}) = \mu\phi(\mathbf{r}) \tag{1.15}$$

Due to the nonlinear nature of $g|\phi(\mathbf{r},t)|^2$, in general, the solution of this equation is done numerically. As a final step the ground state wave function can be rewritten in terms of the condensate's density distribution $n_0(\mathbf{r}) = |\phi(\mathbf{r})|^2$, yielding a comprehensive form of the GPE

$$\begin{aligned} E(n_0) = \mu &= \int d\mathbf{r}\left(-\frac{\hbar^2}{2m}\Delta n_0(\mathbf{r}) + U(\mathbf{r})n_0(\mathbf{r}) + \frac{g}{2}n_0(\mathbf{r})^2\right) \\ &= E_{\text{kin}} + E_{\text{pot}} + E_{\text{int}}. \end{aligned} \tag{1.16}$$

Here, the first term describes the kinetic energy, also referred to as *quantum pressure*, while the second and third term denote the potential- and interaction energy in the system.

1.1.4 Large Condensates: The Thomas-Fermi Approximation

Increasing the atom number or the interaction strength decreases the influence of the kinetic energy E_{kin}. In this limit, when the kinetic energy is neglected, the Thomas-Fermi approximation applies [55].

$$\frac{E_{\mathrm{int}}}{E_{\mathrm{kin}}} \propto \frac{N_0|a|}{a_{\mathrm{ho}}} \gg 1. \tag{1.17}$$

Here, a denotes the scattering length (attractive: $a < 0$, repulsive: $a > 0$) and $a_{\mathrm{ho}} = \sqrt{\hbar/m\bar{\omega}}$ describes the radius of a non-interacting wave packet in the ground state of the harmonic oscillator potential. An analytical expression in terms of the condensate density distribution can be written as [55]:

$$n_0(\mathbf{r}) = \begin{cases} \frac{1}{g}\left(\mu - U(\mathbf{r})\right) & \text{where } \mu - U(\mathbf{r}) \geq 0 \\ 0 & \text{else} \end{cases} . \tag{1.18}$$

Considering the normalization condition $N_0 = \int d\mathbf{r} n_0(\mathbf{r})$ the chemical potential writes as

$$\mu = \frac{\hbar\bar{\omega}}{2}\left(15\frac{Na}{a_{\mathrm{ho}}}\right)^{2/5} \tag{1.19}$$

where the external potential $U(\mathbf{r}) = \mu$ equals the chemical potential.
The Thomas-Fermi radii are defined as

$$R_i = \sqrt{\frac{2\mu}{m\omega_j^2}}, \tag{1.20}$$

which scales with increasing particle number N_0. It is important to note, that only within the edges of the BEC, this approximation is true, since at these areas the kinetic energy E_{kin} can not be neglected any longer.

1.2 Experimental Realization of Bose-Einstein Condensates

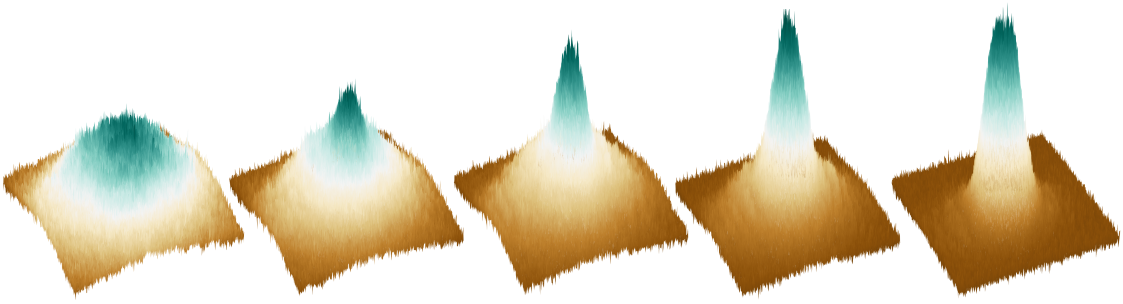

After providing a brief overview of the theoretical background of Bose-Einstein condensation, this section describes its experimental realization and the methods employed to reach the critical temperature for the condensation threshold. While conventional cooling techniques, such as dilution cooling in dilution refrigerators [63], can effectively lower temperatures to the millikelvin range, they fall short of reaching the lower nanokelvin temperatures essential for the occurrence of the desired phase transition. For this purpose, a combination of laser cooling and magnetic trapping is employed to create a magneto-optical trap (MOT), pre-cooling the atoms to a few hundred millikelvin. Subsequently, the atomic sample, having reached a sufficiently low temperature, is loaded into a conservative optical dipole trap to undergo further forced evaporative cooling. This approach, widely employed in numerous experiments, enables the attainment of sufficiently low temperatures, and with significant effort, even reaching the picokelvin regimes [64, 65]. The whole experimental scheme is realized in an ultra-high vacuum chamber, ensuring low collision rates with background gas, which would otherwise cause large atom losses. The following subsections will present the properties of each mentioned cooling mechanism.

1.2.1 Pre-cooling Atoms in a MOT

A magneto-optical trap combines the Doppler cooling mechanism, first time proposed by T. Hänsch and A. L. Schawlow in 1975 [66], later experimentally realized in a three dimensional setup by Chu et al. in 1985 [67], and magnetic trapping of atoms, which allows for efficient confinement of the cooled atoms in a localized region. Considering a simplified two-level atom, consisting of a ground state energy E_g and an excited state energy E_e, and exposed to a laser beam slightly detuned from the atomic transition $E_{\mathrm{ph}} < \Delta E = E_e - E_g$, a momentum gain $\mathbf{p} = \hbar\mathbf{k}$ occurs as a result of absorbing the photon's energy $E_{\mathrm{ph}} = \hbar\omega_{\mathrm{ph}}$, causing the atomic excitation. Here the absolute value of the wave vector is $|\mathbf{k}| = k = {}^{\hbar\omega_{\mathrm{ph}}}/_{c}$, with c as the speed of light. While this absorption of a photon is a directed process, the relaxation of the atom to its ground state takes place in a random direction via spontaneous emission, as seen in Figure 1.2 (C). The isotropic nature of this mechanism results in, on average, a directed momentum transfer occurring due to numerous absorption and re-emission cycles. In addition, a red shift is implemented onto the laser beam, causing only atoms which are moving towards the photons to be addressed by the cooling process. In a usual setup, three counter-propagating pair of beams are used to slow down atoms

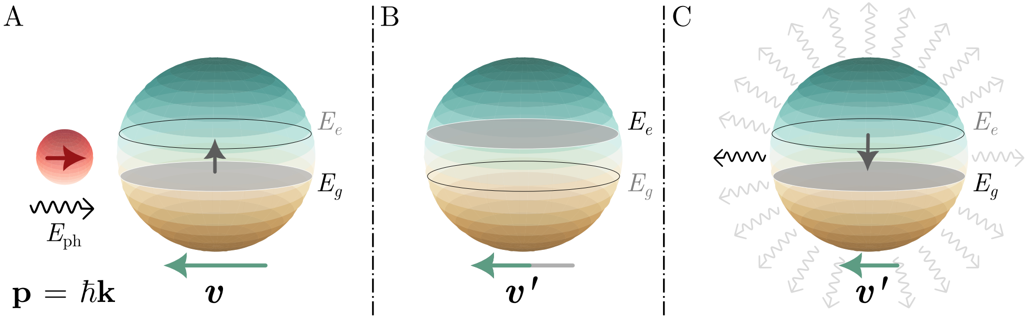

Figure 1.2: Basic principle of Doppler cooling simplified to a one dimensional case for a two level atom. Atoms moving with a velocity of v towards a red detuned laser light can be excited to the upper state by absorbing a photon (red sphere) with a momentum $\mathbf{p} = \hbar\mathbf{k}$ (A to B). While the absorption of the photon is directed, the emission is isotropic leading to a net momentum transfer from one direction (C).

in the intersection region, reducing their kinetic energy, nevertheless failing to trap the cooled atoms in a localized region.

In order to confine the atoms to the cooling region, a magnetic trapping potential is added, for which the laser beams of the Doppler cooling mechanism are circularly polarized in order to drive different m_F transitions. A pair of anti-Helmholtz coils is commonly used to generate a quadrupole field creating a magnetic gradient which is zero in the center of the trap (as seen in Figure 1.3(a)). When atoms leave the center of the trap, the atomic state degeneracy is lifted asymmetrically for respective absolute values of the magnetic field. Figure 1.3(b) shows the basic principle in one dimension for a simplified example of a two level system with an $F' = 1$ excited state, which in presence of a magnetic field, splits into three Zeeman states ($m_F = 0; \pm 1$). Moving to the positive side of the magnetic field ($B > 0$) lowers the $m_F = -1$ state, where due to the σ^- polarization the $\Delta m_F = -1$ transition becomes resonant. The opposite happens for atoms moving in the other direction, where σ^+ polarization and the $\Delta m_F = +1$ transition is utilized, consequently ensuring an effective force pushing atoms back to the cooling region.

As mentioned earlier, the rubidium atoms used in the experiment exhibit a more complex level scheme than the two-level system described above. Figure 1.4 illustrates the transitions used for atom cooling, revealing the need for two laser frequencies. Ideally, the cooling transition is a closed transition, meaning that after excitation only relaxation into the original state is possible, allowing for a large amount of excitation-relaxation cycles. In this case, the transition from $|5^2S_{1/2}, F = 2\rangle$ to $|5^2P_{3/2}, F' = 3\rangle$ is utilized. However, off-resonant excitation to the $|5^2P_{3/2}, F' = 2\rangle$ state and subsequent relaxation to the state $|5^2S_{1/2}, F = 1\rangle$, results in the loss of atoms for the cooling process. Therefore, an additional repumping frequency is required to transport the atoms back to the cooling process, by addressing the $|5^2S_{1/2}, F = 1\rangle$ to $|5^2P_{3/2}, F' = 2\rangle$ transition. One limitation for reachable temperatures in a magneto-optical trap is given by the natural linewidth Γ of the used cooling transition. The so called *Doppler temperature* $T_{\rm D} = \hbar\Gamma/2k_{\rm B}$ for the ^{87}Rb rubidium atoms in the experiment is calculated to be $T_{\rm D} = 145.57\,\mu\text{K}$ [69] and although methods such as *Sisyphus-* and *polarization gradient cooling* enables sub-Doppler regimes down

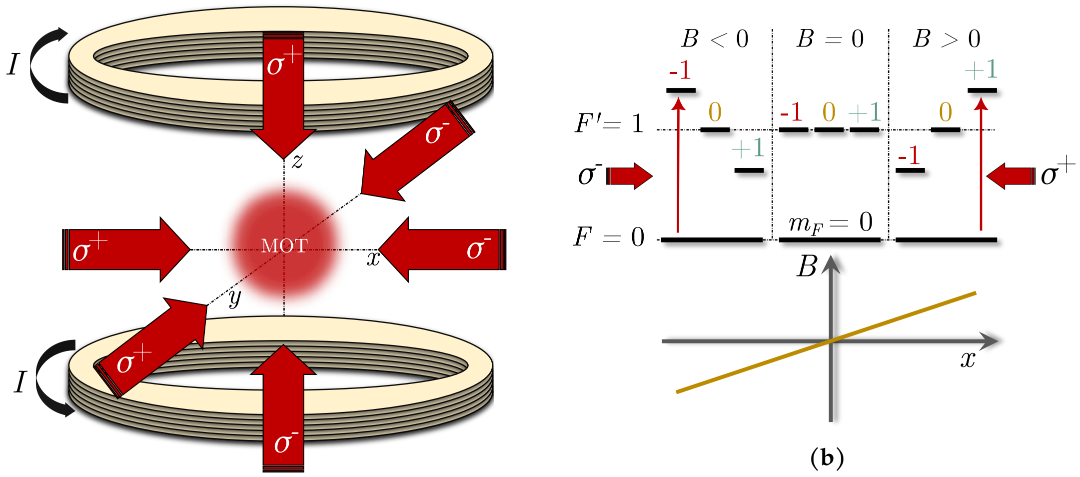

(a)

(b)

Figure 1.3: (a) Schematic setup of a magneto optical trap using two anti-Helmholtz coils and six counter-propagating laser beams with respective circular polarization $\sigma^{\pm}$. While the optical force of the laser beams slows the atoms (shown in Figure 1.2) the magnetic field, which is zero in the center, generates a positional dependent force, pushing atoms back to the crossing section of the cooling area. (b) Simplified level scheme of a two-level atom, where due to the Zeeman shift the $|F' = 1, m_F = 1\rangle$ state degeneracy is lifted in a respective manner depending on the magnetic field presented in one dimension below. For atoms moving to the right (left), the magnetic field is positive (negative), and the σ^+-polarized (σ^-) laser beams drive the respective $\Delta m_F = +1$ ($\Delta m_F = -1$) transition, hence pushing the atoms back to the trap center.

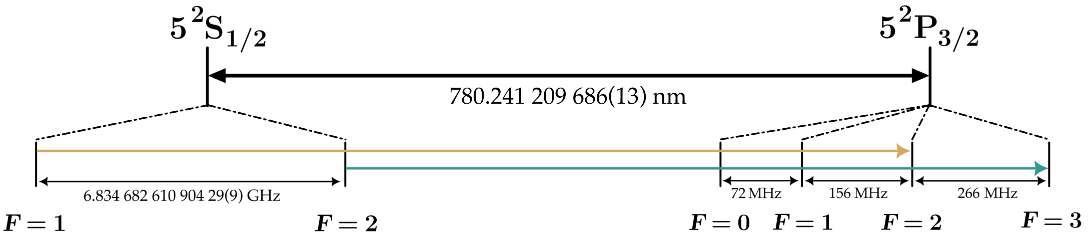

Figure 1.4: Rubidium-87 D2 transition (obtained from [68]), where the cooling laser transition $|5^2S_{1/2}, F = 2\rangle$ to $|5^2P_{3/2}, F' = 3\rangle$ is marked in green and the repumping transition $|5^2S_{1/2}, F = 1\rangle$ to $|5^2P_{3/2}, F' = 2\rangle$ is marked in yellow.

to the recoil temperature $T_{\mathrm{R}} = \hbar^2 k^2 / m_{\mathrm{Rb}} k_{\mathrm{B}} = 362\,\mathrm{nK}$ [70, 71], with m_{Rb} as the mass of the rubidium atom, the critical temperature for Bose-Einstein condensation is far out of reach. For this further cooling methods in form of forced evaporative cooling have to be implemented using conservative traps realized by a single focused optical dipole trap introduced in the next section.

1.2.2 Optical Dipole Trap

To overcome the mentioned temperature limitations and reach the condensation threshold, a conservative trap in the form of a far-off resonance optical dipole trap (FORT) is here utilized. In a magneto-optical trap, the Doppler cooling of atoms is achieved through a dissipative force generated by an absorption and spontaneous re-emission cycle. However, conservative traps for neutral atoms operate differently by creating a potential minimum that allows for the trapping of atoms.

There are essentially two types of traps that can be used for this purpose. This section presents the general functioning of a far-off resonance optical dipole trap, which, alongside magnetic traps, represents a conventional method for creating a Bose-Einstein condensate (BEC) with pre-cooled atomic ensembles. While magnetic traps utilize the magnetic dipole moment of neutral atoms, in the case of an optical dipole trap, the interaction between laser light and the atom induces an optical dipole moment resulting in the so-called *AC Stark shift* [72–74]. As described by Grimm et al. [75], a simple semi-classical approach for a two-level atom interacting with a classical light field can be used to describe the dipole force $\mathbf{F}_{\text{dip}} = -\nabla U_{\text{dip}}$, where U_{dip} is the resulting dipole potential with a depth of a few millikelvin. In order to account for the multilevel structure of the used alkali atoms a quantum mechanical *dressed state* ansatz will be presented, where both the atom and the light field are quantized.

Semi-classical Approach

During the interaction of atoms with highly detuned laser light, the mentioned dipole force arises due to the gradient field of the latter and the atomic dipole moment. The oscillating electric field of the laser light induces a dipole moment, which in turn re-interacts with the laser light. The electric field $\mathbf{E}(\mathbf{r},t)$ including the unit vector $\hat{\mathbf{e}}$ indicating the polarization direction, writes as

$$\mathbf{E}(\mathbf{r},t) = \hat{\mathbf{e}}\tilde{E}(\mathbf{r})e^{-i\omega t} + c.c., \tag{1.21}$$

with the corresponding dipole moment

$$\mathbf{p}(\mathbf{r},t) = \hat{\mathbf{e}}\tilde{p}(\mathbf{r})e^{-i\omega t} + c.c.. \tag{1.22}$$

The amplitudes $\tilde{E}$ and $\tilde{p}$ are related with the complex polarizability $\alpha(\omega)$

$$\tilde{p} = \alpha(\omega)\tilde{E}, \tag{1.23}$$

which is specific to the atom species and dependent on the driving frequency ω. For an isotropic medium, α can be described as a complex scalar (see [76] for validity in ^{87}Rb atoms). Using equation (1.23), the dipole potential U_{dip} can be calculated as a product of the dipole moment $\mathbf{p}$ and the electric field vector $\mathbf{E}$

$$U_{\text{dip}} = -\frac{1}{2}\langle\mathbf{pE}\rangle_t = -\frac{1}{2}\langle\alpha(\omega)E^2\rangle = -\frac{1}{2\varepsilon_0 c}\text{Re}(\alpha(\omega))I(\mathbf{r}). \tag{1.24}$$

The factor $-\frac{1}{2}$ stems from the presence of an induced dipole moment [75], while ε_0 is the electric field constant and with the speed of light c describes the field intensity $I = 2\varepsilon_0 c|\mathbf{E}|^2$. The parentheses represent the temporal averaging over the rapidly oscillating terms. The dipole potential U_{dip} is proportional to the light intensity I and the real part of the complex polarizability $\alpha(\omega)$. This describes the in-phase oscillating component of the dipole oscillation and is responsible for the dispersive interaction between the light field and the atomic dipole moment [75]. As a conservative potential, the dipole force can be written as

$$\mathbf{F}_{\text{dip}}(\mathbf{r}) = -\nabla U_{\text{dip}}(\mathbf{r}) = \frac{1}{2\varepsilon_0 c}\text{Re}(\alpha(\omega))\nabla I(\mathbf{r}), \tag{1.25}$$

while considering the fraction of the dipole moment, which is oscillating out of phase results in the absorbed power

$$P_{\text{abs}} = \langle \dot{\mathbf{p}}\mathbf{E}\rangle_t = 2\omega\text{Im}(\tilde{p}\tilde{E}^*) = \frac{\omega}{\varepsilon_0 c}\text{Im}(\alpha)I. \tag{1.26}$$

The corresponding scattering rate Γ_{sc}, which can be understood as a cycle of absorbing a photon with the energy $\hbar\omega$ and spontaneously re-emitting via dipole radiation is then

$$\Gamma_{\text{sc}} = \frac{P_{\text{abs}}}{\hbar\omega} = \frac{1}{\hbar\varepsilon_0 c}\text{Im}(\alpha)I(\mathbf{r}). \tag{1.27}$$

The geometric shape and photon scattering rate can be described by equations (1.25) and (1.27). These equations provide information about the potential shape and heating rate of the optical dipole trap and are connected, on the one hand, by the respective components of the complex polarizability $\alpha(\omega)$ and, on the other hand, by the spatially distributed field intensity of the laser beam $I(\mathbf{r})$.

This classical approach, grounded in the oscillator model proposed by H. Lorentz [77], describes the atom's electron, with a charge of e and a mass of m_e, as elastically connected to its core, where the eigenfrequency ω_0 corresponds to the atomic transition frequency. The electrons equation of motion can be written as a second order differential equation

$$\ddot{x} + \Gamma_\omega \dot{x} + {\omega^2}_0 x = -\frac{e}{m_e}E(t) \tag{1.28}$$

where due to the emission of energy by a circularly accelerated charge the system is damped [78]. Incorporating the Larmor-formula [79] the classical damping rate can be calculated to

$$\Gamma_\omega = \frac{e^2\omega^2}{6\pi\varepsilon_0 m_e c^3} \tag{1.29}$$

and with equation (1.23) the complex polarizability writes as

$$\alpha = \frac{e^2}{m_e} \frac{1}{{\omega_0}^2 - \omega^2 - i\omega\Gamma_\omega} = 6\pi\varepsilon_0 c^3 \frac{\Gamma/{\omega_0}^2}{{\omega_0}^2 - \omega^2 - i(\omega^3/{\omega_0}^2)\Gamma}. \tag{1.30}$$

Here, the on-resonance damping rate $\Gamma = \left({}^{\omega_0}/_{\omega}\right)^2 \Gamma_\omega$ has been introduced. With the above expression for the polarizability, the dipole potential U_{dip} (equation (1.24)) and scattering rate Γ_{sc} (equation (1.27)) can be calculated, where under the assumption that $\Gamma_\omega \ll \omega_0$ the terms proportional to $\left({}^{\Gamma}/_{\omega_0}\right)^2$ are neglected and lead to

$$U_{\text{dip}}(\mathbf{r}) = -\frac{3\pi c^2}{2{\omega_0}^3} \left(\frac{\Gamma}{\omega_0 - \omega} + \frac{\Gamma}{\omega_0 + \omega} \right) I(\mathbf{r}) \tag{1.31}$$

and

$$\Gamma_{\text{sc}}(\mathbf{r}) = \frac{3\pi c^2}{2\hbar{\omega_0}^3} \left(\frac{\omega}{\omega_0} \right)^3 \left(\frac{\Gamma}{\omega_0 - \omega} + \frac{\Gamma}{\omega_0 + \omega} \right)^2 I(\mathbf{r}). \tag{1.32}$$

Each equation above show two resonances, where besides the usual case for $\omega = \omega_0$, the case $\omega = -\omega_0$ also is present. As shown in [80], the latter is suppressed with assumption that the detuning $\Delta = |\omega - \omega_0| \ll \omega_0$ is a lot smaller than the driving frequency ω_0. For the case that $\omega/\omega_0 \approx 1$ equations (1.31) and (1.32) can be further simplified to

$$U_{\text{dip}}(\mathbf{r}) = \frac{3\pi c^2}{2{\omega_0}^3} \frac{\Gamma}{\Delta} I(\mathbf{r}) \tag{1.33}$$

and

$$\Gamma_{\text{sc}}(\mathbf{r}) = \frac{3\pi c^2}{2\hbar{\omega_0}^3} \left(\frac{\Gamma}{\Delta} \right)^2 I(\mathbf{r}). \tag{1.34}$$

The scattering rate Γ_{sc} and the optical dipole potential U_{dip} can be related with the following equation

$$\hbar\Gamma_{\text{sc}} = \frac{\Gamma}{\Delta} U_{\text{dip}} \tag{1.35}$$

providing two important insights into optical dipole traps. On the one hand, the sign of the detuning Δ plays a crucial role in determining the behavior of the system. Depending on whether the system is on the red-detuned side ($\Delta < 0$) or the blue-detuned side ($\Delta > 0$) of resonance, a dipole interaction based on the overlap between potential minimum and intensity distribution arises. Figure 1.5(a) shows the case of a negative detuning (red-detuned, $\Delta < 0$), where the potential minimum aligns with the intensity maximum, creating favorable trapping conditions. Conversely, with a positive detuning (blue-detuned, $\Delta > 0$), the opposite behavior shows, where atoms can be trapped in the intensity minimum (as seen in Figure 1.5(b)).

On the one hand, considering equations (1.33) and (1.34), it is observed that the dipole

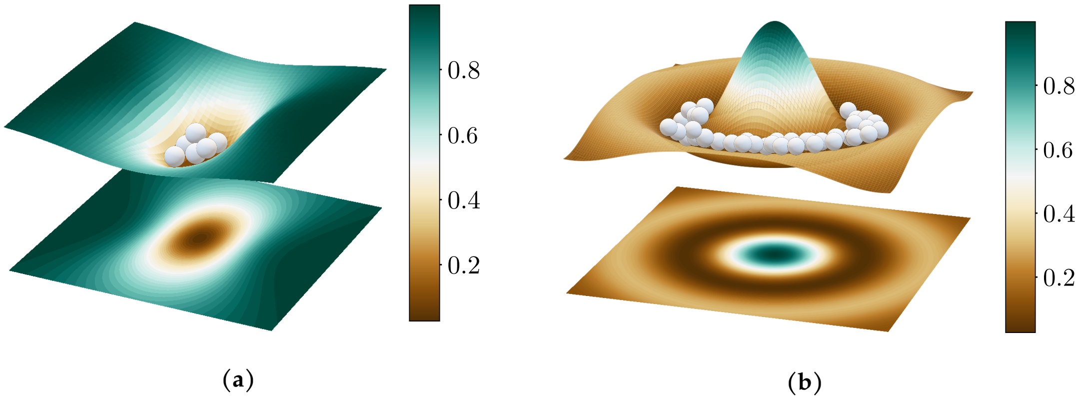

(a) (b)

Figure 1.5: (a) Visual representation of an optical potential, where the trapping laser frequency is red detuned ($\Delta < 0$) and the potential minimum overlaps with the intensity maximum. (b) The opposite case of a blue detuned ($\Delta > 0$) trap, for example realized with a so called *Mexican hat* potential, where the atoms (white spheres) are trapped at areas of low intensity. The color gradient represents the trapping region (brown).

trapping potential U_{dip}, which should ideally be maximized, is proportional to $^{I}/_{\Delta}$. On the other hand, the scattering rate Γ_{sc}, which should be minimized, is proportional to $^{I}/_{\Delta^2}$. Experimentally, low scattering rates with deep potentials are realized by implementing high laser powers with large detunings.

It should be emphasized that the atoms used in the experiment do not represent two-level systems but rather exhibit fine and hyperfine structures. However, if the detuning Δ is far enough from the fine and hyperfine level splittings ($\Delta \gg \Delta_{\text{FS/HFS}}$), these substructures are not resolved, and the two-level system approximation holds true. Nevertheless in the following the effects of fine- and hyperfine substructures will be included in a quantum mechanical dressed state system, showing ground-state light shifts for multi-level alkali atoms.

Dressed State Approach

The quantum mechanical dynamics of a multilevel atom in a far detuned optical light field can be described by second order time-independent perturbation theory acting on the interaction Hamiltonian $H_{\text{int}} = -\hat{\mu}\mathbf{E}$, with $\hat{\mu} = -e\mathbf{r}$ as the dipole operator and $\mathbf{E}$ the electric field. The resulting energy shifts ΔE_i write as

$$\Delta E_i = \sum_{i \neq j} \frac{|\langle j|H_{\text{int}}|i\rangle|^2}{\mathcal{E}_i - \mathcal{E}_j}, \tag{1.36}$$

where i denotes the number of energy levels in a multi-level atom and $\mathcal{E}_{i,j}$ represents the unperturbed energies in the system [81]. Other than in the given semi-classical approach above, now the sub-systems consisting of the atom and the light field are combined (*dressed*) to one quantum system, where in the ground state the atoms internal energy is zero and the field energy is $n\hbar\omega$, with n as the number of photons and $\mathcal{E}_i = n\hbar\omega$ depicts the total energy for the unperturbed state. It is easy to see, that upon absorbing a photon with the energy

$\hbar\omega_0$ the sum of atomic energy and field energy results $\mathcal{E}_j = \hbar\omega_0 + (n-1)\hbar\omega = -\hbar\Delta_{ij} + n\hbar\omega$, where the energy difference between the two states is $\mathcal{E}_i - \mathcal{E}_j = \hbar\Delta_{ij}$. Considering the two-level atom interaction Hamiltonian $H_1 = \mu E$, equation (1.36) simplifies to

$$\Delta E = \pm\frac{|\langle e|\mu|g\rangle|^2}{\Delta}|E|^2 = \pm\frac{3\pi c^2}{2{\omega_0}^3}\frac{\Gamma}{\Delta}I, \tag{1.37}$$

where $I = 2\varepsilon_0 c|\tilde{E}|^2$ and $\Gamma = {}^{{\omega_0}^3}\!/_{3\pi\varepsilon_0\hbar c^3}|\langle e|\mu|g\rangle|^2$ [75]. The positive and negative sign represent the two respective states of the atom, where the first shift, being the ground state energy, yields the dipole potential U_{dip} from equation (1.33), derived with the semi-classical approach. This optically induced shift is also called the AC Stark shift, and for the case of low saturation, offers a potential minimum for the motion of the atoms (as seen in Figure 1.6).

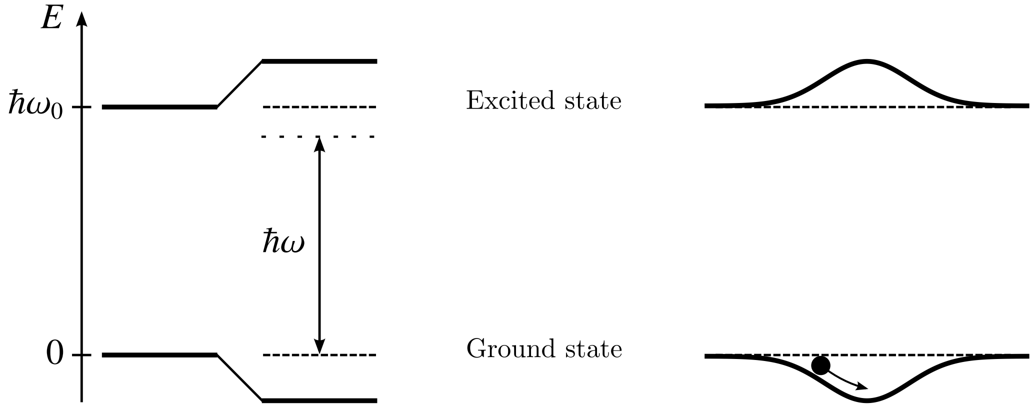

Figure 1.6: Visualization of the occurring AC stark shift. The dipolar interaction between atom and light induces a shift of the energetic levels proportional to the light fields intensity. For red detuning, the ground state of the atom is then lowered while the excited state is elevated. This visualization is taken and modified from [75].

Taking different weighting coefficients of dipole transitions and their respective detunings Δ_{ij}, contributing to the shift of the ground level, an analogous calculation for a more complex multi-level atom can be performed. The resulting dynamic Stark shift is obtained as the sum of the respective contributions ΔE_j from the different excitations of energy levels $\mathcal{E}_j$ [75]. In the case of ^{87}Rb rubidium atoms, with a nuclear spin of $I = 3/2$, the resulting $S \rightarrow P$ transition is a D-line doublet (as can be seen in Figure 1.4) including the fine structure splitting $\hbar\Delta_{\text{FS}}$ [82]. Since large detunings ($\Delta \gg \Delta_{\text{FS}}$) are chosen for the use in optical dipole traps, the effect of the much smaller hyperfine substructure can be usually neglected and the dipole potential for a multi-level atom writes as

$$U_{\text{dip}}(\mathbf{r}) = \frac{3\pi c^2}{2{\omega_0}^3}\frac{\Gamma}{\Delta}\left(1 + \frac{1}{3}\mathscr{P}g_F m_F\frac{\Delta_{\text{FS}}}{\Delta}\right)I(\mathbf{r}), \tag{1.38}$$

with the g-factor g_F, the magnetic quantum number m_F and $\mathscr{P}$ as the laser lights polarization for π-($\mathscr{P} = 0$) and $\sigma^{\pm}$-polarization ($\mathscr{P} = \pm 1$), respectively. Here, the zeroth order is identical to the two-level atom approximation, while the first order term depicts a much smaller dependency on the sub-level structures. In the experiment performed in this work, a linearly polarized ($\mathscr{P} = 0$) laser with $\lambda_{\mathrm{CO2}} = 10.6\,\mu\mathrm{m}$ ($\Delta_{\mathrm{FS}}/\Delta \approx 0.2$) is used, causing the correction factors to be negligible, hence making it valid to assume the two-level approximation for the dipole trapping potential.

1.2.3 Forced Evaporative Cooling

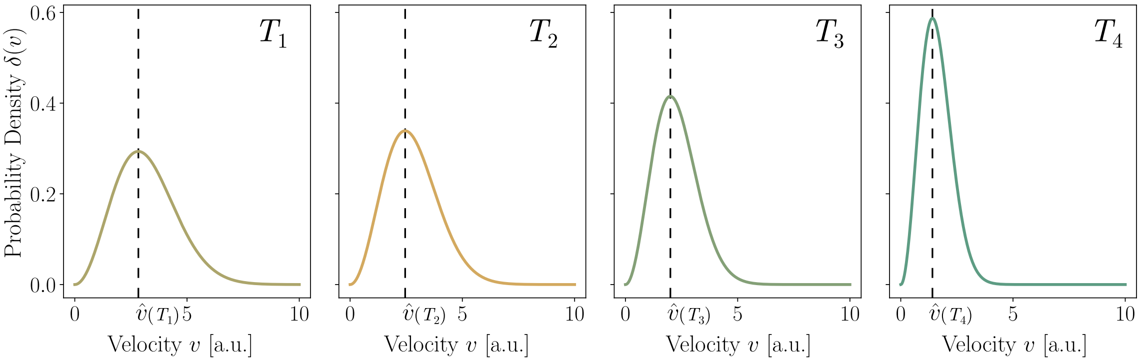

Figure 1.7: Exemplary representation of a Boltzmann distribution showing the probability density $\delta(v)$ against the velocity v for descending temperatures (from left to right $T_1 > T_2 > T_3 > T_4$). During evaporation of trapped atoms, the high energy tail of the thermal distribution gets 'cut off', when high-energetic atoms leave the trap, lowering the average velocity $\hat{v}$ after each re-thermalization process.

After discussing the main quantities involved in an optical dipole trap, the final step towards achieving a quantum degenerate state will be discussed here. The fundamental principle underlying evaporative cooling is the removal of high energetic atoms from the optical dipole trap, followed by the subsequent re-thermalization of the remaining atoms, first time realized in magnetic traps in 1987 [83] later demonstrated in crossed optical traps in 1997 [84].

This process effectively reduces the overall thermal velocity by truncating the high-energy tail of the Boltzmann distribution, as seen in Figure 1.7. This is clearly associated with significant atomic losses, which makes it essential to start the evaporation process with a high number of atoms in the dipole trap. In the case of magnetic traps, the excitation of atoms to non-confined Zeeman levels can be used to remove the highest energetic atoms. However, in the case of optical dipole traps, this is achieved by simply reducing the depth of the trapping potential. The process of *forced* evaporation occurs when the intensity of the beam is lowered, effectively flattening the geometry of the trap.

Preparing the atoms in the lowest energetic state suppresses inelastic collisions during the evaporation process [75]. In our case, this is achieved by preparing the rubidium atoms in the $|5^2S_{1/2}, F = 1\rangle$ state, which is explained in more detail in chapter 3. However, there is a natural limit where tightly confined traps allow for high atomic densities but result in limited trapping volumes, which restricts the number of particles that can be loaded into the trap. Conversely, decreasing the focus of the beam increases the area of the dipole trapping potential but at the cost of particle density and, therefore, elastic collision rates, which are needed for re-thermalization. In section 3.3, this challenge is overcome by an experimental method that increases the trapping region through spatial modulation of the dipole trapping laser beam.

1.3 Neutral Atoms in Optical Lattices

Optical lattices, formed by interfering laser beams, provide a versatile platform for studying a wide range of quantum phenomena. Specifically, periodic structures with regions of high and low intensity are created, trapping atoms and exhibiting behavior analogous to electrons in crystalline structures.

To begin with, the simplest case of a one-dimensional two-photon (standing wave) lattice is presented with a classical approach. This configuration involves two counter-propagating beams with the same linear polarization, forming a standing wave, which is utilized for Bragg-pulse preparation of different momentum states during the experimental cycle. Conversely, for generating a two-level system suitable for quantum Rabi simulations, a multi-photon lattice consisting of a four-photon process, is implemented resulting in a higher periodicity compared to a standing wave. Incorporating Bloch's theorem [85] the dispersion relations of each lattice will be presented, where the resulting band model shows an analogy to solid-state physics [86].

1.3.1 Two-photon Lattice Potential

Two counter-propagating, linear polarized beams with the same frequency $f = {}^{\omega}/_{2\pi}$ and respective propagation directions $\pm z$ form a standing wave, which for the red detuned case localize atoms in the intensity maximum (as can be seen in section 1.2.2) [87]. In this case, each beam can be described by a plane wave

$$\mathbf{E}_1(z,t) = E_1 \hat{\mathbf{e}}_1 \cos(\omega t + kz + \varphi_1) \tag{1.39}$$

$$\mathbf{E}_2(z,t) = E_2 \hat{\mathbf{e}}_2 \cos(\omega t - kz + \varphi_2). \tag{1.40}$$

Here, the phases φ_1 and φ_2 correspond to the respective beam and $k = {}^{2\pi}/_{\lambda}$ is the wave vector including the laser lights wavelength $\lambda = {}^{2\pi c}/_{\omega}$. Averaging over time results in the total intensity

$$\begin{aligned} I(z) &= c\varepsilon_0 \left\langle \mathbf{E}_{\text{tot}}^2 \right\rangle_t = c\varepsilon_0 \left\langle (\mathbf{E}_1 + \mathbf{E}_2)^2 \right\rangle_t \\ &= c\varepsilon_0 \left\langle \mathbf{E}_1^2 + \mathbf{E}_2^2 + 2\mathbf{E}_1\mathbf{E}_2 \right\rangle_t \\ &= I_1 + I_2 + I_{\text{int}}(z), \end{aligned} \tag{1.41}$$

where $I_{1/2} = {}^{1}/_{2} c\varepsilon_0 E_{1/2}$ corresponds to each beams intensity and the interference term $I_{\text{int}}(z)$ includes the orientation of the polarization vectors $\hat{\mathbf{e}}_{1/2}$ with the angle α

$$I_{\text{int}} = 2\sqrt{I_1 I_2} \cos(2kz + \varphi) \cdot \cos(\alpha), \tag{1.42}$$

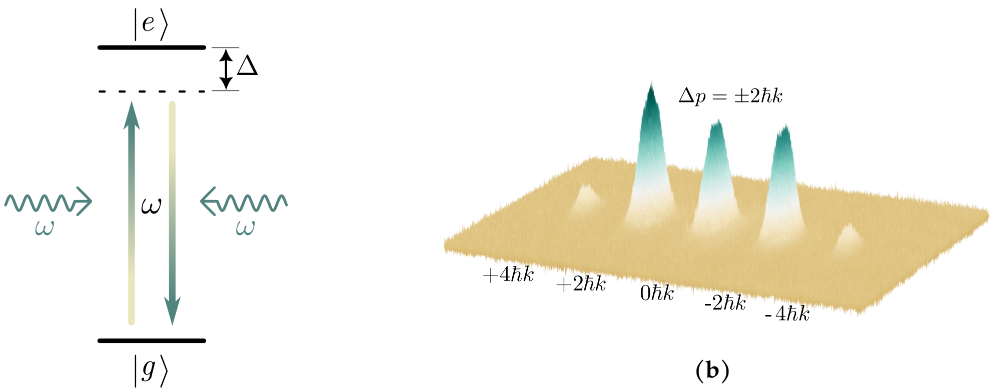

(a) (b)

Figure 1.8: (a) Level scheme of a two-photon lattice where the atom is transferred to the excited state $|e\rangle$ by absorbing a photon with the frequency ω and followed up by a stimulated emission into the ground state $|g\rangle$ for a full cycle. (b) Exemplary time of flight absorption image of a BEC superimposed to a two-photon lattice potential. The resulting picture contains atoms which are separated by a momentum difference of $\Delta p = \pm 2\hbar k$ implying the presence of a $\lambda/2$ periodicity.

where $\cos(\alpha) = \hat{\mathbf{e}}_1 \cdot \hat{\mathbf{e}}_2$ and the phase difference $\varphi = \varphi_1 - \varphi_2$.
In the experiment, parallel polarization between the two beams is used to maximize the interference term I_{int}, where the resulting lattice potential with periodicity $\lambda/2$ writes as

$$V_{2\text{ph}}(z) = \frac{V_2}{2}\cos(2kz + \varphi) + \text{const.} \tag{1.43}$$

Changing φ moves the lattice, while $V_2 \propto \sqrt{I_1 I_2}$ and is commonly measured in recoil energy $E_R = \hbar^2 k^2/2m$ [88], with m as the atomic mass.
The lattice at hand, which possesses a periodicity of $\lambda/2$, can also be described in terms of virtual processes within the quantum-mechanical framework. In this description, the lattice potential is created when an atom absorbs a photon from a laser beam in one direction and subsequently emits it in a stimulated manner into the laser beam from the other direction, as depicted in Figure 1.8(a). This effective two-photon process leads to the atoms localization in a lattice structure, where each site is separated by $\pm 2\hbar k$ in respective direction, in momentum space (as seen in Figure 1.8(b)).

1.3.2 Four-photon Lattice Potential

After discussing the simple case of a two-photon lattice, where the emerging periodicity $\lambda/2$ is directly correlated to the wavelength λ of the laser light [89], larger periodicity $\lambda/2n$ can also be realized by incorporating the same wavelength of the laser, but with higher order processes of $2n$ photons transferring momenta of $2n\hbar k$ to the atoms [52].
Figure 1.9(a) shows the four-photon lattice scheme employed in the experiment with a corresponding time of flight distribution of atoms with a momentum separation of $4\hbar k$ (Figure 1.9(b)). To suppress lower order processes, multiple frequencies with different polarizations are utilized. In conventional two-level schemes, four-photon processes are

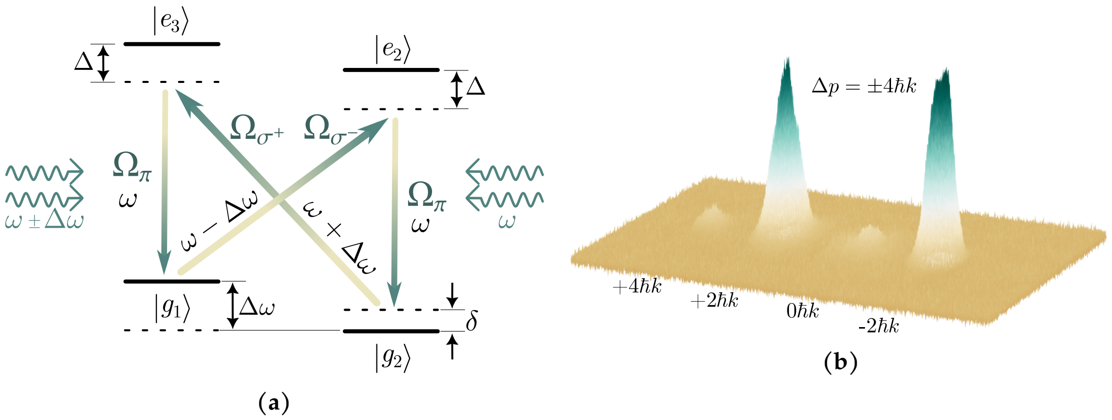

(a) (b)

Figure 1.9: (a) Level scheme of a four-photon lattice containing two ground states $|g_1\rangle$ and $|g_2\rangle$ and two excited states $|e_2\rangle$ and $|e_3\rangle$. Two sets of counter-propagating laser frequencies ω from one side and $\omega \pm \Delta\omega$ from the opposite side are used to generate a closed loop four-photon transition cycle, formed by two absorption- and the stimulated emission processes, respectively. Increasing the two-level detuning δ suppresses undesired two-photon processes. (b) Exemplary time of flight absorption image of a BEC superimposed to a four-photon lattice potential. The resulting picture contains atoms which are separated by a momentum difference of $\Delta p = \pm 4\hbar k$ resulting in a $\lambda/4$ spatial periodicity.

highly unlikely due to the rapid relaxation into the initial ground state following the preceding excitation, occurring faster than a second excitation can take place. To address this issue, a double ground state system comprising of $|g_1\rangle$ and $|g_2\rangle$ is introduced, which is experimentally realized using the m_F manifold of the $|5^2S_{1/2}, F = 1\rangle$ hyperfine state of ^{87}Rb rubidium atoms. With this scheme, it is possible to realize two subsequent absorption and re-emission cycles, where a total momentum of $4\hbar k$ is transferred to the atom, leading to a spatial lattice periodicity of $\lambda/4$. As shown in earlier works on the experiment during the PhD thesis of G. Ritt [90], the four-photon lattice dynamics can be described by the time-dependent perturbation theory

$$i\hbar\partial_t |\Psi(z,t)\rangle = \left[\hat{H}_0 + \hat{\mathfrak{I}}(z,t)\right] |\Psi(z,t)\rangle \tag{1.44}$$

where the non-perturbed Hamiltonian $\hat{H}_0$ writes as

$$\hat{H}_0 = \hbar \begin{pmatrix} 0 & 0 & 0 & 0 \\ 0 & \Delta\omega - \delta & 0 & 0 \\ 0 & 0 & \omega + \Delta & 0 \\ 0 & 0 & 0 & \omega + \Delta \end{pmatrix}, \tag{1.45}$$

with ω as the frequency of the lattice beam, $\Delta\omega$ the added (or subtracted) amount for the used four-photon process, Δ the single-photon detuning of the optical transition to the excited states $|e_1\rangle$ and $|e_2\rangle$ and δ the two-photon detuning to the the second ground state $|g_2\rangle$. It is easy to see, that the eigenbasis of this Hamiltonian is given by the non-perturbed ground- and excited states $\{|g_1\rangle, |g_2\rangle, |e_1\rangle, |e_2\rangle\}$, where the energy scaling $\delta < \Delta\omega \ll \Delta \ll \omega$ allows for the approximation of $H_{4,4} = \omega + \Delta + \Delta\omega - \delta \approx \omega + \Delta$. The interaction operator $\hat{\mathcal{J}}(z,t)$ in equation (1.44), representing the time-dependent perturbation caused by the interaction of the atomic dipole moment $\mathbf{p}_{\text{in}}$ with the electric field of the lattice beams, can be written as

$$\begin{aligned} \mathcal{J}_{i,j} = \langle g_i| \, \mathbf{p}_{\text{in}}\mathbf{E}(z,t) \, |a_j\rangle = & \\ & \mathcal{J}_{1,3} = \hbar\Omega_\pi \cos(\omega t + kz) = \mathcal{J}^*_{3,1} \\ & \mathcal{J}_{1,4} = \hbar\Omega_{\sigma^+} \cos((\omega + \Delta\omega)t - kz) = \mathcal{J}^*_{3,1} \\ & \mathcal{J}_{2,3} = \hbar\Omega_{\sigma^-} \cos((\omega + \Delta\omega)t + kz) = \mathcal{J}^*_{3,2} \\ & \mathcal{J}_{2,4} = \hbar\Omega_\pi \cos(\omega t + kz) = \mathcal{J}^*_{4,2}, \end{aligned} \tag{1.46}$$

where the respective π- and $\sigma^\pm$- transitions are represented by the Rabi-frequencies $\Omega_{\sigma^\pm}$ and Ω_π. Equation (1.44) is solved with the following ansatz

$$|\Psi(z,t)\rangle = \begin{pmatrix} c_1(z,t) \\ e^{-i(\Delta\omega-\delta)t} \cdot c_2(z,t) \\ e^{-i(\omega+\delta)t} \cdot c_3(z,t) \\ e^{-i(\omega+\delta)t} \cdot c_4(z,t), \end{pmatrix} \tag{1.47}$$

where, after applying the *rotating wave approximation* (RWA), the resulting coefficients c_i are presented as four coupled differential equations

$$\dot{c}_1 = -\frac{i}{2}\left(\Omega_\pi e^{-i\Delta t+ikz} \cdot c_3 + \Omega_{\sigma^+} e^{-i\Delta t-ikz} \cdot c_4\right) \tag{1.48}$$

$$\dot{c}_2 = -\frac{i}{2}\left(\Omega_{\sigma^-} e^{-i(\Delta+\delta)t-ikz} \cdot c_3 + \Omega_\pi e^{-i(\Delta+\delta)t+ikz} \cdot c_4\right) \tag{1.49}$$

$$\dot{c}_3 = -\frac{i}{2}\left(\Omega^*_\pi e^{i\Delta t-ikz} \cdot c_1 + \Omega^*_{\sigma^-} e^{i(\Delta+\delta)t+ikz} \cdot c_2\right) \tag{1.50}$$

$$\dot{c}_4 = -\frac{i}{2}\left(\Omega^*_{\sigma^+} e^{i\Delta t+ikz} \cdot c_1 + \Omega^*_\pi e^{i(\Delta+\delta)t+ikz} \cdot c_2\right). \tag{1.51}$$

Assuming slow varying ground state populations c_1 and c_2, allows for integrating over equations (1.50) and (1.51) yielding coefficients c_3 and c_4, which in turn can be substituted in equations (1.48) and (1.49), and with $\Omega_{\text{eff},\pm} = {}^{\Omega_{\sigma^\pm}\Omega^*_\pi}/_{2\Delta}$ resulting in an effective two-level system

$$\dot{c}_1 = \frac{i}{2}\left[\frac{|\Omega_\pi|^2 + |\Omega_{\sigma^+}|^2}{2\Delta} c_1 + e^{i\delta t}\left(\Omega^*_{\text{eff},-} e^{i2kz} + \Omega_{\text{eff},+} e^{-i2kz}\right) c_2\right] \tag{1.52}$$

$$\dot{c}_2 = \frac{i}{2}\left[e^{-i\delta t}\left(\Omega_{\mathrm{eff},-}e^{-i2kz} + \Omega^*_{\mathrm{eff},+}e^{i2kz}\right)c_1 + \frac{|\Omega_\pi|^2 + |\Omega_{\sigma-}|^2}{2\Delta}c_2\right] \tag{1.53}$$

The final formalism for $\dot{c}_1$ can be derived, by assuming that the initial preparation takes place in the $|g_1\rangle$ state, where with a large enough two-photon detuning δ and $c_2 \ll c_1$, the population coefficient can be described by a single equation

$$\dot{c}_1 = i\left[\frac{|\Omega_\pi|^2 + |\Omega_{\sigma+}|^2}{4\Delta} - \frac{|\Omega_{\mathrm{eff},+}|^2 + |\Omega_{\mathrm{eff},-}|^2}{4\delta} - \frac{|\Omega_{\mathrm{eff},+}\Omega_{\mathrm{eff},-}|}{4\delta}\cos(4kz + \varphi_{\lambda/4})\right]c_1. \tag{1.54}$$

For this, equation (1.53) is integrated, as a result adiabatically eliminating the second ground state $|g_2\rangle$. Taking a closer look at equation (1.54) reveals three terms, where the first one represents an energy shift due to two-photon processes, while the second and third one show higher order effects in form of four-photon processes. The periodicity of $\lambda/4$ is depicted in the last term, yielding the effective potential

$$V_{\lambda/4}(z) = \frac{V_4}{2}\cos(4kz + \varphi_{\lambda/4}) + \mathrm{const}, \tag{1.55}$$

where the phase $\varphi_{\lambda/4}$ is defined with $\Omega_{\mathrm{eff},+}\Omega_{\mathrm{eff},-} = |\Omega_{\mathrm{eff},+}\Omega_{\mathrm{eff},-}|e^{i\varphi_{\lambda/4}}$ and the potential depth scales as $V_4 \propto I_\pi I_\sigma/\delta$. Increasing the two-photon detuning, suppresses two-photon processes, while also decreasing the potential depth of the four-photon lattice (as will be demonstrated in chapter 3.4). Variation of the phase $\varphi_{\lambda/4}$ can be used to spatially move the lattice.

The presented scheme to generate a multi-photon lattice potential enables the creation of a four-photon lattice with a spatial periodicity of $\lambda/4$. This scheme realizes an experimental tool that can be used to create both standing wave two- and four-photon potentials using an optical setup realized with a single laser source [52].

1.3.3 Bloch Formalism and Dispersion Relations

In the following, the dynamics of a system composed of a Bose-Einstein condensate superimposed to an optical lattice potential will be discussed, where the atomic dispersion relation will be derived out of the Gross-Pitaevskii equation (GPE) (1.14). Experimentally a short expansion phase for the atoms can be used to ensure that the atomic interaction can be neglected. The equation of motion can then be written as

$$i\hbar\frac{\partial}{\partial t}\Psi(z,t) = \left(\frac{\hat{p}^2}{2m} + V(z)\right)\Psi(z,t), \tag{1.56}$$

where $\hat{p} = -i\hbar\partial_z$ represents the momentum operator, m the atomic mass and $V(z)$ the external potential introduced with equation (1.43). Due to the periodic nature of the system, it is convenient to solve equation (1.56) with the Bloch ansatz $\Psi(z) = e^{-iqz/\hbar}u_q(z)$ [85], consisting of a plane wave in propagation direction z and a periodic function $u_q(z)$ with the same periodicity as the external lattice potential $V(z)$, hence introducing the motion of a free particle with the quasimomentum q. Experimentally, the external potential $V(z)$ is the summation of both the two-photon- and four-photon potentials $V_{\lambda/2}$ and $V_{\lambda/4}$ (equations (1.43) and (1.55))

$$V(z) = \frac{V_2}{4}\left(e^{i2kz} + e^{-i2kz}\right) + \frac{V_4}{4}\left(e^{i(4kz+\varphi)} + e^{-i(4kz+\varphi)}\right), \tag{1.57}$$

where the periodicity $V(z) = V(z+L)$ with $L = \lambda/2$ is also represented in the Bloch ansatz $u_q(z,t) = u_q(z+L,t)$. With this, equation (1.56) writes as

$$i\hbar\frac{\partial}{\partial t}u_q(z,t) = \left(\frac{(\hat{p}+q)^2}{2m} + V(z)\right)u_q(z,t), \tag{1.58}$$

where $u_q(z,t) = \sum_l c_{q,l}(t)e^{i2lkz}$ is a discrete Fourier sum with $l \in \mathbb{Z}$. Substituting the external potential $V(z)$ from equation (1.57) results in a coupled differential equation for the coefficients $c_{q,l}(t)$

$$i\hbar\dot{c}_{q,l} = \frac{(2l\hbar k + q)^2}{2m}c_{q,l} + \frac{V_2}{4}\left(c_{q,l-1} + c_{q,l+1}\right) + \frac{V_4}{4}\left(e^{i\varphi}c_{q,l-2} + e^{-i\varphi}c_{q,l+2}\right), \tag{1.59}$$

which can be rewritten into a Schrödinger equation $i\hbar\partial_t\left|\Psi\right\rangle = H\left|\Psi\right\rangle$ with $\left|\Psi\right\rangle = \sum_l c_{q,l}\left|2l\hbar k + q\right\rangle = (\ldots,c_{q,l-1},c_{q,l,},c_{q,l+1}\ldots)^T$. The Hamilton operator can be described with

$$H = \begin{pmatrix}
E_{-l} & V_2/4 & V_4/4 & 0 & 0 & 0 & 0 & 0 & 0 \\
V_2/4 & \ddots & V_2/4 & V_4/4 & 0 & 0 & 0 & 0 & 0 \\
V_4/4 & V_2/4 & E_{-2} & V_2/4 & V_4/4 & 0 & 0 & 0 & 0 \\
0 & V_4/4 & V_2/4 & E_{-1} & V_2/4 & V_4/4 & 0 & 0 & 0 \\
0 & 0 & V_4/4 & V_2/4 & E_0 & V_2/4 & V_4/4 & 0 & 0 \\
0 & 0 & 0 & V_4/4 & V_2/4 & E_1 & V_2/4 & V_4/4 & 0 \\
0 & 0 & 0 & 0 & V_4/4 & V_2/4 & E_2 & V_2/4 & V_4/4 \\
0 & 0 & 0 & 0 & 0 & 0 & V_2/4 & \ddots & V_2/4 \\
0 & 0 & 0 & 0 & 0 & 0 & 0 & V_4/4 & E_{+l},
\end{pmatrix} \tag{1.60}$$

where the diagonal elements are represented by the kinetic energy $E_{\text{kin}}(l)$ for each $l \in \mathbb{Z}$

$$H_{ll} = E_{\text{kin}}(l) = \frac{(2l\hbar k + q)^2}{2m} \tag{1.61}$$

and the off-diagonal elements $H_{l,l+1} = H^*_{l+1,l} = V_2/4$ and $H_{l,l+2} = H^*_{l+2,l} = V_4/4e^{i\varphi}$ depict induced coupling by the respective two- and four-photon lattice potentials.

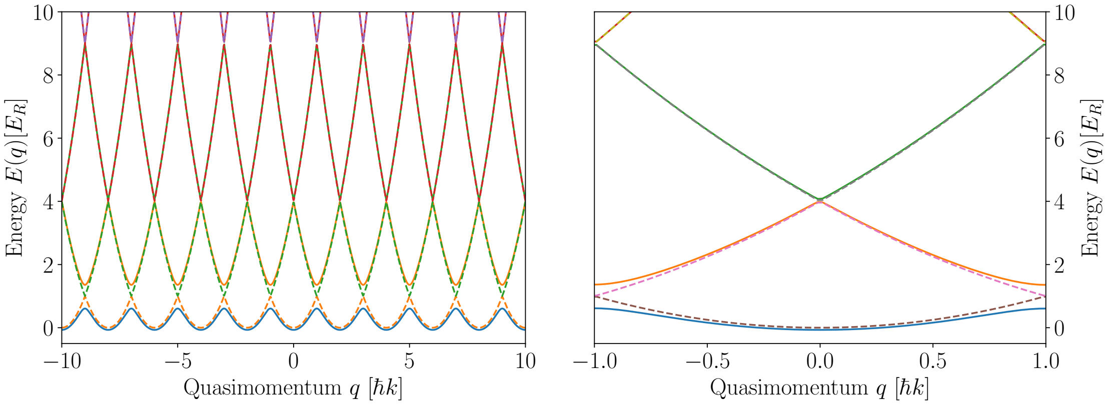

(a) **(b)**

Figure 1.10: (a) Resulting dispersion relation of a two-photon lattice for a large range of the quasimomentum q. The energy on the y-axis is given in units of the recoil energy E_R. (b) The first Brillouin zone of the two-photon lattice is expressed in the interval of $q \in (-\hbar k, +\hbar k]$. The dashed lines represent the free particle parabolas (bare states) for the case of vanishing optical light fields. Increasing the lattice laser beam intensity results in avoided crossing at the quasimomentum $q = \pm\hbar k$.

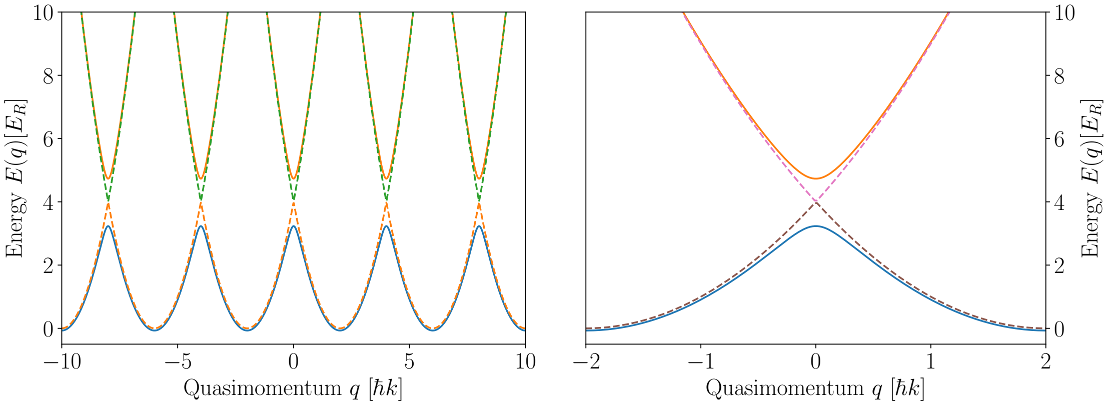

(a) **(b)**

Figure 1.11: (a) Resulting dispersion relation of a four-photon lattice for a large range of the quasimomentum q. The energy on the y-axis is again given in units of the recoil energy E_R. (b) The first Brillouin zone of the four-photon lattice is now expressed in the interval of $q \in (-2\hbar k, 2\hbar k]$ due to higher order terms. The dashed lines represent the free particle parabolas (bare states) for the case of vanishing optical light fields. Increasing the lattice laser beam intensity results in avoided crossing at the quasimomentum $q = 0\hbar k$.

The solution for a two-photon lattice can be expressed as a dispersion relation shown in Figure 1.10 where the energy scale is given in recoil energy $E_R = {(\hbar k)^2}/{2m}$. The usual presentation of these energy spectra is shown in the so-called *Brillouin zone* (as seen in Figure 1.10(b) and 1.11(b)), which, motivated by solid-state physics, is a reduced band structure visualization ($q \in (-\hbar k, +\hbar k]$) representing the range of possible momenta for electrons in a crystal.

In the absence of the optical potential, the atomic dynamics can be well described by parabolas representing unperturbed particles with respective momentum $p = \pm 2\hbar k$ (*bare states*), shown in dashed lines in Figure 1.10. In the presence of an optical light field (blue line), the degeneracy at the intersection points is lifted, where the *avoided crossing* results in a band gap at the quasimomentum $q = \pm\hbar k$. For the case of a four-photon lattice, as expected, the avoided crossing takes place at the intersection points of higher order bands, resulting in a band gap at the quasimomentum $q = 0\hbar k$ (as seen in Figure 1.11).

In the experiment, the energy gap of the effective two-level system is simulated using the dispersion relation shown in Figure 1.11. At quasimomentum $q = 0\hbar k$, the oscillation frequency of the qubit, denoted as ω_{q}, is directly proportional to the four-photon lattice potential V_4. This relationship implies that by increasing the optical laser power, the band gap can be enlarged. To prepare the atoms at this band gap, a two-photon lattice Bragg pulse is employed, transferring a real momentum of $p = \pm 2\hbar k$ onto the atoms. Superimposing the harmonic potential of the optical dipole trap onto this effective qubit enables the quantum simulation of the periodic quantum Rabi model at deep strong coupling, a topic that will be further elaborated upon in the upcoming chapter.

CHAPTER 2

Quantum Simulation of the Periodic Quantum Rabi Model

In the following, a brief theoretical introduction to quantum Rabi physics is given, where different regimes emerge for varying the coupling strength between the two-level system and the bosonic mode. Three distinct domains of *strong-*, *ultra-strong-* and *deep strong coupling regimes* emerge, in which the latter encompasses the main topic of this dissertation. As will be seen later, the experimental system Hamiltonian describing the motion of ultracold atoms, superimposed onto the combined potentials of the optical dipole trap and the four-photon lattice, resembles a generalization of the usual quantum Rabi model – the periodic quantum Rabi model (pQRM). For sub-cycle temporal evolution, both models show the same dynamics, where previous work has been conducted to simulate the usual quantum Rabi model in the deep strong coupling regime [53].
In this work, the focus is to investigate the periodic quantum Rabi model which emerges when observing longer interaction times when the first Brillouin zone (as can be seen in Figure 1.11(b)) is crossed. Here, the periodic nature becomes apparent, where collapse and revival of bosonic excitation number and initially prepared vacuum states are predicted. In final remarks of this chapter, a digression into superconducting qubits is presented, due to an existing analogy between the single particle Hamiltonian with superconducting Fluxonium systems [91].

2.1 The Quantum Rabi Model (QRM)

As previously mentioned, the most fundamental interaction between a bosonic mode and a two-level system can be well described by the quantum Rabi model. Inspired by [92], the Hamiltonian

$$\hat{H}_{\mathrm{QRM}} = \hat{H}_{\mathrm{Field}} + \hat{H}_{\mathrm{Qubit}} + \hat{H}_{\mathrm{Interaction}}, \tag{2.1}$$

consisting of the sub-system of the bosonic field $\hat{H}_{\mathrm{Field}}$, the qubit $\hat{H}_{\mathrm{Qubit}}$ and the interaction term $\hat{H}_{\mathrm{Interaction}}$, will be derived in the following.
Relatively straight forward, the contribution of the bosonic field can be described by

$$\hat{H}_{\mathrm{Field}} = \hbar\omega\hat{a}^{\dagger}\hat{a}, \tag{2.2}$$

where $\hat{a}^{\dagger}$ and $\hat{a}$ depict the creation- and annihilation operators of the bosonic field with the frequency ω.

An intuitive approach is used to describe the two-level sub-system $\hat{H}_{\text{Qubit}}$

$$\hat{H}_{\text{Qubit}} = \frac{1}{2}\hbar\omega_{\text{q}}\hat{\sigma}_z, \tag{2.3}$$

where the factor $1/2$ arises from the energy gap $\Delta E_{\text{q}} = \hbar\omega_{\text{q}}$ between ground- and excited state driven by the inversion operator $\hat{\sigma}_z = |\uparrow\rangle\langle\uparrow| - |\downarrow\rangle\langle\downarrow|$.
The interaction term can be expressed as the dipole operator $\hat{d} = d(\hat{\sigma}_+ + \hat{\sigma}_-)$, where the Pauli matrices $\sigma_+ = |\uparrow\rangle\langle\downarrow|$ and $\sigma_- = |\downarrow\rangle\langle\uparrow|$ correspond to respective ladder operators of the two-level system, acting on the electric field $\hat{\mathbf{E}}$ of the bosonic mode

$$\begin{aligned}\hat{H}_{\text{Interaction}} &= -\hat{\mathbf{d}}\cdot\hat{\mathbf{E}} \\ &= \underbrace{\hat{\mathbf{d}}\cdot\hat{\mathbf{e}}}_{=\hat{d}}\underbrace{\left(-\frac{\hbar\omega}{\varepsilon_0 V}\right)^{1/2}\sin(kz)}_{=\xi}(\hat{a}+\hat{a}^\dagger) = \hat{d}\xi(\hat{a}+\hat{a}^\dagger) \\ &= \hbar g(\hat{\sigma}_+ + \hat{\sigma}_-)(\hat{a}+\hat{a}^\dagger).\end{aligned} \tag{2.4}$$

Here, ê represents the polarization direction, ω the mode frequency, V the effective Volume of the resonator and k the wave vector. The factor $g = d\xi/\hbar$ is introduced as the coupling strength and will prove to be a decisive parameter to distinguish between different regimes of the quantum Rabi model.
Introducing $\hat{\sigma}_x = (\hat{\sigma}_+ + \hat{\sigma}_-)$ the full quantum Rabi Hamiltonian can be written as

$$\begin{aligned}\hat{H}_{\text{QRM}} &= \hat{H}_{\text{Field}} + \hat{H}_{\text{Qubit}} + \hat{H}_{\text{Interaction}} \\ &= \hbar\omega\hat{a}^\dagger\hat{a} + \frac{1}{2}\hbar\omega_{\text{q}}\hat{\sigma}_z + \hbar g\hat{\sigma}_x(\hat{a}+\hat{a}^\dagger).\end{aligned} \tag{2.5}$$

The temporal evolution of the operators $\hat{\sigma}_\pm(t)$, $\hat{a}(t)$ and $\hat{a}^\dagger(t)$, give rise to four different combinations of energy exchange between bosonic field and two-level system:

$$\begin{aligned}&\hat{\sigma}_+\hat{a} \propto e^{i(\omega_{\text{q}}-\omega)t} \\ &\hat{\sigma}_-\hat{a}^\dagger \propto e^{-i(\omega_{\text{q}}-\omega)t} \\ &\hat{\sigma}_+\hat{a}^\dagger \propto e^{i(\omega_{\text{q}}+\omega)t} \\ &\hat{\sigma}_-\hat{a} \propto e^{-i(\omega_{\text{q}}+\omega)t}.\end{aligned} \tag{2.6}$$

At this point, a subdivision can be made into fast and slowly varying terms. For relatively weak coupling strength between the two-level system and the bosonic field the counter-rotating terms $\hat{\sigma}_-\hat{a}$ and $\hat{\sigma}_+\hat{a}^\dagger$ can be neglected and only the slowly varying fractions of equation (2.6) give rise to the well-known Jaynes-Cummings model (JCM) formulated in 1963 as a special case of the full quantum Rabi model [4]

$$\hat{H}_{\text{JCM}} = \hbar\omega\hat{a}^\dagger\hat{a} + \frac{\hbar\omega_{\text{q}}}{2}\hat{\sigma}_z + \hbar g\left(\hat{\sigma}_+\hat{a} + \hat{\sigma}_-\hat{a}^\dagger\right). \tag{2.7}$$

To understand it in a slightly more physical sense, by considering the absorption of a photon from the bosonic field, the atom is transferred to the excited state and vice versa ($\hat{\sigma}_+\hat{a}$ and $\hat{\sigma}_-\hat{a}^\dagger$), hence only energy-conserving (*co-rotating*) terms are used to describe dynamics in the Jaynes-Cummings system.
While a plethora of experiments demonstrating the strong coupling regime of the JCM have been thoroughly investigated in cavity quantum electrodynamics [93–95], atomic physics [96], quantum dots [97], circuit quantum electrodynamics [98, 99] and trapped ions [100–103], this thesis presents the case for a large coupling strength $g \gg \omega$, which dominates over all other energy scales in the system. In this extreme parameter regime, characterized by the inclusion of both the co-rotating and counter-rotating terms in the complete quantum Rabi Hamiltonian, finding a solution for the system was challenging for a long time [104]. An exact solution was first found by D. Braak in 2011 using the parity symmetry ($\mathbb{Z}_2$-symmetry) of the system leading to so called *G-functions* whose zeros yield the exact eigenvalues of the Rabi Hamiltonian [15]. The dynamics of an initial state which is prepared in eigenstates of the two-level system (meaning $|\uparrow\rangle$ or $|\downarrow\rangle$) can be described by so called *parity chains* due to the $\mathbb{Z}_2$-symmetry of the quantum Rabi model. By showing that $[\hat{H},\hat{\Pi}] = 0$, where $\hat{H}$ is the quantum Rabi Hamiltonian and $\hat{\Pi}$ is the parity operator, the Hilbert space can be described by the dynamics of two subsystem Hamiltonians H_+ and H_-, corresponding to respective parity chains Π_+ and Π_- visualized in Figure 2.1. The Π_- chain in Figure 2.1(a) represents the dynamics coupled by the co-rotating terms, while the Π_+ chain shows the dynamics driven by the counter-rotating terms, which is usually neglected for the strong coupling regime of the JCM.

Spectral Classification of the QRM

As mentioned before, different dynamics emerge, when the coupling strength between bosonic mode and qubit is varied. If decoherence effects due to loss processes occur faster than energetic exchange between the subsystems, the weak coupling regime is present. When the coupling strength is larger than decoherence effects, the *strong-coupling regime* (SC regime: $g/\omega \ll 1$) emerges, and the general quantum Rabi Hamiltonian (2.5) can be simplified to the Jaynes-Cummings Model (2.7), describing coherent exchange of bosonic excitations between the subsystems [106]. This approximation becomes invalid for larger coupling strengths ($g/\omega \gtrsim 0.1$), as the counter-rotating terms become increasingly dominant in the regime known as the *ultra-strong coupling* (USC) regime. The transition from the SC regime to the USC regime occurs continuously [106], allowing for perturbation theory to be applied at the early stage of the transition. Thus, the beginning of the USC regime, which can be described by the Bloch-Siegert Hamiltonian, is referred to as the *perturbative* USC regime [21, 22]. The so called Juddian points depicted in Figure 2.2 (directly taken from [22]) separate the perturbative USC regime from the usual USC regime, revealing not only the effect of the ratio g/ω but also the energy (y-axis) that the system can access. The final domain of the quantum Rabi model concludes the *deep-strong coupling regime* (DSC), where the coupling strength is larger than all other significant energy scales ($g/\omega \gtrsim 1$). Here, the nature of the strongly entangled ground-state dynamics of the subsystems is reflected by the emergence of counter-intuitive physical behavior, such as the creation and annihilation of bosonic excitations out of the vacuum and the collapse and revival of

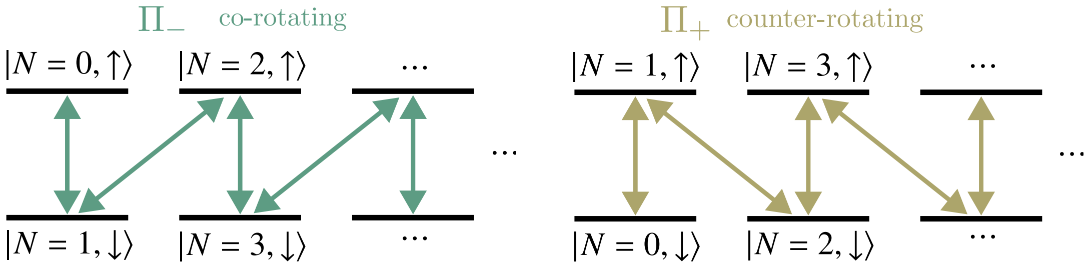

(a) (b)

Figure 2.1: Parity chains of the quantum Rabi model subdivided into two classes of Π_- (a) and Π_+ (b). The underlying dynamics which are shaped by the $\mathbb{Z}_2$ symmetry of the QRM Hamiltonian can be fully described by the combination of the parity operator $\hat{\Pi}$, where the co- and counter-rotating terms couple the sub-dynamics of respective Π_- and Π_+ chain.

initially prepared states devoid of excitations. In contrast to the perturbative USC regime, where the coupling strength is introduced as perturbation, the perturbative DSC regime (pDSC) is a consequence of the two-level system's energy splitting acting as a perturbation onto the coupling strength. This means that the non-perturbative DSC regime directly follows after the non-perturbative USC regime.

The experiment operates at a relative coupling strength $g/\omega \in [4; 6.5]$, which is far in the pDSC regime. The ability to vary the two-level splitting by changing the intensity of the optical lattice laser beam allows for the exploration of the so-called *dispersive* DSC regime ($\omega_\mathrm{q} \gtrsim g$, while $g \gg \omega$), where the dynamics are governed by the dominant energy of the two-level system.

In the following, numerical simulations of the temporal evolution of the bosonic excitation number $\hat{N}$ for two cases of relative coupling strengths are presented: $g/\omega = 0.1$ (in the SC regime) and $g/\omega = 6.4$ (in the pDSC regime). To maintain simplicity, the qubit frequency is set at a similar scale to the bosonic mode frequency ($\omega_\mathrm{q} \simeq \omega$), while the x-axis is shown in units of $\omega t/2\pi$. When initializing the system in the vacuum mode of the bosonic field and the ground state of the two-level system ($|N = 0, \downarrow\rangle$), only vacuum Rabi oscillations occur in the strong coupling regime, depicted as a green line in the inset plot of Figure 2.3(a). In contrast, in the pDSC regime, which is the focus of this thesis, a rise up to $\hat{N}_\mathrm{DSC,max} \approx 160$ is observed, shown as a solid yellow line in the simulations. The same parameters are again utilized for the excited state preparation ($|N = 0, \uparrow\rangle$) and are illustrated in Figure 2.3(b). To emphasize the difference between the two regimes, which are separated by a quantum phase transition (QPT) [107], an inset plot is utilized again to provide a close-up view of the strong-coupling temporal dynamics (green solid line). Here the maximum bosonic excitation is now $\hat{N}_\mathrm{JCM,max} = 1$, while the behavior for the pDSC regime is unaffected for the chosen qubit frequency $\omega_\mathrm{q} \simeq \omega$. Subsequent sections will demonstrate that further increasing the qubit frequency results in a transition into the dispersive DSC regime, notably observed when examining the temporal dynamics of the bosonic excitation number as the qubit frequency approaches the coupling strength $\omega_\mathrm{q} \to g$.

The origin of the displayed temporal evolution of the oscillating excitation number in the perturbative deep strong coupling regime lies in the occupation probabilities of the number

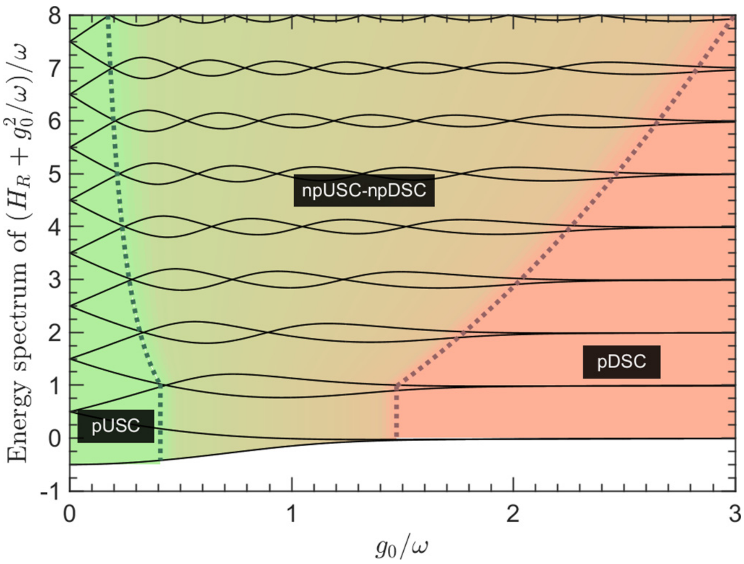

Figure 2.2: Coupling regimes of the quantum Rabi model depending on the relative coupling strength g/ω and the mean energy that the system can access (directly taken from [105]). The first Juddian points (first dotted line) mark the area of the perturbative ultra strong coupling regime (pUSC) followed up by an intermediate region where the non-perturbative ultra- and deep strong coupling regime coexist (npUSC-npDSC). The final regime, which is simulated in this thesis, concludes the perturbative deep strong coupling regime (pDSC) for larger coupling strengths introduced with the second Juddian points (second dotted line).

states (Fock states) of the field mode. This oscillatory nature leads to a rapid collapse of the initially prepared ground state $|N = 0, \downarrow\rangle$, while after a full period, the initial state revives. Figure 2.4(a) shows a visualization of the temporal evolution of the excitation number wavepackets for a full oscillation period and a vanishing qubit frequency $\omega_\text{q} \to 0$. On the right side (Figure 2.4(b)), a numerical simulation of the resulting collapse and revival of an initially prepared state $|N = 0, \downarrow\rangle$ is shown for the qubit frequency $\omega_\text{q} \to 0$ (yellow) and ${}^{\omega_\text{q}}/_{\omega} \approx 2$ (green dashed). Visible partial revivals and collapses in the simulation are attributed to the self-interference of photon number wavepackets, resulting in a distorted pattern and will be verified with experimental data in the later chapter [108].

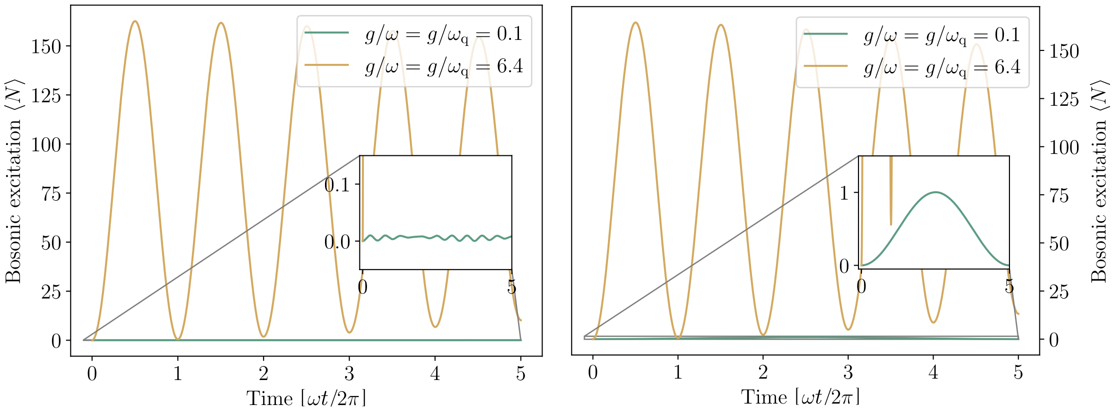

(a)

(b)

Figure 2.3: (a) Temporal evolution of the bosonic excitation $\langle N \rangle$ for an initial vacuum state preparation in the ground state of the qubit $|N = 0, \downarrow\rangle$. In the strong coupling regime ($g/\omega = 0.1$, green) the dynamics are governed by vacuum Rabi oscillations (inset plot). For larger coupling strengths in the DSC regime ($g/\omega = 6.4$, yellow) a large number of $\hat{N}_{\mathrm{DSC,max}} \approx 160$ is reached (yellow). (b) Preparation in the excited state of the qubit does not change the dynamics for the DSC regime, but now shows a rise up to $\hat{N}_{\mathrm{JCM,max}} = 1$ (inset plot, green solid line).

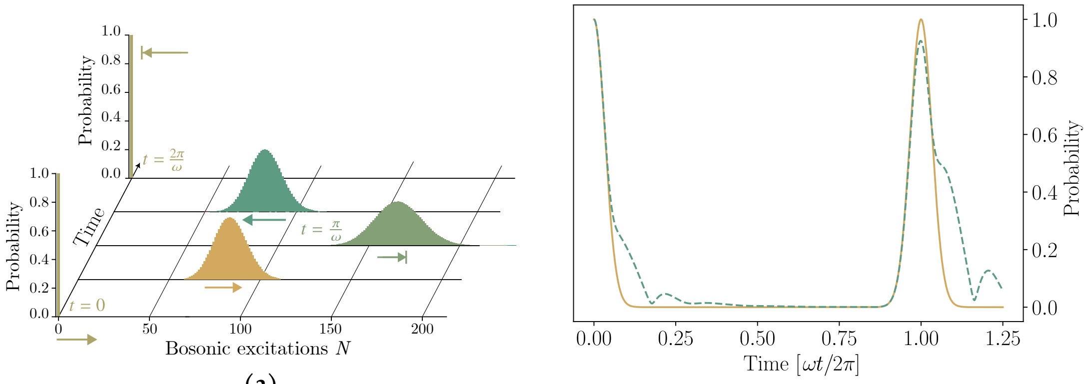

(a)

(b)

Figure 2.4: (a) Temporal evolution of the Fock states occupation probability for a full oscillation period ($t = 0 \rightarrow t = 2\pi/\omega$) and initial preparation in $|N = 0, \downarrow\rangle$, a relative coupling strength $g/\omega = 6.4$ and a vanishing qubit frequency $\omega_q \rightarrow 0$. The visualization shows typical emergence of photon number wavepackets oscillating in time. (b) Numerical simulation of resulting collapse and revival patterns for a vanishing qubit frequency $\omega_q \rightarrow 0$ (yellow solid line) and a larger splitting $\omega_q/\omega \approx 2$ (green dashed line), where partial revivals are observed, which are understood as interference of photon number wavepackets.

2.2 Similarities and Differences between pQRM and QRM

The following section describes the analogy between the quantum Rabi model and the system simulated in the experiment, which is called the periodic quantum Rabi model (pQRM). A separation is made for the case of small interaction time, limiting the dynamics to the first Brillouin zone, where both the experimentally simulated system and the QRM exhibit the same dynamics. Since these sub-cycle time scales have already been observed in the context of J. Koch's PhD thesis [53, 27], only a brief presentation of the analogy between the models will be provided here. The main focus of this thesis is the long-time interaction of the periodic version of the quantum Rabi model, which is presented in the regime where the first Brillouin zone is crossed and deviations from the usual quantum Rabi model arise. Interestingly, a similar system represented by fluxonium qubits can be well described by the experimental system Hamiltonian, showing potential applicability for superconducting qubit platforms.

2.2.1 Short Time Interaction

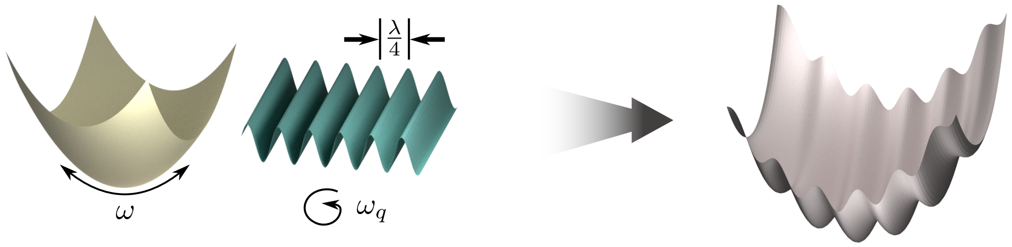

Harmonic potential Four-photon lattice Combined potential

Figure 2.5: Visualization of the harmonic potential (left) with the bosonic mode frequency ω and the four-photon lattice (middle) with the qubit splitting ω_q, which are combined to the total potential illustrated on the right.

The simulation of the quantum Rabi model requires a bosonic field, which is realized by the oscillation of ultra-cold rubidium atoms in an optical dipole trapping potential created by a far-off resonance CO_2 laser beam (see Figure 2.5 for visualization). Superimposing these atoms to a four-photon potential leads to the band structure depicted in Figure 1.11(b), which acts as an effective two-level system with the qubit energy gap $\Delta E_\mathrm{qubit} = \hbar\omega_\mathrm{q}$ with the oscillation frequency ω_q.

The system Hamiltonian including the kinetic energy of the atoms and the harmonic trap, and a periodic potential then writes as

$$\hat{H}_\mathrm{exp} = \underbrace{\frac{m\omega^2}{2}\hat{x}^2}_{\hat{H}_\mathrm{harmonic}} + \underbrace{\frac{\hat{p}^2}{2m} + \frac{V}{2}\cos(4k\hat{x})}_{\hat{H}_\mathrm{periodic}}, \tag{2.8}$$

where, $\hat{p} = -i\hbar\partial/\partial x$ denotes the atoms momentum and $k = 2\pi/\lambda$ is the wave vector, with λ being the wavelength of the lattice laser beam. Furthermore, V represents the optical lattice potential depth, m the atoms mass and ω the bosonic mode frequency, meaning the radial oscillation frequency in the optical dipole trap.

Due to the periodic nature of the optical lattice potential, it is convenient to use the Bloch basis function $\langle \hat{x}|\phi_n(q)\rangle = e^{iqx/\hbar}e^{-i2kx}e^{i4nkx}$ where $n \in \mathbb{Z}$ and $q \in (-2\hbar k, 2\hbar k]$ resembles the first Brillouin zone. The momentum operator is diagonal in the Bloch basis, while the periodic potential introduces a coupling between adjacent bands

$$\begin{aligned} \hat{H}_{\text{periodic}} &= \frac{\hat{p}^2}{2m} + \frac{V}{2}\cos(4k\hat{x})\,|q,n\rangle \\ &= \frac{1}{2m}[q + (2n-1)2\hbar k]^2\,|q,n\rangle + \frac{V}{4}(|q,n+1\rangle + |q,n-1\rangle). \end{aligned} \tag{2.9}$$

By restricting the dynamics to the two lowest bands $n = [0,1]$, the periodic part $\hat{H}_{\text{periodic}}$ of the full Hamiltonian can be written as

$$\hat{H}_{\text{periodic}} = \frac{q^2}{2m} + \frac{2\hbar k}{m}\sigma_z q + \frac{V}{4}\sigma_x, \tag{2.10}$$

where $\sigma_x = |n=0\rangle\langle n=0| - |n=1\rangle\langle n=1|$ and $\sigma_z = |n=1\rangle\langle n=0| + |n=0\rangle\langle n=1|$ was used. Focusing on the harmonic part $\hat{H}_{\text{harmonic}}$ of equation (2.8), we can write

$$\langle \tilde{q},\tilde{n}|\hat{x}^2|q,n\rangle = \int_{-\infty}^{+\infty} dx x^2 e^{i[4(n-\tilde{n})k + (q-\tilde{q})/\hbar]x}. \tag{2.11}$$

Considering diagonal elements in the qubit Hilbert space ($\tilde{n} = n$), results in

$$\langle \tilde{q},n|\hat{x}^2|q,n\rangle = \int_{-\infty}^{+\infty} dx x^2 e^{i(q-\tilde{q})x/\hbar} = -\hbar^2 \langle \tilde{q},n|\,\frac{\partial^2}{\partial q^2}\,|q,n\rangle\,. \tag{2.12}$$

It is easy to see that the harmonic term introduces an operator that is diagonal in the Hilbert space and can be expressed as $\hat{x} = -i\hbar\frac{\partial}{\partial q}$ using the Bloch basis. This results in the quasimomentum operator $\hat{q}$ and the position operator $\hat{x}$ satisfying the commutation relation $[\hat{x},\hat{q}] = i\hbar$.

Analyzing the exponent in equation (2.12) shows that the integral for $n \neq \tilde{n}$ is only non-zero if $4\hbar(n-\tilde{n})k = q - \tilde{q}$. By choosing a quasimomentum difference of $\delta q = q - \tilde{q} = 4\hbar k$, a coupling is induced between neighboring bands ($|2\hbar k,n\rangle\langle -2\hbar k,n+1| + \text{H.c.}$), emphasizing the importance of a four-photon lattice in the experiment.

The position operator $\hat{x}^2$ can be expressed as

$$\hat{x}^2 = -\hbar^2\frac{\partial^2}{\partial q^2}\begin{pmatrix} 1 & 0 \\ 0 & 1 \end{pmatrix} + \zeta(|2\hbar k,n\rangle\langle -2\hbar k,n+1| + |-2\hbar k,n+1\rangle\langle 2\hbar k,n|), \tag{2.13}$$

with $\zeta = \langle -2\hbar k, 1|\,\hat{x}^2\,|2\hbar k,0\rangle$ describing an *Umklapp*-process which is enabled upon reaching the edge of the first Brillouin zone. Combining equation (2.10) and (2.13) and introducing the creation and annihilation operators as

$$\hat{a}^\dagger = \sqrt{\frac{m\omega}{2\hbar}}\left(\hat{x} - \frac{i}{m\omega}q\right) \tag{2.14}$$

and

$$\hat{a} = \sqrt{\frac{m\omega}{2\hbar}}\left(\hat{x} + \frac{i}{m\omega}q\right) \tag{2.15}$$

results in

$$\hat{H} = \hbar\omega\hat{a}^\dagger\hat{a}\mathbb{1}_2 + \frac{V}{4}\hbar\begin{pmatrix}0 & 1\\ 1 & 0\end{pmatrix} + i2\hbar k\sqrt{\frac{\hbar\omega}{2m}}\left(\hat{a}^\dagger - \hat{a}\right)\begin{pmatrix}1 & 0\\ 0 & -1\end{pmatrix}. \tag{2.16}$$

By substituting $\omega_\mathrm{q} = \frac{V}{2}$ as the qubit frequency and using

$$g = 2k\sqrt{\frac{\hbar\omega}{2m}} \tag{2.17}$$

as the coupling strength, a unitary transformation represented by the matrix:

$$U = \frac{1}{\sqrt{2}}\begin{pmatrix}1 & -1\\ 1 & 1\end{pmatrix} \tag{2.18}$$

results in the Hamiltonian

$$\hat{H}_\mathrm{QRM} = \hbar\omega\hat{a}^\dagger\hat{a} + \frac{\hbar\omega_\mathrm{q}}{2}\hat{\sigma}_z + i\hbar g\hat{\sigma}_x\left(\hat{a}^\dagger - \hat{a}\right), \tag{2.19}$$

which is similar to equation (2.5), except for a global phase shift caused by the unitary transformation, which does not affect the observable dynamics in the system [109]. Considering an initial preparation Ψ_0 at the band gap, corresponding to $\hat{q} = 0$ (see Figure 1.11(b)), the analogy of equations (2.8) and (2.19) is ensured when the Umklapp term ζ vanishes. The maximum time of interaction, which in essence is restricted by the dynamics to the first Brillouin zone $\hat{q} \in (-2\hbar k, +2\hbar k]$ can be calculated with $\langle\Psi_0|\,\hat{q}\,|\Psi_0\rangle = 0$ to

$$t_\mathrm{max} = \frac{\pi}{2\omega}. \tag{2.20}$$

After showing the analogy between the quantum Rabi model (QRM) and the periodic quantum Rabi model (pQRM) in the boundaries of the first Brillouin zone, an approximation for the maximum achievable bosonic excitation number N_max can be derived for the case of a vanishing qubit frequency. When applying the *slow qubit approximation* ($\omega_\mathrm{q} \to 0$), this leads to the modification of the quantum Rabi Hamiltonian

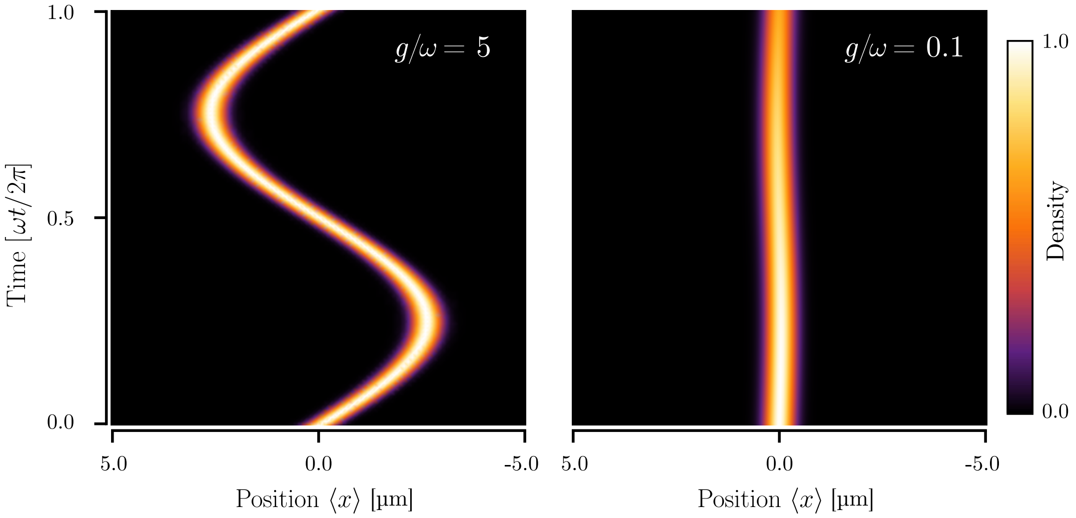

Figure 2.6: Displacement dynamics of an initial state prepared in $|N=0,\downarrow\rangle$ for a large relative coupling strength $g/\omega = 5$ far in the perturbative deep strong coupling regime (left panel) and a ratio $g/\omega = 0.1$ describing the perturbative ultra strong coupling regime (right panel). The wavepackets displacement over the wavepackets size gives direct proof of the pDSC regime.

$$\begin{aligned}\hat{H}_{\omega_\mathrm{q}=0} &= \hbar\omega\hat{a}^\dagger\hat{a} + \hbar g\hat{\sigma}_x(\hat{a}+\hat{a}^\dagger) \\ &= \hbar\omega\left(\hat{a}^\dagger + \frac{g\hat{\sigma}_x}{\omega}\right)\left(\hat{a} + \frac{g\hat{\sigma}_x}{\omega}\right) + \hbar\left(\frac{\omega}{2} - \frac{g^2}{\omega}\right),\end{aligned} \tag{2.21}$$

which can be easily diagonalized by a displacement operator $\hat{D}(\alpha) = e^{\alpha a^\dagger - \alpha^* a}$. The time evolution of a vacuum state $|N=0\rangle = |0\rangle$ with the displaced Hamiltonian $\hat{H}(\alpha)$ results in

$$\begin{aligned}e^{i\hat{H}(\alpha)t/\hbar}|0\rangle &= \hat{D}(-\alpha)e^{i\hat{H}(0)t/\hbar}\hat{D}(\alpha)|0\rangle \\ &= e^{\frac{i\omega t}{2}} e^{\frac{ig^2 t}{\omega}} \hat{D}\,|e^{-i\omega t}\alpha\rangle \\ &= e^{\frac{i\omega t}{2}} e^{\frac{ig^2 t}{\omega}} e^{\mathrm{Im}(|\alpha|^2)e^{i\omega t}} \hat{D}\left(\alpha\left(e^{-i\omega t - 1}\right)\right)|0\rangle\,,\end{aligned} \tag{2.22}$$

and the bosonic excitation number $\langle N\rangle$ can be calculated to

$$\langle\hat{N}\rangle = |\alpha(t)|^2 = 4|\alpha|^2\sin^2\left(\frac{\omega t}{2}\right). \tag{2.23}$$

The maximum bosonic excitation number N_max can be calculated to

$$N_\mathrm{max} = 4|\alpha|^2 = \frac{4g^2}{\omega^2}, \tag{2.24}$$

where $\alpha = g/\omega$ was used. Although the case for $\omega_\mathrm{q} \to 0$ is a trivial one, it nevertheless gives insight into equation (2.24), showing that the temporal evolution of the bosonic excitation

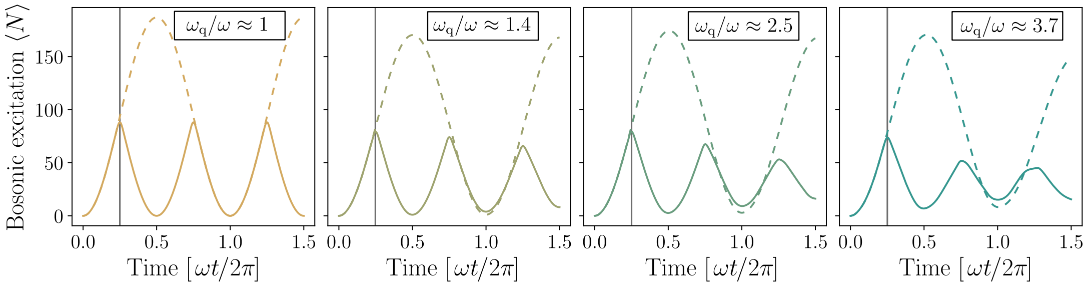

Figure 2.7: Numerical simulations of the temporal evolution of the bosonic excitation number $\langle N \rangle$ for the QRM Hamiltonian (2.5) (dashed lines) and the pQRM Hamiltonian (2.8) (solid lines) for ascending values of the ratio between the qubit frequency and bosonic mode ω_q/ω (from left to right) and fixed value for the coupling strength $g/\omega = 6.4$. The dynamics of both models overlap in the first Brillouin zone. The periodic nature of the pQRM becomes apparent due to the Umklapp process taking place at $\omega t_{\max}/2\pi = 0.25$, marked as a gray vertical line. For stronger qubit frequencies, the discrepancy between both models becomes increases.

number is solely depended on the relative coupling strength and not on the preparation of the initial state.

Another realization which can be gained in the limit of the slow qubit approximation, takes into account that the ratio between the coupling strength g and the harmonic oscillation frequency ω can be described as

$$\frac{g}{\omega} = \frac{x_0}{x_{\text{ho}}}, \tag{2.25}$$

where $x_0 = \frac{2\hbar k}{m\omega}$ is the amplitude of the classical oscillation for a vanishing lattice potential ($\omega_q \to 0$) and $x_{\text{ho}} = \sqrt{2\hbar/m\omega}$ depicts the atom specific size of the harmonic oscillator ground state wavepacket. Hence, only in the perturbative deep strong coupling regime, where $g/\omega \gg 1$, the wavepackets displacement dynamics can exceed the wavepackets size. This behavior is illustrated in Figure 2.6, where the displacement dynamics of an initially prepared state $|N = 0, \downarrow\rangle$ is compared between the perturbative deep strong coupling regime with a relative coupling strength of $g/\omega = 5$ (left panel) and the perturbative ultra strong coupling regime with the ratio $g/\omega = 0.1$ (right panel). As expected, the numerical simulation for the pDSC regime shows clear oscillations, where the wavepacket expansion exceeds the initial wavepacket size, in contrast to the pUSC regime, where no significant displacement dynamics can be observed. From an experimentalists point of view, this is intriguing since measuring the displaced atoms in the harmonic trap, while the qubit splitting is negligible, directly provides the coupling strength under consideration [27].

Moving on, the case of longer interaction times ($t > t_{\max}$) (see equation (2.20)) resulting in the emergence of a periodic version of the quantum Rabi model will be discussed. In this thesis, the boundaries of the first Brillouin zone are crossed resulting in the emergence of a periodic version of the system (pQRM). The difference between the pQRM and QRM becomes evident when observing numerical simulations of the temporal evolution of the bosonic excitation number $\langle N \rangle$ in Figure 2.7. Starting from the left to the right, the

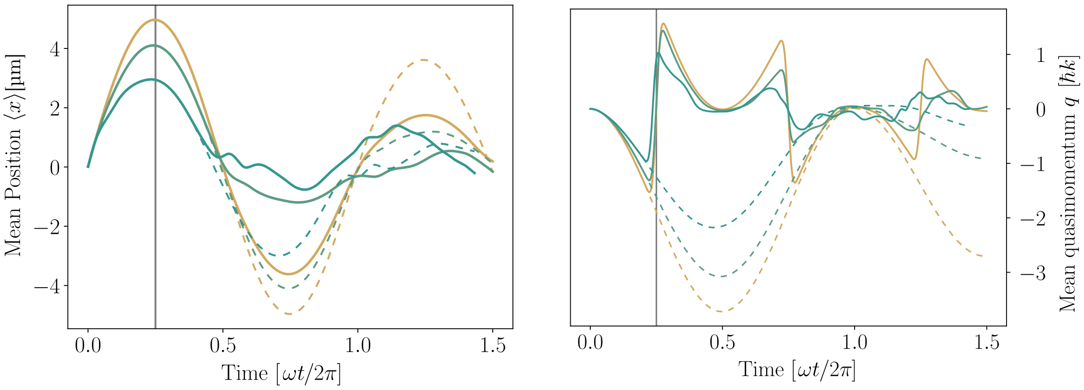

(a)

(b)

Figure 2.8: (a) Numerical simulations of the temporal evolution of the mean position $\langle x \rangle$ for the QRM Hamiltonian (2.5) (dashed lines) and the pQRM Hamiltonian (2.8) (solid lines) for ascending values of the ratio between the qubit frequency and bosonic mode ω_q/ω encoded in the color gradient from yellow ($\omega_\mathrm{q}/\omega \to 0$) to green ($\omega_\mathrm{q}/\omega \approx 5$) and fixed value for the coupling strength $g/\omega = 6.4$. Again the similarity of both models can be observed until the edge of the first Brillouin zone (gray vertical line) is reached and discrepancies arise upon this restriction is crossed. (b) Numerical simulations of the temporal evolution of the mean quasimomentum $\langle q \rangle$ with the same parameters as in (a), where the Umklapp process can be seen as a shift occurring as soon as the edge of the first Brillouin zone is reached ($q = -2\hbar k$) and the system re-enters from the other side of the dispersion relation in Figure 1.11(b) at $q = +2\hbar k$.

ratio between qubit frequency and bosonic mode ω_q/ω is increased from 1 to 3.7, while the relative coupling strength $g/\omega = 6.4$ is kept constant far in the perturbative DSC regime. It is easy to see, that as mentioned before, both models show similar dynamics up to the point where the first Brillouin zone is reached, marked in the panels as a gray vertical line at $\omega t_\mathrm{max}/2\pi = 0.25$. From this point on, a clear difference in the dynamics of both models takes place, where the Umklapp process manifests itself as 'reflection' at the edge of the first Brillouin zone (*Umklapp scattering*). Intuitively speaking, at this point, one departs from the dispersion relation (see Figure 1.11(b)) at $q = +2\hbar k$ only to subsequently re-enter again on the opposite side at $q = -2\hbar k$, which translates into skipping the second quadrant in the phase diagram during time evolution (for visualization see PhD thesis of J. Koch [53]). Comparing the panels with ascending qubit splittings ω_q the discrepancy between the models becomes larger, when ω_q/ω is increased.

Moving on to further observables, the numerical simulations for the mean position $\langle x \rangle$ and mean quasimomentum $\langle q \rangle$ are also presented for the same parameter set as in Figure 2.7. Figure 2.8 shows the resulting temporal evolution, for which the increasing qubit frequency is encoded in the color gradient from yellow ($\omega_\mathrm{q}/\omega \to 0$) to green ($\omega_\mathrm{q}/\omega \approx 5$). Again for $t < t_\mathrm{max}$ the dynamics in both models overlap, while for the case of the mean position $\langle x \rangle$ (Figure 2.8(a)), the divergence starts at later times $\omega t/2\pi \approx 0.5$ due to real space numerical simulation. Figure 2.8(b) shows the effect of the Umklapp process onto the mean quasimomentum $\langle q \rangle$, where upon reaching the edge of the first Brillouin zone a jump to the opposite mean quasimomentum takes place, and the dynamics are shifted

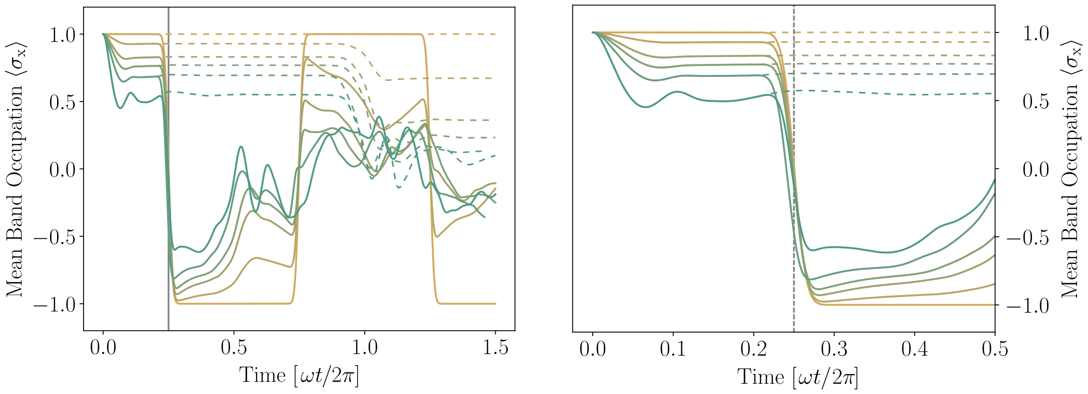

(a) (b)

Figure 2.9: (a) Numerical simulations of the temporal evolution of the mean band occupation number $\langle \sigma_x \rangle$ for the QRM Hamiltonian (2.5) (dashed lines) and the pQRM Hamiltonian (2.8) (solid lines) for the same qubit frequencies as in Figure 2.8 and fixed value for the coupling strength $^g/_\omega = 6.4$. (b) Close-up for a smaller time interval, showing the Umklapp process in detail.

upwards. This observed behavior for the mean quasi momentum $\langle q \rangle$ directly translates to the dynamics of the mean band occupation number $\langle \sigma_x \rangle$, which can be expressed in the basis of the band eigenstate $\sigma_x = |n=0\rangle \langle n=1| - |n=1\rangle \langle n=1|$, with $n = [0{,}1]$ for $p = q - 2\hbar k$ and $p = q + 2\hbar k$ respectively. Approaching the edge of the Brillouin zone leads to the remapping of bands, leading to the dynamics depicted in Figure 2.9. Again larger qubit splittings amplify the discrepancy between the two models.

The dynamics of the periodic quantum Rabi model (pQRM) are significantly influenced by the Umklapp process occurring at the edge of the first Brillouin zone, particularly when considering larger values of the qubit splitting ω_q. The theoretical foundation for this phenomenon is rooted in the mentioned derivation and the accompanying introduction of the Bloch basis. As shown, the QRM Hamiltonian in equation (2.5) is derived from the experimental Hamiltonian introduced in equation (2.8). The presented numerical differences in Figures 2.7, 2.8 and 2.9 are, therefore, a result of the respective mathematical models, among other factors.

While not significantly represented in the upcoming measurements, another approach for numerical calculation is illustrated in Figure 2.10, in order to improve the understanding of similarities and differences between the experimental and theoretical model. In this case, unlike previous numerical calculations, the Bloch basis is not integrated into the theoretical model, and there is no mapping onto the quasimomentum. Consequently, the experimental Hamiltonian is straightforwardly computed by solving the Schrödinger equation. The relative coupling strength is set far within the perturbative deep strong coupling regime ($^g/_\omega = 5$). In line with the experiment, the initial state is prepared with a momentum transfer of $p = -2\hbar k$ onto the atoms at the center of the harmonic trap. For the standard quantum Rabi model, this state corresponds to a superposition of the qubit eigenstates $|\rightarrow\rangle = {}^1/_{\sqrt{2}}\,(|\uparrow\rangle + |\downarrow\rangle)$ prepared in the vacuum mode of the bosonic field

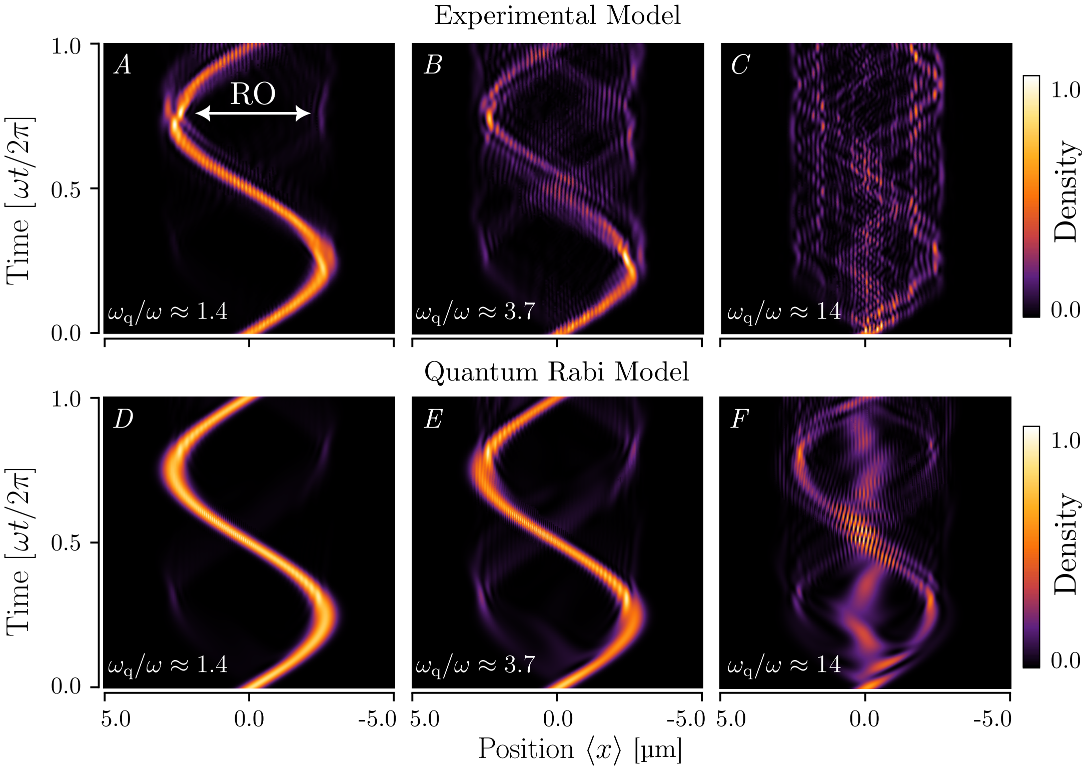

Figure 2.10: Numerical simulation of the temporal evolution of the wavepacket's probability distribution for experimental Hamiltonian in equation (2.8) (*A*, *B* and *C*) and the standard QRM in equation (2.5) (*D*, *E* and *F*). The relative coupling strength is far in the perturbative deep strong coupling regime ($g/\omega = 5$), while the ratio between qubit frequency and bosonic mode is increased from left to right ranging from $\omega_q/\omega = 1.4$ to $\omega_q/\omega = 14$.

$|N = 0, \rightarrow\rangle$. The calculations are done in temporal units of the bosonic mode frequency $\omega t/2\pi$.

Results for the experimental model are displayed in the upper panels *A*, *B*, and *C* of Figure 2.10, illustrating the temporal evolution of the wavepacket's probability distribution as two-dimensional density plots. The ratios between the qubit splitting and the harmonic oscillation frequency are varied from left to right (ranging from $\omega_q/\omega = 1.4$ to $\omega_q/\omega = 14$). Similar results for the standard quantum Rabi model (as per equation (2.5)) are presented in the lower panels *D*, *E*, and *F*, using the same parameters for the relative coupling strength and qubit frequency as in the panels above.

A qualitative comparison between both models reveals similarity for small values of ω_q/ω (*A* and *D*), where the dynamics resemble those of a harmonic oscillation, with minor contributions of Rabi oscillations (RO) between the respective momentum states $\pm 2\hbar k$. As the qubit frequency increases, the Rabi oscillations between the momentum states become more pronounced, resulting in the formation of an 'eight-shaped' silhouette in the probability distribution presented in panel *B* and *E*.

The final two panels *C* and *F* depict the scenario where the qubit frequency dominates over all energies in the system ($\omega_\mathrm{q}/\omega \simeq 14$ and $\omega_\mathrm{q}/g \simeq 3$). In this scenario, the high qubit frequency leads to a probability distribution that equally combines the features of Rabi- and harmonic oscillations.

In all panels, the deviation of the experimental model from the quantum Rabi model becomes apparent after extended temporal evolution ($\omega t/2\pi > 0.25$), and this deviation amplifies with increasing ratios of ω_q/ω. While the case of a moderate qubit frequency still shows qualitative similarities in panels *A* and *D*, the case of an extremely large qubit frequency ($\omega_\mathrm{q}/\omega \simeq 14$) implies vastly different dynamics when comparing panel *C* to panel *F*. In this regime, even for short interaction times, the wavepacket's probability distribution shown in panel *C* displays a unique appearance, with a greater sense of 'localization' in specific lattice sites. One possible explanation for this behavior can be derived by comparing the available energies. Here, the ratio between the two-photon recoil energy E_2ph and the band gap energy $E_\mathrm{Qubit} = \hbar\omega_\mathrm{q}$ given by the four-photon lattice potential $V = 2\omega_\mathrm{q}$ can be expressed as:

$$\frac{E_\mathrm{2ph}}{\hbar\omega_\mathrm{q}} = \frac{\frac{2\hbar^2 k^2}{m}}{\hbar\omega_\mathrm{q}}. \tag{2.26}$$

Substituting $k = mg^2/2\hbar\omega$ from equation (2.17) leads to the relation

$$\frac{E_\mathrm{2ph}}{\hbar\omega_\mathrm{q}} = \frac{g^2}{\omega_\mathrm{q}\omega} = \left(\frac{g}{\omega}\right)^2 \left(\frac{\omega_\mathrm{q}}{\omega}\right)^{-1} \tag{2.27}$$

Interestingly, the first term in equation (2.27) represents the squared relative coupling strength, denoted as $g/\omega = 5$ far in the pDSC regime, while the second term represents the ratio between the bosonic mode frequency ω and the qubit frequency ω_q. In simpler terms, increasing the qubit's frequency, as depicted in Figure 2.10, reduces the ratio $E_\mathrm{2ph}/\hbar\omega_\mathrm{q}$.

From a more physical perspective, a constraint arises when the depth of the four-photon potential, which determines the qubit's frequency, reaches a threshold at which the atomic wave packet no longer extends beyond it. This condition ($V \gg E_\mathrm{2ph}$) leads to a stronger influence of tunneling effects, which is a possible explanation for the localization phenomena presented in panel *C*. A natural limitation in the experimental model becomes apparent here. As a brief outlook for the use of very strong four-photon lattice potentials, it may be more suitable to consider localized Wannier states rather than the Bloch basis, as is discussed more thoroughly in [110]. This is an important insight that is worth keeping in mind, especially since the quantum simulation presented here is conducted for larger than full-cycle temporal dynamics ($\omega t/2\pi > 1$). Due to this extended interaction time, the localization effects described above, hence the discrepancy between the system Hamiltonian and the quantum Rabi Hamiltonian, become more pronounced for large qubit frequencies. Consequently, besides the experimental limitation of heating the atomic BEC through near-infrared photon scattering from strong lattice potentials during prolonged interaction times, there is also a physical reason not to use excessively strong lattice potentials during the time evolution of the quantum simulation, as this may lead to potential limitations of the Bloch basis.

2.3 Analogy to Superconducting Fluxonium Systems

Moving on to the final section of the theoretical background a digression into superconducting (SC) qubit systems will be presented. The reason for this is an intriguing analogy between the single-particle Hamiltonian in equation (2.8) and the one describing a fluxonium qubit system [91], which could potentially serve as a foundation for simulating superconducting qubit systems through the experiment presented here. SC qubits offer a promising platform for building powerful quantum computers. They are designed using a cooled LC circuit, serving as an artificial two level atom, in which the superconducting condensate emulates the quantum behavior of electrons within atoms.
The LC circuit consists of two main components: an inductance (L) and a capacitor (C). The inductance carries a current I that simulates the oscillation velocity of electrons in their orbits, while the voltage across the capacitor C corresponds to the force $\mathbf{F}$ acting on the 'electron'. To achieve quantum behavior, these superconducting circuits are cooled to extremely low temperatures. Despite their microscopic nature, they can be macroscopically scaled up to sizes on the order of millimeters. This scalability is a remarkable feature, as it allows for the design and manipulation of quantum states at a macroscopic level. For instance, the size of a typical superconducting qubit may be on the order of $1\,\mathrm{mm}$, making it approximately seven orders of magnitude larger than an actual hydrogen atom ($\sim 0.1\,\mathrm{nm}$).

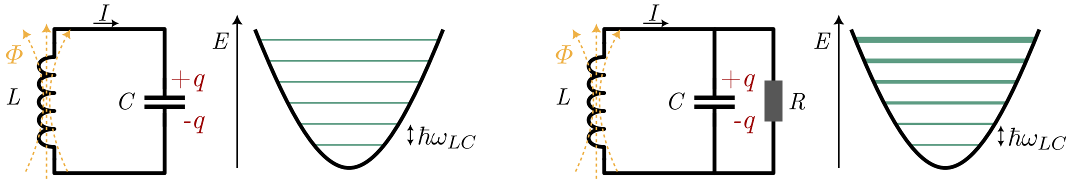

(a)

(b)

Figure 2.11: (a) Simple LC circuit scheme with an inductance L, capacitor C and the charge $\pm q$. The flux ϕ can be understood as the positional coordinate in the system. The resulting energy spectrum with the corresponding energy spacing $\hbar\omega_{LC} = \hbar/\sqrt{LC}$ is depicted on the right. (b) The dissipation in the system is added with a resistor R which results in the broadening of the energy levels depicted on the right.

The schematic of a simple LC circuit is presented in Figure 2.11(a), where the flux $\phi = LI$ can be understood as the position of the particle and $q = CV$ depicts the charge. Essentially, the resulting energy spectrum is that of an harmonic oscillator with the commutator relation $[\hat{\phi},\hat{q}] = i\hbar$ and the energy splitting $\hbar\omega_{LC} = \hbar/\sqrt{LC}$ (as shown in the right panel). In order to account for dissipation, the resistor R is introduced, which leads to a broadening of the energy levels

$$E_n = \hbar\omega_{LC}\left[n\left(1+\frac{i}{2\mathscr{Q}}\right)+\frac{1}{2}\right], \tag{2.28}$$

where $\mathscr{Q} = RC\omega_{LC}$ is the quality factor with $n \in \mathbb{N}$ as the number of the respective energy level, resulting in a lifetime decrease (as seen in Figure 2.11(b)).
The coupling between natural atoms in a vacuum is quite small compared to the coupling

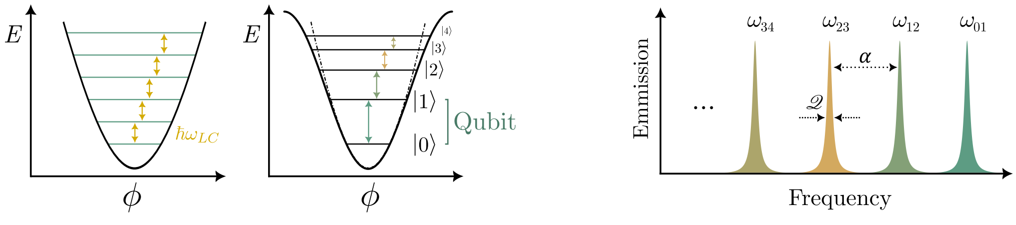

(a) **(b)**

Figure 2.12: (a) Introducing a non-linearity with a different potential shape as shown on the right, results in different energy splittings for the lower energy levels. The two lowest energy levels $|0\rangle$ and $|1\rangle$ with the transition frequency ω_{01} can be used as an effective two-level system. (b) Emission spectrum of the non-linear energy level scheme where the width $\mathscr{Q}$ corresponds to the quality factor and the distance between two frequency peaks $\alpha = {}^{|\omega_{01}-\omega_{12}|}/_{\omega_{01}}$ is the non-linearity ratio.

between two circuits, which can be connected either with a capacitor (capacitive coupling) or an inductance (inductive coupling). However the linearity of the equidistant energy spacings $\hbar\omega_{LC}$ only allows for driving the system in the ground state, hence a non-linearity has to be introduced to generate an effective two-level system.
Figure 2.12(a) shows the effect of such a potential, where in contrast to the left panel, with equidistant energy levels, now different frequencies $\omega_{01} \neq \omega_{12}$ between subsequent levels arise. Restricting the dynamics to the two lowest energy levels $|0\rangle$ and $|1\rangle$ allows the realization of an effective two-level system, hence a qubit. The distance between two frequencies (see also in Figure 2.12(b)) is defined as the *non-linearity ratio* α

$$\alpha = \frac{|\omega_{01} - \omega_{12}|}{\omega_{01}} \tag{2.29}$$

and is desired to be as large as possible. In superconducting qubit experiments the product $\mathscr{Q} \cdot \alpha$ has to be optimized in order to realize large enough coherence times where the different transition frequencies are as far separated as possible. These requirements are well fulfilled with a so called Josephson tunnel junction, for which Figure 2.13(a) displays the basic schematic, where in essence two superconductors are separated by a thin barrier. The current I flowing through a Josephson junction can be described as

$$I = I_0 \sin(\phi/\phi_0), \tag{2.30}$$

where $\phi_0 = {}^{\hbar}/_{2e}$ is the flux quantum. The Josephson inductance is defined as $L_J = {}^{\phi}/_{I_0}$, where for small flux values, the dashed line in the left panel of Figure 2.13(b) shows a linear inductance scaling with $I = \phi/L_J$. Observing the bare Josephson potential

$$U = -E_J \cos(\phi/\phi_0), \tag{2.31}$$

which is depicted in the right panel of Figure 2.13(b), shows the deviation from the parabola of a harmonic potential, emphasizing the non-linear nature necessary for the creation of the qubit. With this, a simple tool kit consisting of a capacitor and two inductances can be

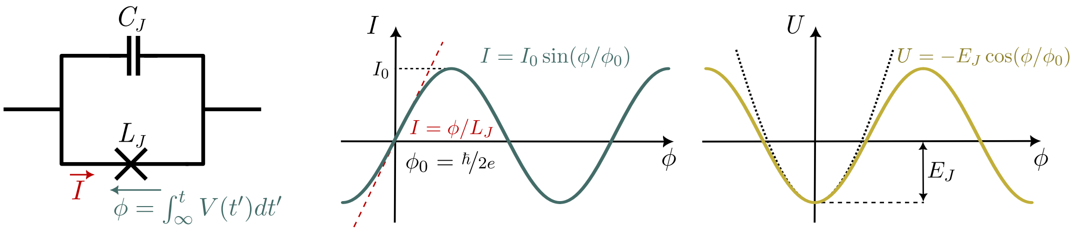

(a) **(b)**

Figure 2.13: (a) Schematic of a Josephson circuit. (b) The Josephson current I (left panel) and the Josephson potential U (right panel) versus the flux ϕ. For small flux values ($\phi < \phi_0$) an inductive behavior can be observed (red dashed line) for the current $I = \phi/L_J$, while for larger flux values an oscillation occurs. The bare Josephson potential shows the deviation from a harmonic potential, making it suitable for the creation of the non-linear energy level spacing for the creation of an effective two-level system.

used to create a superconducting circuit simulating an artificial atom. The characteristic energies for the capacitor (E_C), the inductance (E_L) and the Josephson junction (E_J) can be written as

$$E_C = \frac{e^2}{2C} \qquad E_L = \frac{\hbar^2}{4e^2 L} \qquad E_J = \frac{\hbar^2}{4e^2 L_J}. \tag{2.32}$$

Changing the ratios E_J/E_C and E_L/E_J creates a plethora of potential landscapes which can be used to engineer different atoms. In the following the derivation of a Hamiltonian for a so called fluxonium qubit will be presented, which then later on, presents an interesting analogy to the system Hamiltonian in equation (2.8).

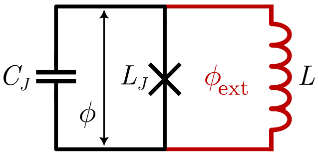

Figure 2.14: Schematic of a fluxonium qubit, where ϕ is the phase across the Josephson junction, C_J is the capacitance, L_J and L the corresponding inductances and ϕ_{ext} is the external magnetic flux.

A fluxonium qubit is a superconducting circuit consisting of a capacitance, an inductance and a Josephson junction, where the energies are ordered in $E_J > E_C > E_L$ (schematic depicted in Figure 2.14). The flux through an active node can be described by

$$C\ddot{\phi} = -\frac{\phi}{L} - \xi \sin\left(\frac{2\pi\left(\phi + \phi_{\text{ext}}\right)}{\phi_0}\right), \tag{2.33}$$

where ϕ is the phase across the Josephson junction, acting as the dynamical variable representing the qubit state, L is the inductance of the Josephson junction, ξ is a dimensionless parameter representing the coupling strength between superconducting islands, ϕ_{ext} is the external magnetic flux threading the qubit loop and $\phi_0 = {}^{\hbar}\!/_{2e}$ is the reduced flux quantum. The corresponding scheme is depicted in Figure 2.14. From this, the Lagrangian of the system can be written as

$$\mathcal{L} = \frac{C}{2}\dot{\phi}^2 - \frac{\phi^2}{2L} + \frac{\xi\phi_0}{2\pi}\cos\left(\frac{2\pi\left(\phi + \phi_{\text{ext}}\right)}{\phi_0}\right). \tag{2.34}$$

The canonical charge $q = {}^{\partial\mathcal{L}}\!/_{\partial\dot{\phi}} = C\dot{\phi}$ is used to obtain the Hamiltonian by the Legendre transformation

$$\begin{aligned} \hat{H} &= q\dot{\phi} - \mathcal{L} \\ &= q\left(\frac{q}{C}\right) - \left[\frac{C}{2}\left(\frac{q}{C}\right)^2 - \frac{\phi^2}{2L} + \frac{\xi\phi_0}{2\pi}\cos\left(\frac{2\pi(\phi + \phi_{\text{ext}})}{\phi_0}\right)\right] \\ &= \frac{q^2}{2C} + \frac{\phi^2}{2L} - \frac{\xi\phi_0}{2\pi}\cos\left(\frac{2\pi(\phi + \phi_{\text{ext}})}{\phi_0}\right). \end{aligned} \tag{2.35}$$

Introducing the number of excess Cooper pairs on the capacitive electrodes $n = {}^{q}\!/_{2e}$ [111], $E_C = {}^{2e}\!/_{8C}$, $E_L = {}^{1}\!/_{L}$ and $E_J = {}^{\xi\phi_0}\!/_{2\pi}$, results in the fluxonium Hamiltonian [36]

$$\hat{H} = 4E_C\hat{n}^2 + \frac{1}{2}E_L\hat{\phi}^2 - E_J\cos\left(\frac{2\pi(\hat{\phi} + \phi_{\text{ext}})}{\phi_0}\right), \tag{2.36}$$

which can be further simplified into a reduced form [91]

$$\hat{H} = 4E_C\left(\frac{\hat{q}}{2e}\right)^2 + \underbrace{\frac{1}{2}E_L\hat{\phi}^2 - E_J\cos\left(\hat{\phi} + \phi_{\text{ext}}\right)}_{V(\hat{\phi})}. \tag{2.37}$$

The equation above describes a particle with a mass inversely proportional to E_C in the potential $V(\hat{\phi})$. The tunability of this potential allows for creation of different potentials, leading to significantly different systems depicted in Figure 2.15. It is easy to see, that a connection to the combined potential in Figure 2.5 can be drawn from earlier sections.
In the following, a fixed external magnetic flux $\phi_{\text{ext}} = \pi$ is chosen to show the similarity between the superconducting circuit model (equation (2.37)) and the periodic quantum Rabi Hamiltonian $\hat{H}_{\text{exp}}$

$$\hat{H}_{\text{exp}} = \frac{m\omega^2}{2}\hat{x}^2 + \frac{\hat{p}^2}{2m} + \frac{V}{2}\cos(4k\hat{x}). \tag{2.38}$$

For the fluxonium system the charge $\hat{q}$ and flux $\hat{\phi}$ commute with

$$\underbrace{[\hat{\phi}, \frac{\hat{q}}{2e}\hbar]}_{\text{Fluxonium}} = i\hbar = \underbrace{[\hat{x},\hat{p}]}_{\text{Experiment}}, \tag{2.39}$$

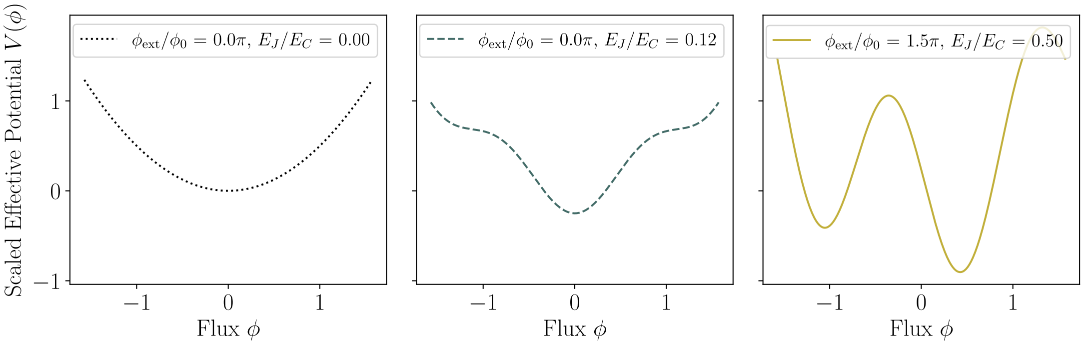

Figure 2.15: Numerical simulations of the scaled effective potential $V(\phi)$ for different ratios of the external magnetic flux and the reduced flux quantum ϕ_{ext}/ϕ_0 and different values for the ratio of the Josephson energy and the capacitance energy E_J/E_C. The simple case where both are zero describes a harmonic potential (black dotted line), while increasing the Josephson energy E_J shows faster oscillations superimposed to the harmonic potential (green dashed line). The effect of the external flux ϕ_{ext} is visible as a shift along the x axis (yellow solid line).

where in case of the experiment's system Hamiltonian the position $\hat{x}$ and momentum $\hat{p}$ fulfill the commutation relation. The second and third term can be mapped fairly easy, by rescaling the positional parameter $\hat{\phi} \overset{!}{=} 4k\hat{x}$, resulting in the harmonic potential

$$\frac{m\omega^2\hat{x}^2}{2} \underset{\hat{\phi}=4k\hat{x}}{=} \frac{m\omega^2}{2}\left(\frac{\hat{\phi}}{4k}\right)^2 \overset{!}{=} \frac{E_L}{2}\hat{\phi}^2, \tag{2.40}$$

yielding the inductance energy

$$E_L = \frac{m\omega^2}{16k^2}. \tag{2.41}$$

Using the same scaling factor shows the similarity between the third terms of each Hamiltonians, where a simple formalism between the potential depth V in equation (2.38) and the Josephson energy E_J in equation (2.37) can be found

$$E_J = \frac{V}{2}. \tag{2.42}$$

Substituting $\hat{x} = \hat{\phi}/4k$ and using equation (2.39) results in

$$i\hbar = \left[\frac{\hat{\phi}}{4k}, \hat{p}\right] = \frac{\hat{\phi}}{4k}\hat{p} - \hat{p}\frac{\hat{\phi}}{4k} = \left[\hat{\phi}, \frac{\hat{p}}{4k}\right] \overset{!}{=} \left[\hat{\phi}, \frac{\hat{q}}{2e}\hbar\right], \tag{2.43}$$

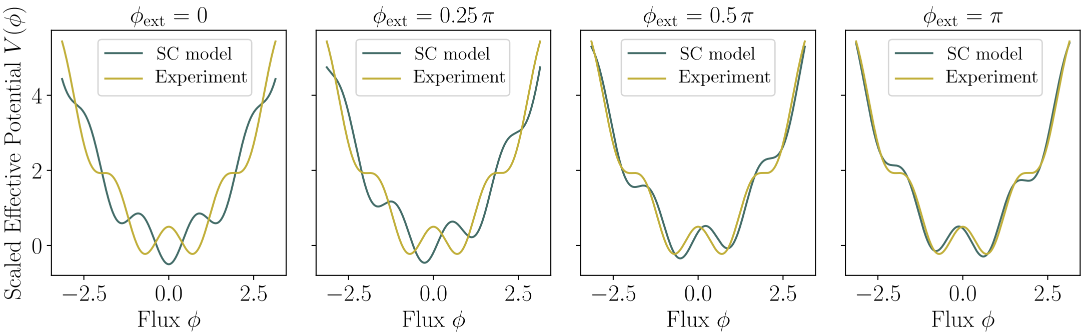

Figure 2.16: Numerical simulations of the scaled effective potential $V(\phi)$, where $\hat{\phi} = 4k\hat{x}$ was used, for different external flux values ϕ_{ext}. The derived energies E_C, E_L and E_J are used resulting in similar shape of the effective potential for the experiment's system Hamiltonian (yellow solid line) and fluxonium system (green solid line).

which leads to $\hat{p} = \frac{2\hbar k}{e}\hat{q}$.
With this, the kinetic energy term $E_{\text{kin}} = \hat{p}^2/2m$ of equation (2.8) writes as

$$\frac{\hat{p}^2}{2m} = \frac{1}{2m}\left(\frac{4\hbar k}{2e}\hat{q}\right)^2 \overset{!}{=} 4E_C\left(\frac{\hat{q}}{2e}\right)^2, \tag{2.44}$$

resulting in the capacitor's energy E_C

$$E_C = \frac{2\hbar^2 k^2}{m}, \tag{2.45}$$

which resembles the two-photon recoil energy E_{2ph}.
Incorporating the resulting energy terms E_C, E_L, and E_J into equations (2.45), (2.41), and (2.42) produces Figure 2.16, which illustrates the similarity between both systems. The numerical simulations utilize the rescaled positional term $\hat{\phi} = 4k\hat{x}$ and includes various values for the external flux (ranging from $\phi_{\text{ext}} = 0$ to $\phi_{\text{ext}} = \pi$ from left to right), thereby demonstrating the comparability of the two systems. Once again, changing the external flux ϕ_{ext} causes shifts in the scaled effective potentials $V(\phi)$ along the x-axis, with an observable overlap occurring in the case of $\phi_{\text{ext}} = \pi$. For arbitrary flux values ϕ_{ext}, it can be demonstrated (as shown in the Appendix) that a unitary basis transformation maps the fluxonium Hamiltonian onto the aforementioned system Hamiltonian in the quasimomentum basis (2.38), further reinforcing the resemblance between these two systems.
In order to derive the resulting coupling strength g in such a superconducting fluxonium setup, the product

$$E_L \cdot E_C \overset{(2.45)}{\underset{(2.41)}{=}} \frac{m\omega^2}{16k^2} \cdot \frac{2\hbar^2 k^2}{m} = \frac{\hbar^2\omega^2}{8} \rightarrow \hbar\omega = \sqrt{8E_L E_C} \tag{2.46}$$

is taken, and with

$$\frac{k^2}{m} = \frac{E_C}{2\hbar^2} \overset{(2.17)}{\rightarrow} g^2 = \frac{k^2 2\hbar\omega}{m} \overset{(2.46)}{=} \frac{2E_C\sqrt{8E_LE_C}}{2\hbar^2} \rightarrow \hbar g = \left(8E_LE_C^3\right)^{1/4} \tag{2.47}$$

the resulting normalized coupling strength is calculated to

$$\frac{g}{\omega} = \left(\frac{8E_LE_C^3}{64E_L^2E_C^2}\right)^{1/4} = \left(\frac{E_C}{8E_L}\right)^{1/4} \simeq 1.93, \tag{2.48}$$

describing a superconducting fluxonium system.

Table 2.1: Comparison of the resulting energies E_J, E_C and E_L between the system Hamiltonian and the fluxonium model, where experimental parameters are used in equation (2.42), (2.45) and (2.41). Representative energy values for the superconducting fluxonium setup are taken from [91].

Energy comparison between the systems			
Energy $[1/\hbar]$	E_J	E_C	E_L
Experiment	$0 - 5.5\,\mathrm{kHz}$	$15\,\mathrm{kHz}$	$44\,\mathrm{kHz} - 80\,\mathrm{kHz}$
Fluxonium [91]	$4.76\,\mathrm{GHz}$	$0.065\,\mathrm{GHz}$	$7.07\,\mathrm{GHz}$

With the above introduction and the demonstrated analogy between the two systems, it is potentially conceivable to simulate a superconducting qubit system using the present experiment. What is particularly interesting in this context is that the coupling strength at which this analog quantum simulation would occur would also be in the deep strong coupling regime. This could potentially reveal intriguing phenomena within the realm of superconducting qubit platforms, offering a powerful tool for quantum computation.

CHAPTER 3

Experimental Setup

In this chapter, a brief discussion of the experimental apparatus will be presented. Firstly, the vacuum system will be presented, followed up by the setup of the magneto-optical trap, which is used for pre-cooling the atoms in order to subsequently load them into an optical dipole trap. After a large enough number of atoms is loaded into the optical dipole trap, forced evaporation cooling takes place resulting in the creation of a Bose-Einstein condensate. Lastly, the optical lattice laser setup is presented, which is used to prepare and manipulate the ultra-cold atoms, also serving as the periodic potential for the creation of an effective two-level system.

For more detailed descriptions of each presented system, the reader is kindly referred to previous works conducted on the experiment [53, 112–114].

3.1 Vacuum System

In order to maintain low collision rates and achieve low temperatures for the atomic ensemble, all experiments are conducted within an ultra-high vacuum apparatus. The main chamber, depicted in Figure 3.1, includes dipole trapping optics (Zn-Se lenses) inside the chamber to ensure tight trapping confinement in propagation direction, which can be mechanically adjusted by manipulators and optical access points. A cylindrical fore chamber houses vacuum pumps and an ionization vacuum gauge. Combining an ion getter pump (*Meca2000 VTS 25l/s*) and a titanium sublimation pump (*Riber TSP2*) in conjunction with a mechanical turbo-molecular pump facilitates the achievement and maintenance of ultra-high vacuum, which is typically at a pressure of $3 \cdot 10^{-10}$ mbar. During experimental operation, only the ion getter pump is used to maintain this pressure level and is being monitored using an ionization vacuum gauge (*Leybold Thermovac TR 211*). Wear and tear effects of the ion getter pump lead to the release of gaseous molecules, which then have to be captured by applying a new titanium getter layer every few months. A multitude of flanges are connected to the spherical main chamber to ensure optical access for absorption imaging (CF DN63) and laser-cooling (CF DN40, CF DN16) and one, which is used to hold the three rubidium dispensers and the horizontal axis for guiding the dipole trapping laser beam (CF DN40). Heating the dispenser to approximately $550\,^{\circ}\mathrm{C}$ can be done by applying a current of about $4.2\,\mathrm{A}$, which then leads to reduction of the chemical trapping agent (Rb2CrO4) in the dispensers, hence releasing atomic rubidium into the vacuum chamber. Modulating this current during the experimental cycle allows for precise

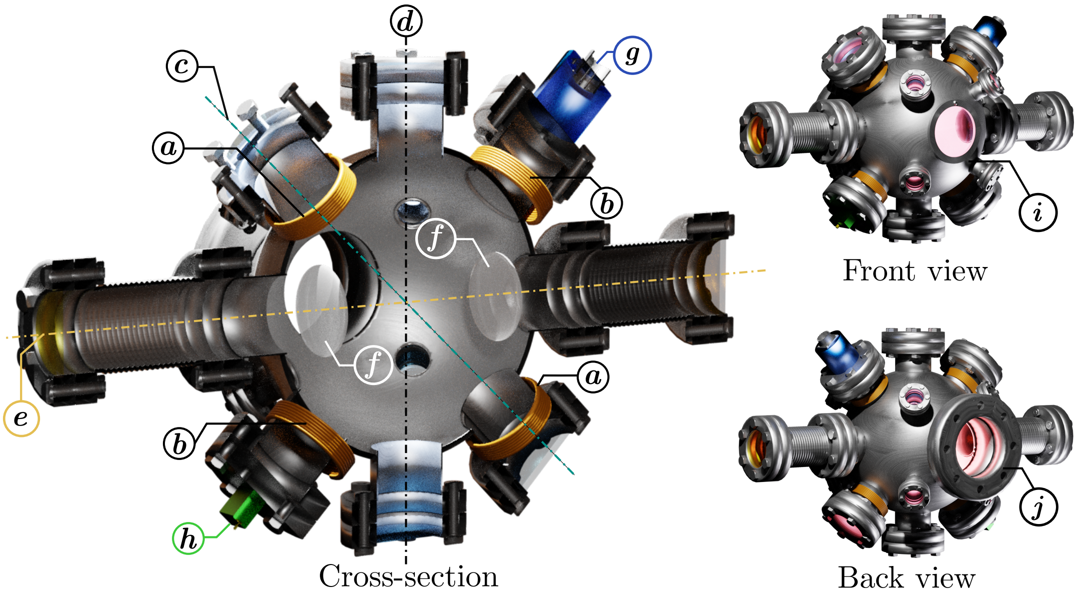

Figure 3.1: Cross-section of the main experimental vacuum chamber (left) with front- and back view depicted as smaller images on the right. Alphabetical letters correspond to the following devices: Coil pairs of the magneto-optical trap (MOT) (**a**) and gravity compensation coils (**b**), main optical axes for the MOT (**c**), lattice laser (**d**) and optical dipole trap (**e** with focusing lenses (**f**) located within the chamber). The rubidium dispensers (**g**) are located in the top right corner of the image, while on the mirrored left side, the microwave antenna (**h**) can be seen. The not sliced front- and back view images show the optical access for absorption imaging (**i**) and the port connecting main chamber to the fore chamber (**j**).

dosing of rubidium into the background gas, while the trapping agent helps to prevent contamination of the chamber by the release of unwanted gases.

3.2 Magneto-optical Trap

The released ^{87}Rb isotopes, present in the heated sample with a $27.835\,\%$ abundance [115], are cooled and trapped in the center of the spherical chamber by a magneto-optical trap. Although this specific isotope technically decays into ^{87}Sr [68] the long half life of $\simeq 50$ billion years allows for the assumption of a stable isotope [116].

The used transition addressed by the *cooling laser* is presented in Figure 3.3(a), where the line width between the two states $|5S_{1/2}, F = 2\rangle$ and $|5P_{3/2}, F = 3\rangle$ is $\Gamma_c = 6.0666(18)\,\mathrm{MHz}$. Non-resonant scattering of light leads to atoms decaying into the $|5S_{1/2}, F = 1\rangle$ lower hyperfine state. This acts as a dark state, when only the cooling laser is on, which results in atoms being effectively lost for the cooling process. For this, a *repumping laser* is used to drive the transition between $|5S_{1/2}, F = 1\rangle$ and $|5P_{3/2}, F = 2\rangle$ (Figure 3.2(a)), recovering atoms for the cooling process.

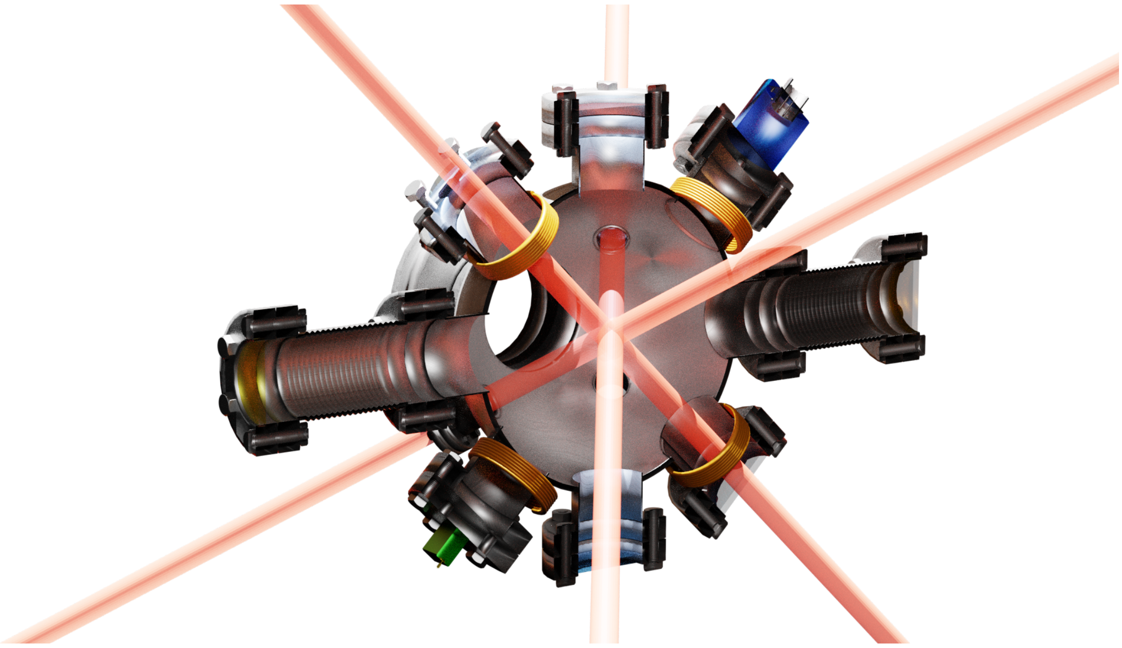

3.2.1 Laser Cooling

Repumping Laser

A self built interference filter laser (IFL) [117] with a maximum output power of around $50\,\mathrm{mW}$ at a diode current of $I_d = 100\,\mathrm{mA}$ is used to return atoms from the dark state to the cooling process. The frequency stabilization of the repumping laser, which also serves as a frequency offset stabilization for the cooling laser is depicted in Figure 3.2(b), where right after passing the optical Faraday isolator, which reduces back reflection to the laser diode, a beam path is separated for frequency stabilization. This, in essence, consists of the modulation of the diode current I_d with $25\,\mathrm{MHz}$, leading to the creation of side band signals used for frequency stabilization [118]. For a more detailed description of the implemented scheme, the reader is kindly referred to earlier works conducted on the experiment [119]. Another beam path is separated from the main path, in order to generate a beating signal used to reference the frequency offset between repumping- and cooling laser, where the detailed mechanism will be presented in the subsequent section for the cooling laser setup. A combination of a mechanical shutter (*Melles Griot SafeClose*) placed in the focal plane of a 1:1 telescope, subsequently followed by an acousto-optical modulator (AOM *Isomet 1205C-1*) ensures the suppression of stray light, while still allowing quick shutdown- and rise times on a nanosecond scale. In order to have a homogeneous beam intensity along the propagation axis, a pinhole with a diameter of $50\,\mu\mathrm{m}$ is used in the focal plane of an enlarging telescope, optimizing transversal mode selection.

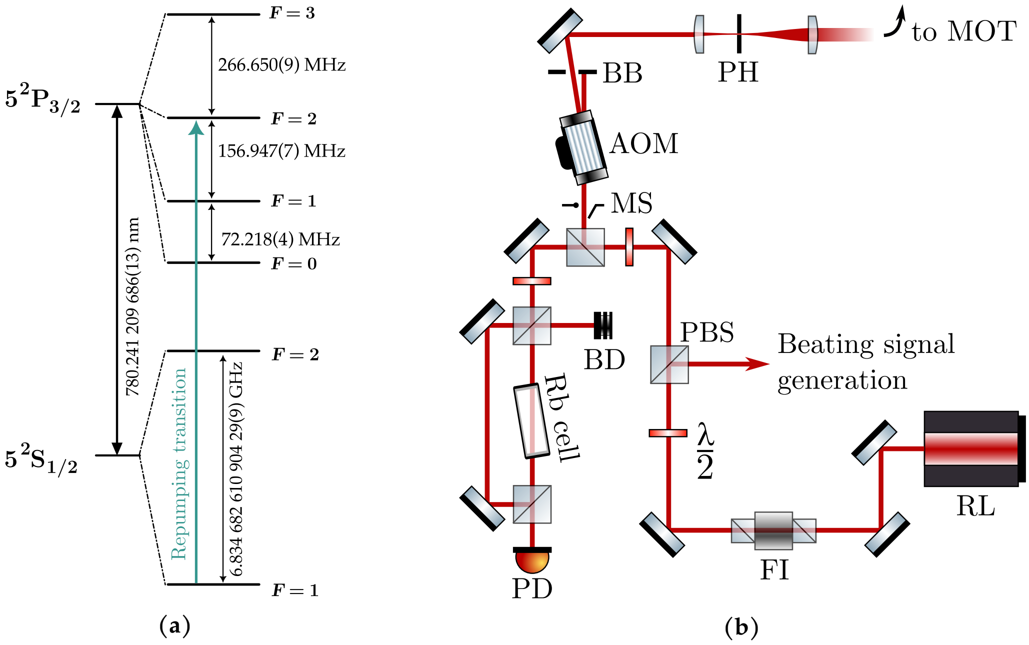

Figure 3.2: (a) Rubidium-87 D2 transition (obtained from [68]), where the repumping transition from $|5S_{1/2}, F = 1\rangle$ to $|5P_{3/2}, F = 2\rangle$ is marked in green. (b) Experimental setup for frequency stabilization and mode selection used for the repumping laser (RL). After passing an optical Faraday isolator (FI), the main beam is split at a polarizing beam splitter (PBS) and guided to the beating signal generation. Another PBS is used to take a small fraction for the frequency modulation spectroscopy setup including a photo-diode (PD) and a beam dump (BD). The main beam passes a mechanical shutter (MS) and an acousto-optical modulator (AOM) where the zeroth order is blocked by a beam blocker (BB). Finally a pinhole (PH) in the focus of an enlarging telescope is used for mode selection. The repumping laser light is overlapped with the cooling laser light and guided to the vacuum setup.

Cooling Laser

The laser system used to drive the cooling transition is a combination of a grating-stabilized diode laser equipped with a trapezoidal diode (*Toptica DLX 110*). Applying diode currents of around 1.4 A generates a maximum output power of around 350 mW at a wavelength of $\lambda = 780\,\mathrm{nm}$. The setup used in the experiment is depicted in Figure 3.3(b). Again, an optical Faraday isolator and the combination of a mechanical shutter with an AOM is used for similar reasons as shown before, however this time, the shown spectroscopy setup only serves as a rough monitoring tool. As mentioned before, the actual frequency stabilization of the cooling laser is realized by creating a beating signal between the two lasers. Here, both beams are guided together into a single mode optical fiber and detected by a fast photo diode (*Alphalas UPD-50-SP*) with a bandwidth of 7 GHz. The resulting beating signal between the two lasers at 6.568 GHz is then down-converted (*Rohde & Schwarz SMT06*) and again used as a control signal for frequency stabilization realized by a frequency-to-voltage converter. By implementing this scheme, a significantly wider tunable frequency range can be achieved compared to a fixed stabilization protocol. To provide a more comprehensive

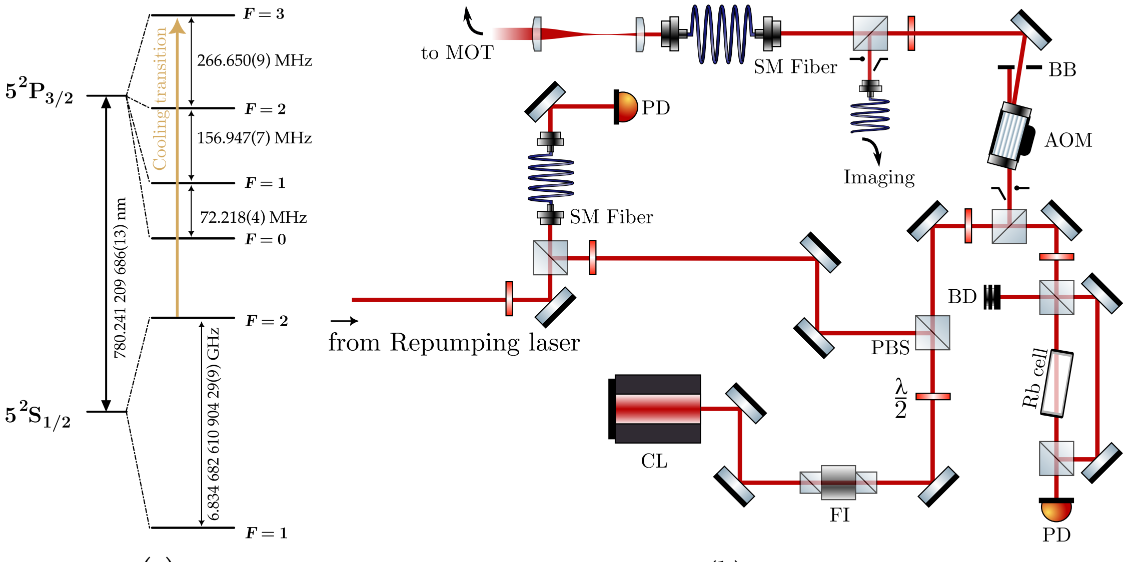

(a) (b)

Figure 3.3: (a) Rubidium-87 D2 transition (obtained from [68]), where the cooling laser transition from $|5S_{1/2}, F = 2\rangle$ to $|5P_{3/2}, F = 3\rangle$ is marked in yellow. (b) The structure for the cooling laser (CL) is fundamentally similar to the one depicted in Figure 3.2(b), with the exception that a single-mode fiber (SM fiber) is used in this case for mode selection of the cooling laser light. Just like the repumping laser, partial beams are utilized for spectroscopy purposes and for generating the beating signal by superimposing the light from both lasers on a polarizing beam splitter. The combined light is then directed onto a fast photo diode (PD) through a single-mode fiber. Another partial beam is extracted for absorption imaging purposes.

and detailed explanation of the creation and properties of the beating signal, please refer to the work of G. Ritt in his PhD dissertation [119]. This scheme enhances the cooling laser's versatility, as the frequency can be easily adjusted to resonance at the end of each experimental cycle, allowing for absorption imaging without the need for an additional detection laser. To achieve this, a polarization beam splitter (PBS) is utilized to direct a small portion of the reflected light into a single mode fiber for imaging, while the majority of the transmitted light is directed into another single mode fiber for mode selection. Before entering the vacuum chamber, a widening telescope is used to increase the beam diameter of the cooling laser, such that it can be overlapped with the repumping laser. Subsequently, the two beams are split into six counter-propagating beam pairs and directed into the vacuum chamber, passing through $\lambda/4$-plates to ensure correct circular polarization. The full experimental setup for laser cooling is depicted in Figure 3.4.

3.2.2 Magnetic Trapping

After discussing the laser cooling setup, a pair of anti-helmholtz coils is attached to the flanges of the MOT's main axis on the vacuum chamber as shown in Figure 3.1 in order to create a positional dependent gradient field for atom trapping. While a more detailed explanation of its functionality can be found in the PhD dissertation of M. Leder [113]

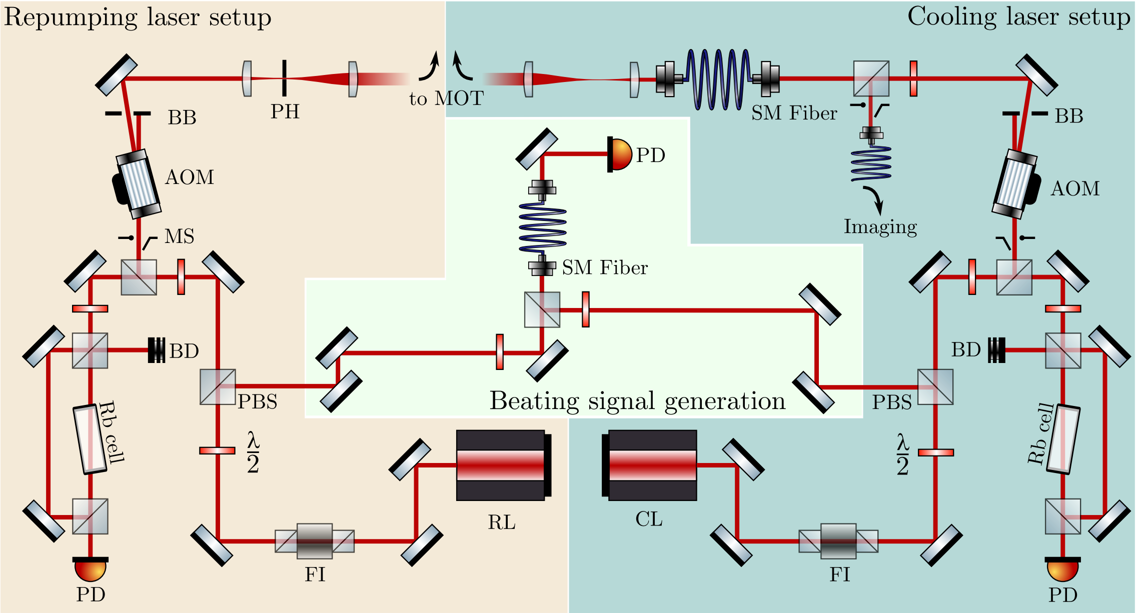

Figure 3.4: Combination of the setups of both laser systems, where the cooling laser system is depicted in forest green, the repumping laser system in orange, and the common region for generating the beating signal in light green.

and the Master thesis of L. Sitta [120], some essential properties are also presented in the following. Each coil is made up of 28 annealed copper tubing windings (*RS Pro 846-503*), which can generate high power dissipation values of up to 3 kW during the experimental cycle due to peak current values of 200 A. To ensure safe operation, the copper tubing, which has a diameter of 4 mm, is actively water-cooled and monitored by temperature sensors (*Maxim Integrated DS18S20*) and water flow sensors (*B.I.O.-TECH e.K. FCH-midi-POM*). These sensors can detect emergency situations caused by high temperatures or low water flow and shut down the power supply (Keysight 6691A) if necessary. To prevent ground loops caused by the large distance between the power supply and the experimental apparatus, differential signaling is utilized, which involves transmitting two complementary signals with equal magnitude and opposite polarity over two separate wires to reduce electromagnetic interference and noise. This ensures consistent current values are applied to the coils.

Typical experimental parameters during a cycle involve coil currents of 80 A (MOT-Phase), generating a magnetic field gradient of approximately 13.3 Gs/cm at the center of the chamber. By adding another identical pair of coils (*gravity coils*, see Fig. 3.1), the resulting quadrupole field can be used to levitate the spin-polarized BEC. To achieve even finer control over the electromagnetic potentials near the atoms, so called *offset coils* in Helmholtz configuration are used and placed around the vacuum chamber in all three dimensions.

3.3 Optical Dipole Trap

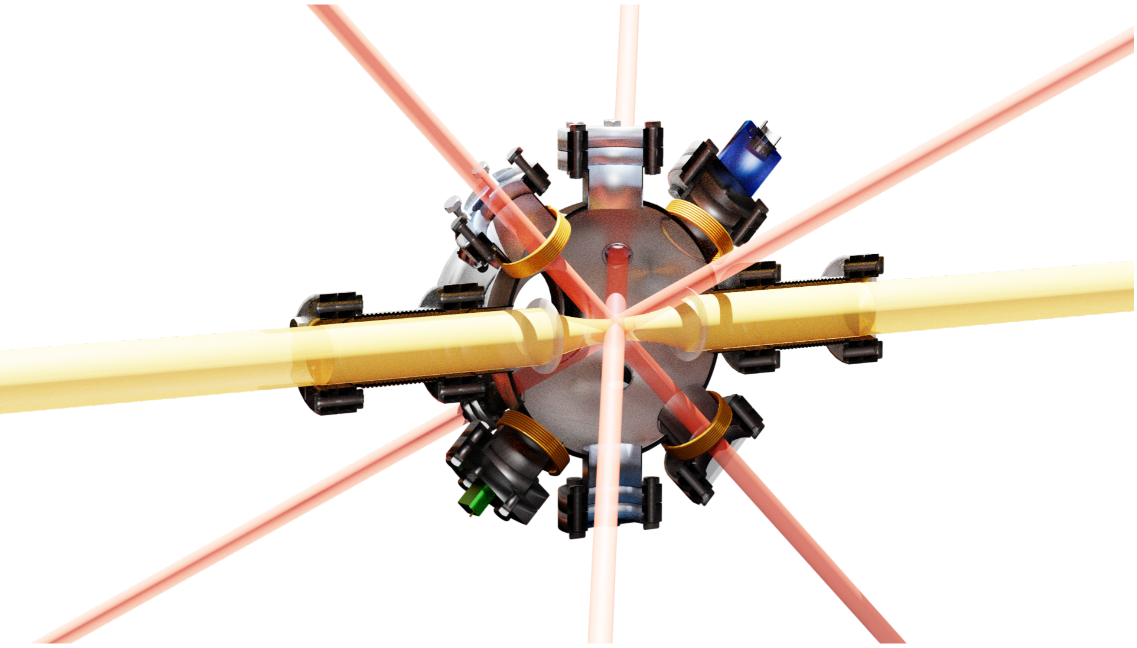

The used CO_2 laser (*Coherent GEM-50S*) with an output power of $50\,\mathrm{W}$ and a wavelength $\lambda_{\mathrm{CO_2}} = 10.6\,\mathrm{\mu m}$ generates a conservative trapping potential produced by a single focused laser beam. This trapping potential allows for effective evaporative cooling, which is necessary for creating the BEC. During this thesis, other high-power laser systems, such as Nd:YAG lasers in a crossed configuration were successfully used to evaporate the trapped atoms into a Bose-Einstein condensate. However, due to the higher scattering rate with near-infrared photons from the Nd:YAG laser beam, they fell short when it came to ramping up the optical power again to provide a harmonic potential for simulating the bosonic mode of the periodic quantum Rabi model. In contrast, the larger wavelength of the CO_2 laser provides two advantages for the experimental realization. Firstly, the high detuning compared to Nd:YAG lasers leads to very low scattering rates, around $0.006\,\mathrm{s}^{-1}$ for power values of $30\,\mathrm{W}$ typically at the start of the evaporation sequence. Secondly, due to the reciprocal scaling of Rayleigh length with wavelength $z_{\mathrm{R}} \propto 1/\lambda_{\mathrm{CO_2}}$, only a single focused laser beam is required to generate a sufficient confinement in the beams propagation direction.

Figure 3.5 shows the optical setup, where the laser beam is split into three beams by two ZnSe beam splitters, one of which is used to monitor the laser's single mode operation by the use of a Fabry-Pérot interferometer (FPI) and the other to stabilize the laser power. For this, the second beam is focused onto a photo detector (*Vigo System PC-10.6*) to measure the laser power. Due to the noise of the photo detector, a lock-in amplifier is used to improve the signal-to-noise ratio. The laser cavity is slowly modulated $(23\,\mathrm{Hz})$ by an integrated piezoelectric actuator to enable the stabilization of the laser output power by minimizing

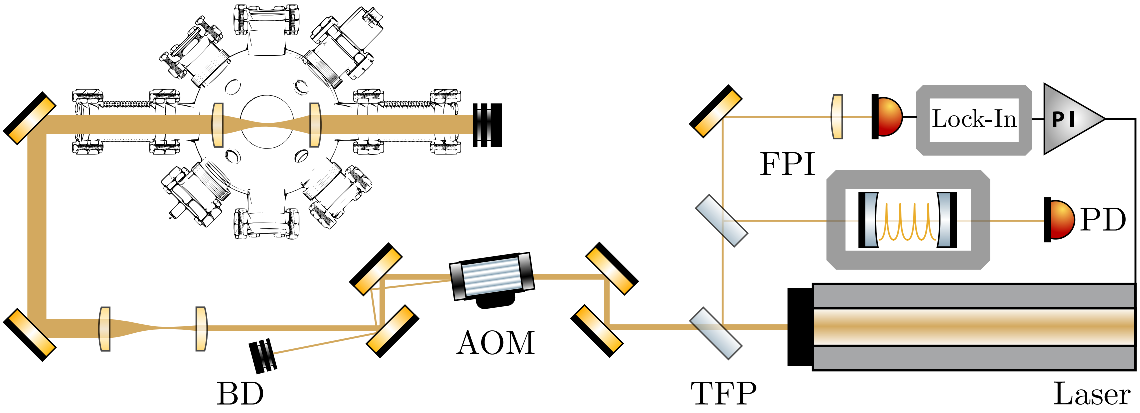

Figure 3.5: Experimental setup of the single focused optical dipole trap, in which, due to the non-standard wavelength of the CO_2 laser (bottom right), almost exclusively ZnSe optics are used. Two partial beams are split of from the main beam using two thin-film polarizers (TFP). One sub-beam is used for resonator stabilization through a lock-in amplifier and PI controller, while the other is directed towards a Fabry-Pérot interferometer (FPI). The main beam passes through an acousto-optic modulator (AOM), where the zeroth order is directed into a beam dump (BD). After the beam is expanded using a telescope, it is guided into the vacuum chamber and then focused onto the atoms using another telescope within the chamber. Outgoing laser light is blocked by another beam dump at the chamber's exit window.

the output signal of the lock-in amplifier. The DC offset voltage of the piezoelectric actuator is controlled by a PI controller. A more in depth description can be found in the Master thesis of S. Z. Hassan [121].
Moving on from the monitoring and stabilization setup, the main beam path is guided through a water cooled acousto-optical modulator (*IntraAction AGM-406B1*). While modulation of RF-signal amplitude varies the beam intensity in the first order, the frequency modulation allows for rapid spatial manipulation in the trapping region. Doing this, effectively expands the area of the trapping potential and improves the loading efficiency from the magneto-optical trap to the dipole trap as can be seen in Figure 3.6.

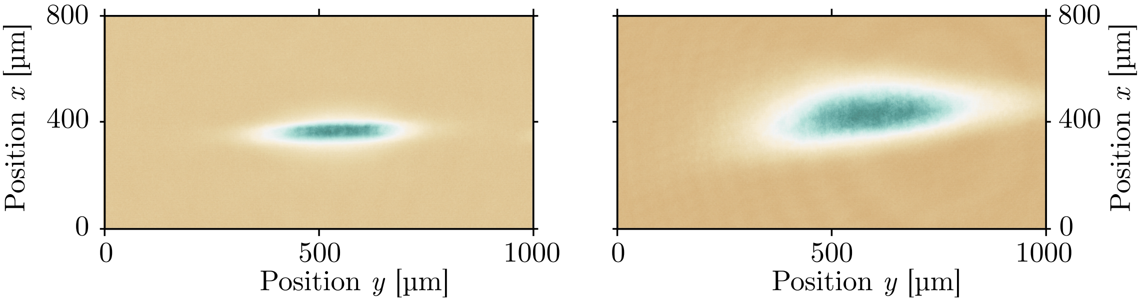

Figure 3.6: Absorption images of pre-cooled atoms loaded into the optical dipole trap with and without spatial modulation of the trapping beam. The modulated trap (right panel) yields a significant increase in loading efficiency.

Here it is crucial to chose a large enough modulation frequency of 50 kHz, such that the effective trapping potential corresponds to the time-averaged modulated potential for the atoms. Previous works can be referred to for a more detailed description of this scheme [122], which typically increases the amount of atoms loaded into the dipole trap by a factor of five. Once the beam passes through the acousto-optical modulator, the zeroth order is directed into a designated beam dump, while the first diffracted order is expanded using a widening telescope. The beam is finally guided into the chamber, where another telescope consisting of two ZnSe lenses focuses the beam to a waist size of $w_0 = 21\,\mu\mathrm{m}$. The trap geometry can be finely adjusted by a mechanical access from the outside, yielding a trap depth of $U_{\mathrm{dip}} = 3.3\,\mathrm{mK}$ for a maximum beam power in the chamber of $P_{\mathrm{CO_2}} = 32\,\mathrm{W}$.

3.4 Optical Lattice Potential

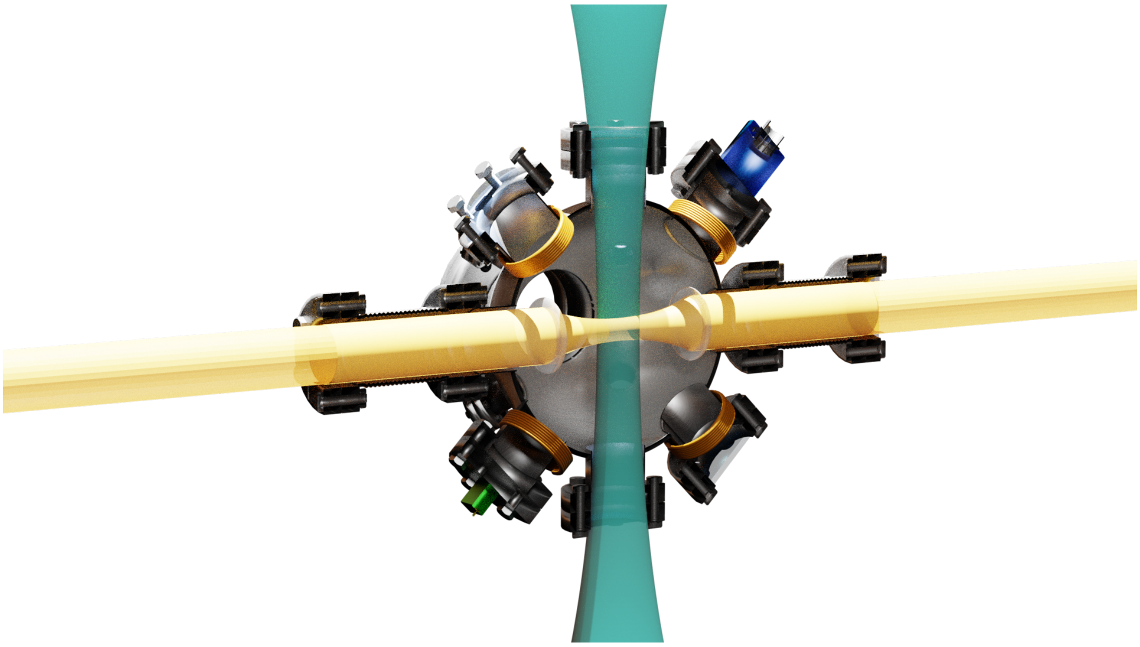

3.4.1 Optical setup

This section discusses the experimental setup for preparing and manipulating the atomic Bose-Einstein condensate and the creation of multi-photon lattices. A one-dimensional optical lattice is generated by a trapezoidal diode laser (*Toptica DLX 110*), which has been already introduced in section 3.2.1. The main laser beam is split into two parts and enters the vacuum chamber from opposite sides (top and bottom).

Figure 3.7 illustrates the experimental setup. After passing through a Faraday isolator, a small portion of the beam is used to monitor frequency characteristics with a Fabry-Pérot interferometer (FPI) and a single mode fiber connected to a wavemeter. As the laser used in the experiment is several nanometer detuned from the resonance frequency of the ^{87}Rb D2-line, with a wavelength of $\lambda_{\mathrm{lat}} = 783.5\,\mathrm{nm}$, the laser diode does not require active stabilization, apart from the standard temperature stabilization provided by the laser

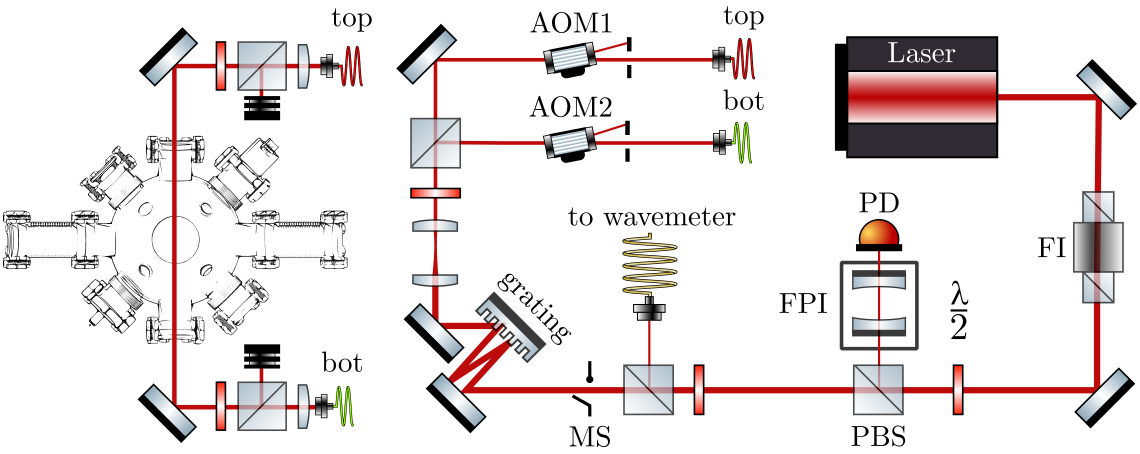

Figure 3.7: Experimental setup of the optics required to generate the lattice potential. After the main beam of the laser (top right) passes through a Faraday isolator (FI), sub-beams are split off to be directed to a Fabry-Pérot interferometer (FPI) and a wavemeter. The main beam passes through a mechanical shutter (MS) and is spectrally filtered using a holographic grating. A telescope optimizes the beam size to match the active aperture of the two acousto-optic modulators. At a polarizing beam splitter (PBS), the main beam is divided into both arms of the optical lattice and coupled into their respective fibers (top, bottom). The fiber outputs are positioned above and below the vacuum chamber and guide the coupled light in opposite directions through the chamber. Lenses at each output focus the laser light at the center of the chamber, while the wave-plates and polarizing beam splitters prevent the counter-propagating laser light from re-entering and direct it into respective beam blockers (BD).

controller. However, spontaneous emission in the edge regions of the trapezoidal diode can cause undesired heating of the atoms. To address this issue, a spectral filtering of the laser beam is carried out using a holographic reflection grating (*Ondax PLR808-92.5-12-17.5-1.5*), which is adjusted at an angle for maximum emission at $783.5\,\mathrm{nm}$ and passed twice by the laser beam. The beam diameter is subsequently reduced using a telescope to fit the active aperture of the following acousto-optical modulators. After the main beam is split into two sub-beams, each of them is guided to an AOM (*Crystal Technology 3200-121*) and fed into polarization-maintaining single-mode fibers. The couplers (*Schäfter & Kirchhoff 60FC-4-M8-10*) of the respective outgoing beams, which are located above and below the vacuum chamber, include micro-lenses (*Schäfter & Kirchhoff 5M-S150-08-S*) that focus the outgoing light to a beam diameter of $170\,\mu\mathrm{m}$ with $50\,\mathrm{mW}$ in each beam path. This allows for high intensity at the location of the atoms to generate the deepest possible lattice potentials. For the generated four-photon lattice potential π-, σ_+-, and σ_--polarization is needed. By using perpendicular polarization of the counter-propagating lattice beams and applying a magnetic offset field that does not point in the direction of the propagation axis, the quantization axis of the atoms can be chosen such that components of σ_+-, σ_-- and π-polarization are present [113, 123].

3.4.2 Radio-frequency Setup

The main interface between experimental control and optical properties of the respective lattice pulses is the modulation of the center frequency of the acousto-optic modulators. To achieve this, an arbitrary waveform generator with high memory depth (*Keysight 33612A*) is used to synthesize the signals used for modulation. In the past, groundwork on Fourier synthesizing of these signals has been completed, such as frequency modulating the upper lattice beam in a way that makes the lattice appear at rest in the atomic reference frame [114]. Using a linear frequency modulation

$$f_{\mathrm{mod}} = f_c - \frac{2g}{\lambda_{\mathrm{lat}}} t \tag{3.1}$$

where f_c denotes the center frequency of the AOM, the gravitational acceleration g and λ_{lat} is the lasers wavelength, preparatory measurements performed to characterize the optical lattice potential on falling atoms will be presented in the next chapter. Other applications in the experiment can be employed by the same laser beam, to address different classes of atoms or to generate moving lattices.

The pulses used to manipulate atoms are modulated onto the laser beam coming from the bottom of the chamber, while the top beam only undergoes frequency ramps. The signals are synthesized at a center frequency of $47\,\mathrm{MHz}$ and then shifted to the required frequency using a double-balanced mixer and an oscillator signal of $154\,\mathrm{MHz}$. The resulting modulated radio frequency signals are filtered, switched, and amplified before reaching the acousto-optic modulators. The RF switch allows for jitter reduction in situations where RF signals need to be combined with other control signals of the real-time system. For a more detailed description of the parts and models in this setup including an experimental scheme of the radio-frequency setup, the reader is kindly referred to the previous works conducted on the experiment [53, 113, 114].

3.5 Absorption Imaging

To image the atomic BEC after each experimental cycle, a resonant sub-beam of the cooling laser is employed (see subsection 3.2.1). However, since the atoms reside in the low-energy state $|5S_{1/2}, F = 1\rangle$ after the dark MOT phase, they are transparent to the cooling laser transition. Therefore, two methods , which are presented in the following, are utilized in the experimental setup to transfer the atoms back to the $|5S_{1/2}, F = 2\rangle$ state, which can be readdressed by the cooling laser transition.

The commonly used method which is employed in most measurements consists of a short light pulse ($\tau_{\mathrm{R}} = 300\,\mu\mathrm{s}$) of the repumping laser to transfer the atoms back to the desired state. To investigate the periodic quantum Rabi model, measurements with up to a few millisecond-long evolution times are required, for which only a small number of a few hundred atoms is utilized, minimizing undesired interatomic collisions (further investigated in following sections). However, obtaining clear images of such small ensembles using the repumping light is challenging due to increased noise caused by off-resonant scattering during the re-transfer process. Therefore, to obtain clearer real space images of small numbers of atoms, a different method is employed, where a short microwave pulse

($\tau_{\mathrm{MW}} = 100\,\mu\mathrm{s}$) is utilized, taking advantage of the hyperfine splitting of the $|5S_{1/2}\rangle$ state. A significant improvement in imaging performance, especially for spatial imaging, was made in the context of the dissertation work of J. Koch [53]. Limited by the distance of the atoms to the central optical access and the size of the used window, the improvement in imaging performance involved the installation of a doublet lens with a diameter of $d \approx 50.8\,\mathrm{mm}$ (*Thorlabs AC508-080-B*) and a new calibration of the distance to the camera of approximately $86.7\,\mathrm{mm}$ to avoid limiting the pixel size of the sCMOS camera (*Andor Zyla 5.5 sCMOS*).

3.6 Experimental Cycle

This section provides an overview of the experimental procedure. In general, the entire cycle can be divided into three areas: the generation of a Bose-Einstein condensate, the quantum simulation of the periodic quantum Rabi model (pQRM), and the subsequent detection of atomic trajectories in position or momentum space. The entire process is controlled by a real-time control system (*Jäger Computergesteuerte Messtechnik GmbH ADwin-Pro I*), which serves as an interface between in-house developed control software and experimental hardware. The communication between the software and the real-time control unit is programmed using VISA interfaces and can address the devices present in the experiment using both digital TTL signals and analog output channels with a voltage range of $-10\,\mathrm{V}$ to $10\,\mathrm{V}$ and a time resolution of $4\,\mu\mathrm{s}$. The following subsections provide an overview of the different stages comprising the entire experimental cycle.

3.6.1 Creation of a Spin Polarized Bose-Einstein Condensate

The basic principle of generating a rubidium Bose-Einstein condensate involves cooling a large ensemble of pre-cooled atoms in an optical dipole trap through evaporative cooling. To accomplish this, a current of approximately $4\,\mathrm{A}$ is applied onto the dispensers, which allows rubidium vapor to enter the chamber. By employing optical cooling, where the detuning of the cooling laser is approximately three linewidths, and magnetic trapping, where the coils are flowed with a current of $80\,\mathrm{A}$, a magneto-optical trap containing approximately $1 \cdot 10^9$ atoms can be created. Loading a magneto-optical trap (MOT) directly from the background gas simplifies the experimental setup by eliminating the need for a combination of a MOT and a Zeeman slower. However, the total cycle time in this experiment increases because a minimum time of approximately $25\,\mathrm{s}$ must be maintained to fully load the MOT.

The optical dipole trap is activated two seconds before the end of the MOT phase, collecting pre-cooled atoms at its focus. During this process, the full power of approximately $30\,\mathrm{W}$ is irradiated into the chamber, while the RF signal of the AOM is modulated with a frequency of $50\,\mathrm{kHz}$, causing spatial expansion of the trapping region. Simultaneously with this phase, a $120\,\mathrm{ms}$ long dark MOT phase takes place, where the cooling laser frequency is detuned by approximately $150\,\mathrm{MHz}$ relative to the cooling transition. This compensates for the AC Stark shift caused by the dipole force and reduces the overall photon scattering rate, enhancing the loading efficiency into the dipole trap as it further decreases the ensemble temperature. After turning off the cooling and repumping laser light, only atoms remaining in the optical dipole trap are left.

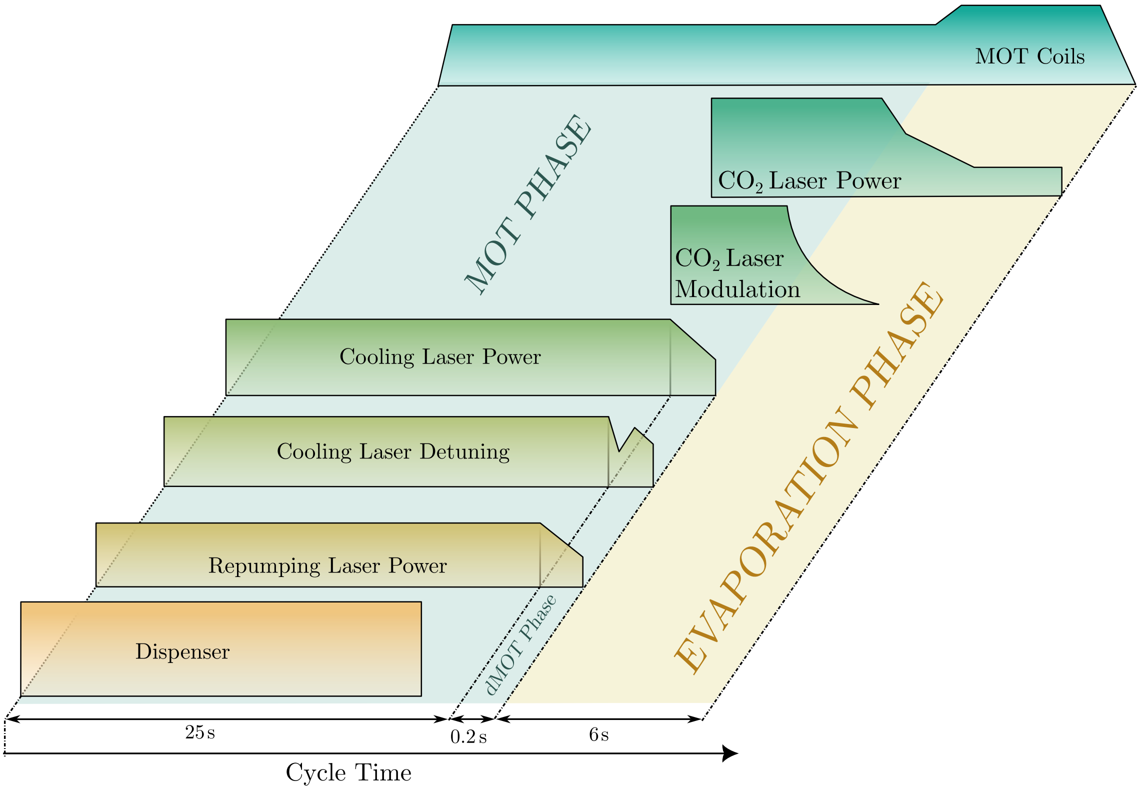

Figure 3.8: Illustration of the experimental cycle for the creation of the atomic Bose-Einstein condensate. The light green area represents the phase of magneto-optical trapping the atoms (MOT phase) with the subsequent evaporation phase depicted in light yellow. The relatively short dark MOT phase of $200\,\mathrm{ms}$ is highlighted within dashed lines.

As in the subsequent step of forced evaporative cooling, the majority of the excessively high energetic atoms are released from the optical dipole trap, since a high number of trapped atoms [124] at the start of the process is crucial. In the experiment, approximately $5 \cdot 10^6$ atoms prove to be more than sufficient for further evaporation with a starting trap depth of $U_{\mathrm{dip}} = 3.3\,\mathrm{mK}$. The entire evaporation process consists of three linear ramps that use the RF power of the AOM to regulate the light intensity and, thus, the trapping depth of the dipole trap. During the first ramp, $96\,\%$ of the RF power is reduced within a short time of $0.5\,\mathrm{s}$, causing the highest energetic atoms to leave the trap. Subsequently, a much slower evaporation ramp takes place to further decrease the trapping potential and, thereby, achieve a Bose-Einstein condensate. Afterwards, the final power is maintained at approximately $1\,‰$ of the initial power to allow for a steady state to be established. The entire process takes approximately 6 seconds, during which the spatial expansion of the dipole trapping beam is adiabatically ramped down to minimize mechanical heating of the produced Bose-Einstein condensate.

In order to simulate the quantum Rabi model, Raman transitions are utilized to create an optical lattice. Additionally, the ability to levitate atoms against gravity necessitates the presence of spin polarization in the generated Bose-Einstein condensate (BEC). For these two reasons, a magnetic field is applied to selectively facilitate evaporation into a specific Zeeman level ($m_F = -1$). The presence of the spin-polarized BEC is confirmed through techniques such as microwave imaging and the combination of a Stern-Gerlach field with time-of-flight far field imaging. The preceding procedures lead to the production of a spin-polarized BEC comprising approximately 40 000 atoms. However, it is discovered in the subsequent results chapter that high atom numbers in long temporal evolution measurements give rise to undesired heating effects due to atom-atom interaction. To address this issue, the atom number is limited to below 1000 by employing evaporation in even shallower traps. Notably, the current experiment features the unique simulation of the bosonic mode of the quantum Rabi model using an optical dipole trap, which, to the best of our knowledge, is only possible with such a far-off resonance trap realized with the CO_2 laser in our setup. Following the utilization of the optical dipole trap for BEC generation, the final power can be adiabatically increased to simulate the bosonic mode of the quantum Rabi model, which is also directly linked to the coupling strength g (as can be seen in equation (2.17)). A lower threshold of $\omega_{\mathrm{min}}/2\pi \gtrsim 250\,\mathrm{Hz}$ for the increased power emerges naturally to ensure the trap's depth is sufficient for harmonic oscillation, while an upper threshold of $\omega_{\mathrm{max}}/2\pi \lesssim 750\,\mathrm{Hz}$ is set to prevent undesired heating processes from destroying the atomic BEC.

3.6.2 Quantum Simulation of the pQRM

The here performed quantum simulation of the periodic Quantum Rabi Model (pQRM) consists of a preparation-, time evolution-, and an analysis phase. As will be seen later, the results presented here are divided into quantum states prepared in the eigenbasis of $\hat{\sigma}_x$- and $\hat{\sigma}_z$- operators. For $\hat{\sigma}_x$, atomic wave packets are prepared using a single Bragg pulse to imprint a momentum transfer of $\pm 2\hbar k$ at the band gap of the four-photon lattice's dispersion relation. On the other hand, the preparation in the eigenbasis of $\hat{\sigma}_z$ is realized by employing two counter-propagating Bragg pulses, which create a 50:50 superposition state of the $+2\hbar k$ and $-2\hbar k$ momentum picture states. Here, the relative phase between the wave packets gives insight into the quantum state being in the upper- ($|\uparrow\rangle$) or lower eigenstate ($|\downarrow\rangle$) of $\hat{\sigma}_z$. The preparation process takes place in the optical dipole trap and needs to be completed as quickly as possible to avoid interfering with the Rabi dynamics evolving in the trap. A suitable compromise is achieved with preparation times of approximately $\tau_{\mathrm{prep}} \approx 40\,\mu\mathrm{s}$, which is sufficiently long to ensure good frequency resolution.

To carry out the time evolution measurements of the quantum simulation described in the previous chapter 2, the quasi-harmonic potential of the dipole trap and the periodic potential of the four-photon lattice need to be combined both temporally and spatially. After preparing the system and setting the optical dipole trap to the appropriate trapping frequency, the lattice potential of suitable intensity is also applied. The atoms are then exposed to the combined potentials, allowing the observed dynamics to be detected gradually over time. This exposure duration corresponds to the duration of the time evolution of the pQRM Hamiltonian. By subjecting the system to different lengths of exposure to these potentials before analysis and detection, it becomes possible to measure the temporal evolution of various observables.

Following each experimental cycle for determining the time evolution, an analysis phase

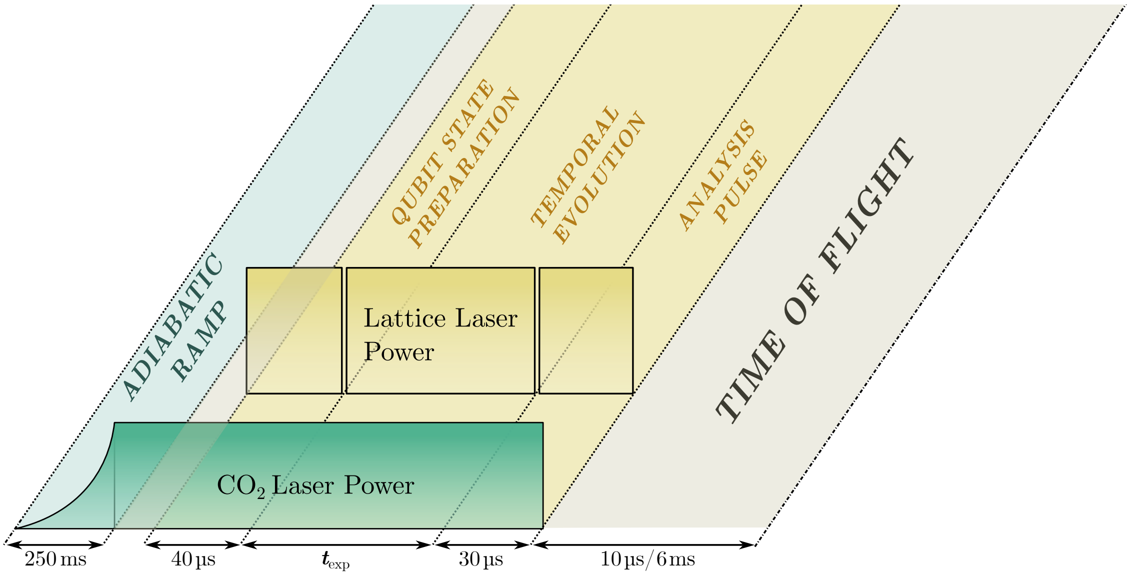

Figure 3.9: Illustration of the experimental cycle for the simulation of the periodic quantum Rabi model. After the creation of an atomic BEC, the CO_2 laser power is adiabatically ramped until a steady state potential for the atoms is reached at the desired trapping frequency. Subsequent qubit state preparation with the lattice laser is performed followed up by a variable experimental time t_{exp} and an analysis pulse. Depending on observation in real- or momentum space, the time of flight duration is chosen between $10\,\mathrm{\mu s}$ and $8\,\mathrm{ms}$.

is conducted where the analysis method is adjusted based on the prepared initial state and the desired observation in either position- or momentum space. In the case of the simplest preparation in the eigenstate of $\hat{\sigma}_x$, the analysis involves straightforwardly turning off all optical potentials and performing detection either in position space, $10\,\mathrm{\mu s}$ after turning off the potentials, or in momentum space after a time-of-flight duration of $8\,\mathrm{ms}$. To analyze quantum states prepared in the $\hat{\sigma}_z$ basis, a phase-selective measurement method is required, as the relevant information is encoded in the relative phase between the two wave packets. Simply turning off the optical potentials would lead to undesired relaxation into individual bare states, which are eigenstates of $\hat{\sigma}_x$. Therefore, an interferometric $\pi/2$ pulse is applied during the measurement of $\hat{\sigma}_z$ eigenstates, which maps the current quantum state back, depending on the relative phase between the wave packets, enabling a phase sensitive readout analysis. Again, as for the preparation pulse, the chosen pulse duration is short enough to avoid interference with the pQRM dynamics ($\tau_{\mathrm{read}} = 30\,\mathrm{\mu s}$), while still providing sufficient frequency resolution.

3.6.3 Detection

To observe the temporal evolution of the atomic BEC, absorption imaging is employed at the end of the experimental cycle using a cooling laser and an sCMOS camera. As mentioned before, a distinction is made between capturing images in position space and momentum space. In position space imaging, a microwave pulse is used to repump the atoms to the $|5S_{1/2}, F = 2\rangle$ state, while a repumping laser pulse is utilized for momentum

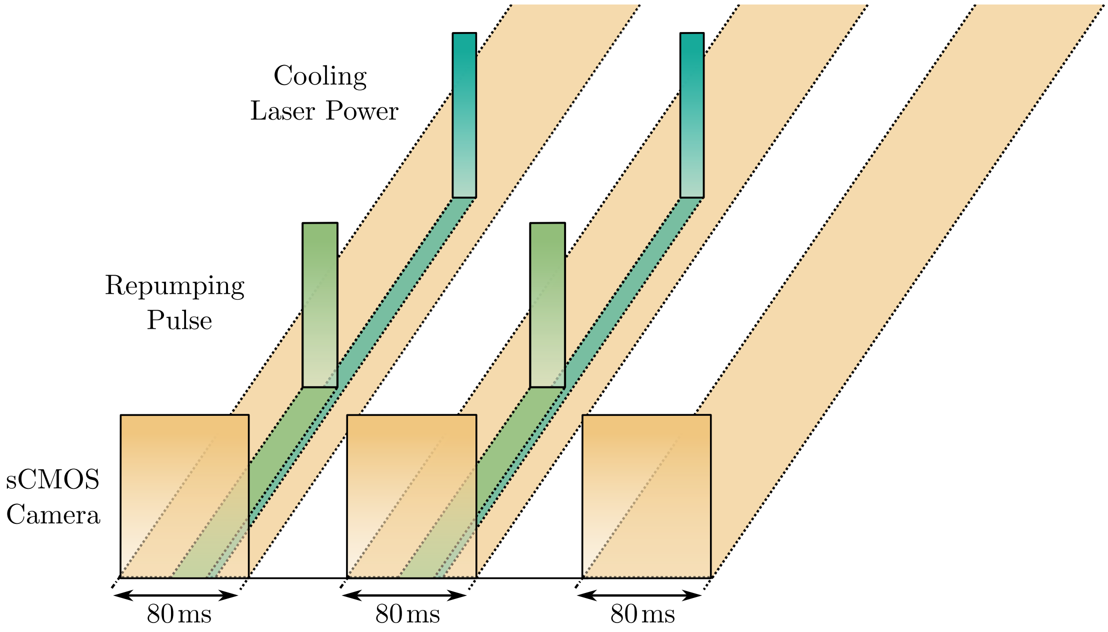

Figure 3.10: Illustration of the experimental cycle describing the absorption imaging protocol. The sCMOS camera is triggered three times, where during the first two pictures a foregoing repumping pulse is used to reveal the atomic ensemble for the cooling laser transition. The last picture is used for background correction.

space imaging. Three images separated by 80 ms are subsequently captured.
The first image creates a shadow of the atoms on the camera chip by absorbing resonant photons from the cooling laser. This process induces heating and destroys the quantum system. As a result, the second cooling laser pulse is not absorbed by atoms, and the image on the camera chip includes all the laser light. By subtracting the two images, the absorption of the atomic ensemble is revealed. The third and final image is taken with no laser light present, serving as a reference for background correction.

CHAPTER 4

Experimental Results

The following chapter presents the observed results for various experimental parameters. Firstly, a characterization of the achievable optical lattice- and trap frequencies will be provided as monitoring measurements, which serve as an experimental tool.
In the context of the periodic quantum Rabi model, various observables in two different states of preparation will be presented. Beginning with measurements in the qubit superposition state (in the $\hat{\sigma}_x$-basis), the temporal evolution of expectation values for position $\langle x \rangle$, mean quasimomentum $\langle q \rangle$, mean band occupation $\langle \sigma_x \rangle$, and the bosonic excitation number $\langle N \rangle$ will be showcased.
When considering the initial state prepared in a qubit eigenstate (in the $\hat{\sigma}_z$-basis), it enables the observation of collapse and revival characteristics by incorporating a phase-sensitive analysis scheme. Concluding the results chapter, measurements of the temporal evolution of the bosonic excitation number will be discussed, this time with the system prepared in the qubit eigenstate. An intriguing difference is revealed between the chosen state of preparation, particularly for large qubit frequencies.

4.1 Experimental Characteristics and Preparatory Measurements

4.1.1 Optical Lattice Potential

To create a periodic potential in the experimental setup, the qubit frequency ω_q can be determined by measuring the Rabi oscillations of atoms in a four-photon lattice potential. The process starts by preparing the atoms in the $-2\hbar k$ momentum state using a Bragg π-pulse. Next, the four-photon lattice potential is applied, allowing transitions between the momentum states $-2\hbar k$ and $+2\hbar k$.
The temporal evolution of this prepared state is shown in Figure 4.1(a), which depicts the relative population of atoms in the momentum states $\pm 2\hbar k$ and $0\hbar k$. The presence of a two-photon lattice is indicated by the here visible oscillation between the zeroth and second orders, and can be suppressed by increasing the two-photon detuning δ. This is particularly important for long-time interaction, which is the main objective of this thesis, as collisions with residual atoms in the zeroth order increase undesired heating in the system. Figure 4.1(b) displays the expected behavior for higher detuning values δ, leading to a rapid decrease in the number of atoms in the $0\hbar k$ momentum state, implying fewer two-photon processes, as seen on the right vertical axis. However, this comes at the expense of reducing the optical four-photon lattice potential depth, as can be seen in equation (1.54), and hence the maximum Rabi frequency (as indicated on the left vertical

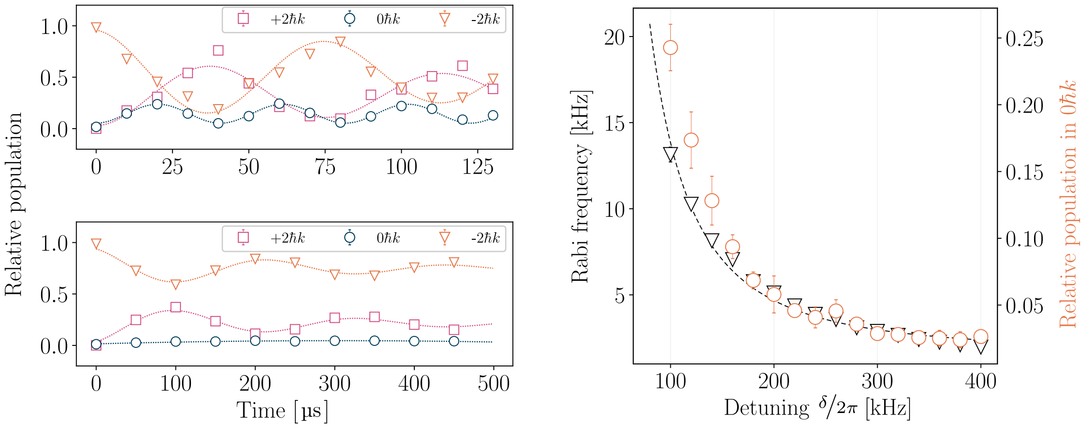

(a) **(b)**

Figure 4.1: (a) Occupation of atoms in the $-2\hbar k$- (orange triangles), $0\hbar k$- (blue circles) and $+2\hbar k$-momentum states (pink squares) versus time, indicating the observation of Rabi oscillations. Atoms are initially prepared in $-2\hbar k$ momentum state and subsequently observed in momentum space during a time of flight measurement. The upper and lower panel show the temporal evolution of all momentum states occupation number with the two-photon detuning of $\delta/2\pi = 100\,\text{kHz}$ and $\delta/2\pi = 210\,\text{kHz}$, respectively. It is clearly visible that for the lower detuning value, undesired occupation in the $0\hbar k$ momentum state is observed. (b) The measured Rabi frequency $\omega_\text{q}/2\pi$ (black triangles) for different detuning values $\delta/2\pi$ can be described by a hyperbolic function (dashed black line). To optimize clean oscillation between $+2\hbar k$ and $-2\hbar k$ the atoms population in $0\hbar k$ is also measured (orange circles).

axis). In practice, a good compromise is achieved with $\delta/2\pi = 210\,\text{kHz}$, resulting in a maximum oscillation frequency of approximately $\omega_\text{q}/2\pi \simeq 5\,\text{kHz}$ and sufficient suppression of undesired two-photon processes.

Continuing with the characterization, the dependence of the Rabi frequency on the RF-power is investigated to reveal the full range of the tunable qubit frequency ω_q. To perform this, atoms are prepared at a momentum state of $-2\hbar k$, and their oscillation is observed after turning off the optical dipole trap so that they are solely superimposed to the optical lattice potential.

Since the atoms are accelerated by gravity relative to the potential created by the lattice laser beams, the laser beam from below is detuned using the AOM according to equation (3.1), which takes into account the acceleration due to gravity $g = 9.81\,\text{m/s}^2$, and the wavelength of the lattice laser beam $\lambda_\text{lat} = 783.5\,\text{nm}$.

An exemplary measurement for the case of an RF-power of $0\,\text{dBm}$ (blue) is depicted in Figure 4.2(a). The fitting curve is a damped harmonic oscillation and implies that for lower power values of $-14\,\text{dBm}$ (orange) longer evolution times are needed to extract the Rabi frequency out of a full oscillation period. Here, an experimental limit arises where, with longer pulses, the amount of addressable atoms decreases due to finite velocity distribution, as shown in Figure 4.2(a). In other words, not all atoms participate to the oscillation, ultimately reducing the observed amplitude. To characterize the full RF-power range, an indirect measurement is implemented by measuring the optical power of each

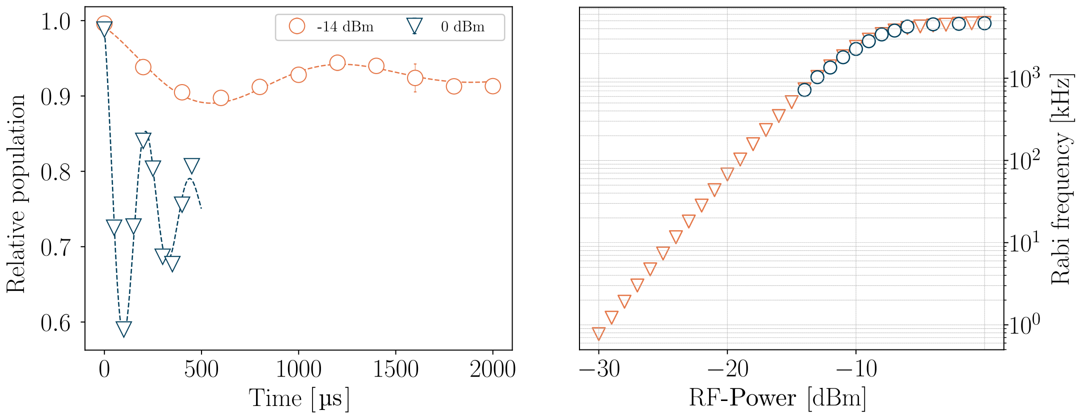

(a) **(b)**

Figure 4.2: (a) Exemplary measurement of the relative population of atoms in the $-2\hbar k$ momentum state, resulting in the Rabi frequency for a RF-power of $0\,\mathrm{dBm}$ (blue triangles) and $-14\,\mathrm{dBm}$ (orange circles), where for the ladder, a longer measurement time is needed in order to observe a full oscillation period, resulting in an experimental limitation for low RF-power values. (b) Rabi Frequency of the four-photon lattice against RF-power used to address the AOM. The direct measurement of atoms oscillating in the lattice potential (blue circles) is only possible for larger power values, due to damped oscillation. Using a fast photodiode to measure the optical power of each lattice beam, covers the experimentally non accessible region of the frequency range (orange triangles).

lattice beam with a fast photo-diode (*Thorlabs DET10A*). Short pulses of $500\,\mu\mathrm{s}$ are chosen to minimize thermal drifts of the AOM. By using nonlinear regression analysis and combining both measurements, it is possible to cover the full RF-power range using the following equation for the obtained photo-diode signals $U_{\mathrm{PD},1}$, and $U_{\mathrm{PD},2}$, where a and b are fitting parameters:

$$\omega_\mathrm{q}(P_\mathrm{RF}) = (a \cdot U_{\mathrm{PD},1} + b \cdot U_{\mathrm{PD},2}) \tag{4.1}$$

Figure 4.2(b) shows the obtained Rabi frequency $\omega_\mathrm{q}/2\pi$ by directly measuring atomic oscillations depicted in Figure 4.2(a) (blue circles) and indirect measurement of the optical power using equation (4.1)(orange triangles). The datasets show good compatibility in the overlapping region, reaffirming the used procedure and revealing the full tunable qubit frequency range for the experiment.

4.1.2 Harmonic Trapping Potential

Moving on, the harmonic trapping potential will be characterized to determine the attainable trapping frequencies needed to simulate the bosonic mode ω of the periodic quantum Rabi model. A Gaussian trapping potential is provided for the pre-cooled atoms by a single focused $\mathrm{CO_2}$ laser beam. The deviation from a harmonic potential is negligible, at only $0.22\,\%$, as calculated by comparing the recoil energy of the atoms induced by the lattice pulses $E_{\mathrm{Rb,max}} = 2E_\mathrm{R}$ with the energy of the dipole trapping potential $U_\mathrm{dip} = 31E_\mathrm{R}$ [53]. Direct measurement of the trap frequency ω involves the application of a Bragg π-pulse

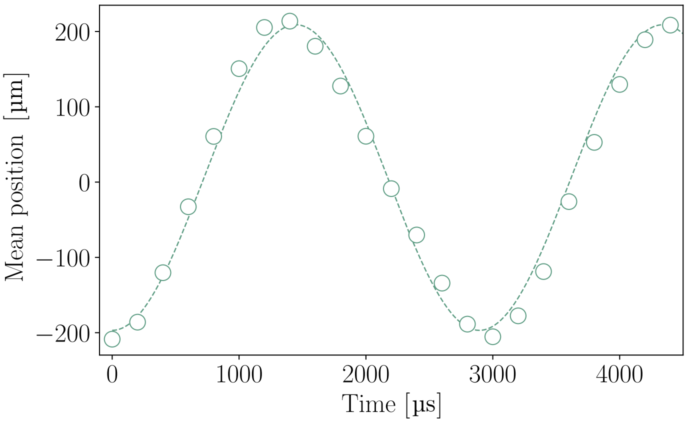

Figure 4.3: The observed variation of mean position of initially prepared atoms in the $-2\hbar k$ momentum state versus time shows the expected oscillatory behavior in the optical dipole trapping potential. Using nonlinear regression to fit a harmonic oscillation (green dashed line) onto the experimental data (green circles) shows good agreement and a resulting harmonic frequency of $^{\omega}/_{2\pi} = 343(2)\,\mathrm{Hz}$.

to transfer the atoms in the $-2\hbar k$ state, followed by the observation of atomic oscillation in the harmonic trapping potential using far field time of flight images. An exemplary measurement for an oscillation frequency of $^{\omega}/_{2\pi} = 383(2)$ Hz is shown in Figure 4.3, where nonlinear regression analysis is used to calculate the mean position of the atomic cloud, shown as green circles. The experimental data is well described by a harmonic oscillation curve, providing further evidence for the harmonic nature of the trapping potential.

In order to change the trap frequency experimentally, the control parameter p, which regulates the RF-power for the used AOM, is varied. Figure 4.4(a) displays the measured trap frequencies for different values of p. The obtained data, shown as green circles, follows the expected theoretical solid line, revealing the experimental parameter range for tuning the optical dipole trap frequency $^{\omega}/_{2\pi}$. As shown by equation 2.17, $g(\omega)$ is inherently dependent on ω, therefore, the measured trap frequencies in Figure 4.4(a) can be utilized to calculate the resulting relative coupling strength, revealing an experimental limitation for $^{g}/_{\omega}$ when the maximum trap frequency is reached.

The two limiting ranges for achievable trapping frequencies are, on one hand, constrained from below by the need for a sufficiently deep trap to retain the atoms in a harmonic trap, and on the other hand, limited from above by strong atom-atom interactions and three-body losses when the trapping potential is too deep. Figure 4.4(b) illustrates this behavior, where the maximum trap frequency $^{\omega}/_{2\pi} = 769(4)\,\mathrm{Hz}$ is marked as a vertical dashed line. It is evident that due to restrictions in the trapping frequency range, the experiment presented here solely operates far in the perturbative deep strong coupling regime ($^{g}/_{\omega} \gg 1$).

4.1.3 Coherence Characteristics

In order to investigate the long time interaction dynamics in the periodic quantum Rabi model, it is crucial to ensure the long time quantum coherence of the entire system. There-

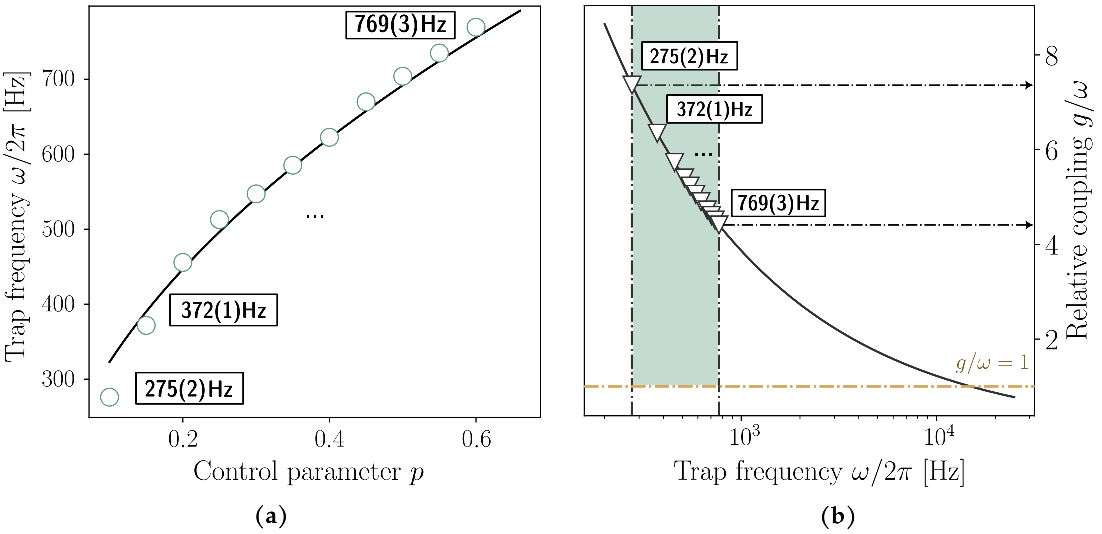

(a) (b)

Figure 4.4: (a) Experimental variation of the control parameter p and resulting trap frequency $^{\omega}/_{2\pi}$ (green circles). The solid line corresponds to theoretical calculation including multiple experimental parameters such as optical laser power $P_{\mathrm{CO}_2} = 32\,\mathrm{W}$, beam waist $w = 21\,\mu\mathrm{m}$ and wave length of the CO_2 laser beam $\lambda_{\mathrm{CO}_2} = 10.6\,\mu\mathrm{m}$. (b) Using the obtained data in Figure 4.4(a) to calculate the relative coupling strength $^{g(\omega)}/_{\omega}$ from equation (2.17). With increasing trap frequency, the relative coupling strength decreases, resulting in an experimental limit for the achieved coupling strength and restricting the experiment far in the deep strong coupling regime (highlighted in green). The horizontal arrows indicate an estimate for the achievable coupling strengths in the experiment, while the relative coupling strength of $^{g}/_{\omega} = 1$, which indicates the emergence of the DSC regime, is marked as a yellow horizontal line.

fore, several preparatory measurements were conducted and are presented in this section. Using a Ramsey-Bordé interferometer first the coherence time of the atomic BEC will be discussed. This scheme will be expanded by combining the atomic dynamics in the harmonic trap with the lattice beams to perform the interferometric pulses, giving insights on the effect of atom number and coherence time in the system.

Coherence of the Atomic BEC

In Section 4.1.2, it was shown that the harmonic trap frequency ω can be adjusted within a range of $^{\omega}/_{2\pi} = 275(2)\,\mathrm{Hz}$ to $^{\omega}/_{2\pi} = 769(2)\,\mathrm{Hz}$, resulting in minimum required coherence times of a few milliseconds. To assess this solely for the atomic Bose-Einstein condensate, a Ramsey-Bordé interferometer is utilized, whose scheme is shown in Figure 4.5(a). For this, a Bragg $\pi/2$-pulse prepares the atomic momentum state $\Psi_{\mathrm{ini}} = \frac{1}{\sqrt{2}}(|0\hbar k\rangle + |2\hbar k\rangle)$, which is a superposition state between the $0\hbar k$ and $+2\hbar k$ momentum state, followed up by a separation time of $\tau = T/2$ and a subsequent application of a Bragg π-pulse, after which another separation time of τ is implemented along with an additional $\pi/2$-pulse. Varying the imprinted relative phase between the two Bragg beams during preparation, a phase dependent transfer between the momentum states is expected, attributed to preserved coherence. Figure 4.5(b) displays the resulting data, where the relative population in the

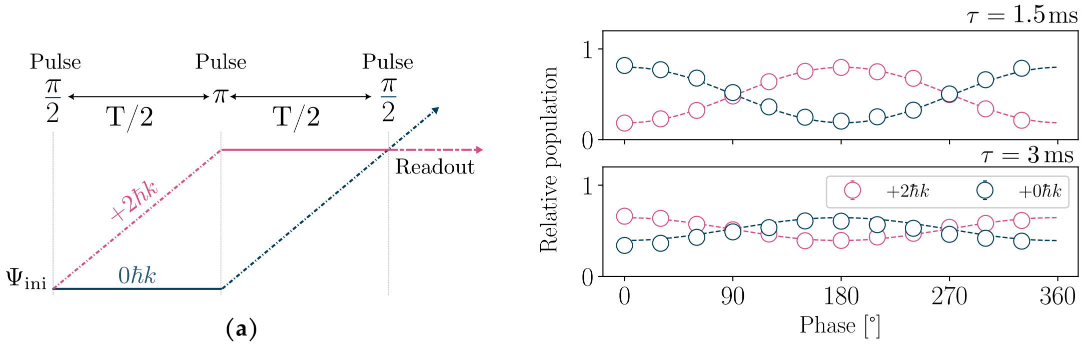

(a)

(b)

Figure 4.5: (a) Ramsey-Bordé interferometer for the free falling atomic BEC after evaporation. After an initial Bragg $\pi/2$-pulse and a subsequent separation time of $\tau = T/2$ a Bragg π-pulse is applied. An additional separation duration and another $\pi/2$-pulse allows for readout and detection of the phase. (b) Measurement of the relative population in the $0\hbar k$ and $+2\hbar k$ momentum state depending on the imprinted phase at preparation for different separation times $\tau = 1.5\,\mathrm{ms}$ and $\tau = 3\,\mathrm{ms}$.

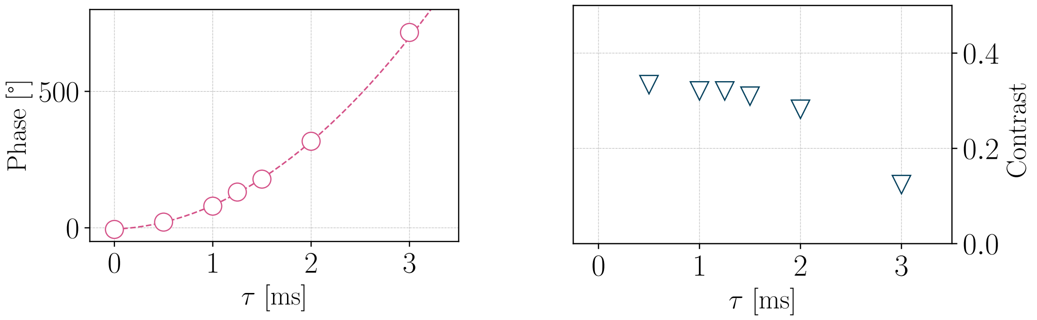

(a)

(b)

Figure 4.6: (a) Measuring the phaseshift that occurs when the separation time τ is increased, by fitting a harmonic function onto the data shown in Figure 4.5(b) and calculating the difference in phase for increasing time τ. (b) The observed decrease in contrast for longer separation times, which is extracted from the amplitude of the fitted data. Even for the highest values of τ, which corresponds to a combined coherence time $2\tau = 6\,\mathrm{ms}$, the contrast does not drop to zero, demonstrating phase coherence of the atoms.

two momentum states $0\hbar k$ and $+2\hbar k$ demonstrates a clear dependence on the imprinted phase for a separation time of $\tau = 1.5\,\mathrm{ms}$ (upper panel). Even further increase to a maximum separation duration of $\tau = 3\,\mathrm{ms}$ (lower panel), a non-vanishing contrast is observed, confirming the expected long-term coherence of an atomic BEC. Fitting the data with harmonic oscillation functions, allows the extraction of amplitude and phase information for each separation time, resulting in the demonstrated behavior presented in Figure 4.6(a) and 4.6(b). Here, the occurring phase-shift and decrease in contrast for increasing separation time τ are observed. As expected, the coherence time of the atomic BEC exceeds the required time of evolution and should not be a limiting factor during the quantum simulation experiment.

Combined Coherence of Atoms in the Superimposed Potential

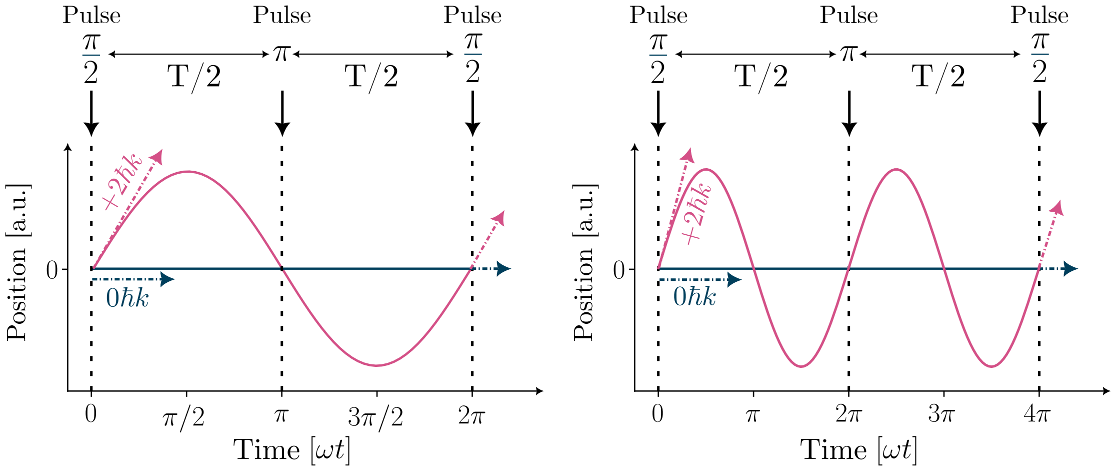

(a) 2π-interferometer **(b)** 4π-interferometer

Figure 4.7: Experimental scheme for analyzing the coherence time in the system using a generalized version of a Ramsey-Bordé interferometer. (a) In order to analyze the combined system of atoms and optical dipole trap, the used $\pi/2$- and π-pulse have to be timed accordingly to the traps oscillation period. Atoms with an initial momentum transfer of $+2\hbar k$ are oscillating in the trapping potential, while atoms with $0\hbar k$ momentum remain at the center of the trap. Due to lack of phase control at $\omega t = \pi$, it is only possible to measure absolute values with no phase relation. This scheme is hence used to observe the relation between contrast and atom number. (b) Doubling the evolution time enables relative phase control at $\omega t = 2\pi$, hence making it possible to observe phase detection between atomic wavepackets.

Moving forward, the coherence of the system is demonstrated in a combined configuration of atoms and the harmonic trap. Essentially, the same interferometer scheme presented in the previous section is employed, but with the difference that atoms now oscillate in the optical dipole trap. This 2π-*interferometer* scheme is shown in Figure 4.7(a), where the Bragg $\pi/2$- and π-pulses occur at the start ($\omega t = 0$), middle ($\omega t = \pi$), and end ($\omega t = 2\pi$) of the oscillation period (orange line), where ω represents the oscillation frequency of the optical dipole trap. As before, the relative population of atoms in the momentum states $0\hbar k$ and $+2\hbar k$ is measured by varying the imprinted phase during the first pulse and the optical dipole trap frequency is set to $\omega/2\pi \simeq 500\,\mathrm{Hz}$.

Figure 4.8 (bottom panels), shows the results of this approach, characterized by randomness of the data. Here, phase fluctuations arising from mechanical vibrations of the lattice beams relative to the dipole trapping beam impede the experimental access to periods of half of the oscillation time at $\omega t = \pi$. Nevertheless using this scheme to investigate the effect of atom numbers on the absolute value of the reached population difference gives insight on the effect of atom-atom interaction in the system. The bottom panel of Figure 4.8 displays three data sets in which the atom number was increased from left to right. In the upper panel, the same data is shown in radial plots for a more visual representation. For a relatively large atom number of $\simeq 7000$ atoms, the absolute value of the relative population drops significantly compared to the case of $\simeq 1000$ atoms, as attributed to more heating and a higher likelihood of three-body losses. Although, varying the imprinted phase for the 2π-interferometer fails to perform the desired correlation with the readout pulse, there is still merit in examining the effect of atom number on the absolute contrast in relative population. As a takeaway, an atom number of 1000 should not be exceeded during long temporal evolution.

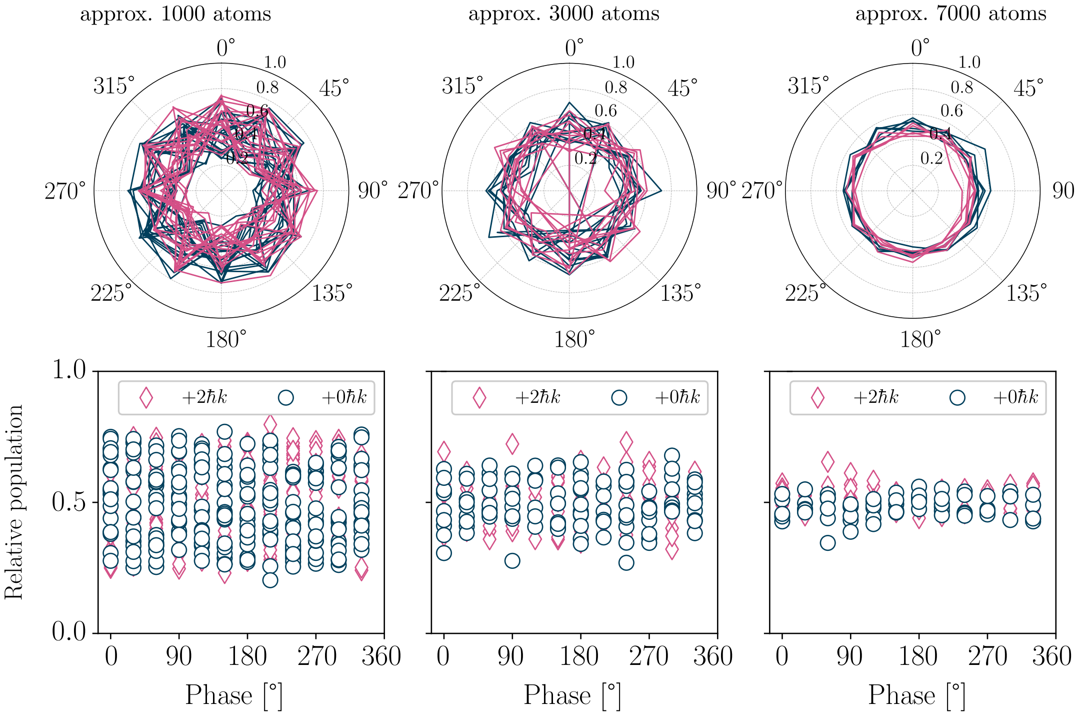

Figure 4.8: Results of the applied scheme in Figure 4.7(a) where a generalized version of a Ramsey-Bordé interferometer is used to analyze the phase dependency on an initially prepared momentum state in $\Psi_{\text{ini}} = \frac{1}{\sqrt{2}}(|0\hbar k\rangle + |2\hbar k\rangle)$. Bottom panels depict the relative population of $0\hbar k$ and $2\hbar k$ and show no visible fringe signal, as attributed to lack of absolute phase control. However, looking at the maximum values, it is still possible to extract information that for increasing atom numbers the observed contrast is strongly damped. The same data is also presented in the above shown radial diagrams in a more visual representation. At each phase value 20 data points were taken.

Expanding the 2π-*interferometer* to a 4π-*interferometer* scheme allows for the Bragg π-pulse to be applied at $\omega t = 2\pi$ and the readout pulse at $\omega t = 4\pi$. With this approach, the relative phase becomes relevant for the readout process, which, in turn, is experimentally accessible. Figure 4.7(b) displays the scheme used for this experimental implementation. The bottom panels of Figure 4.9 exhibit four plots, from left to right, where the time between the Bragg $\pi/2$-pulses is increased from $\tau = 1\,\text{ms}$ up to $\tau = 2\,\text{ms}$ leading to a total observed coherence time of $4\,\text{ms}$ (right panel). This scheme is constrained by the oscillation frequencies reachable in the optical dipole trap. While the left panel corresponds to a maximum trap oscillation frequency of ${}^{\omega}/_{2\pi} = 1002(12)\,\text{Hz}$, the right panel where the

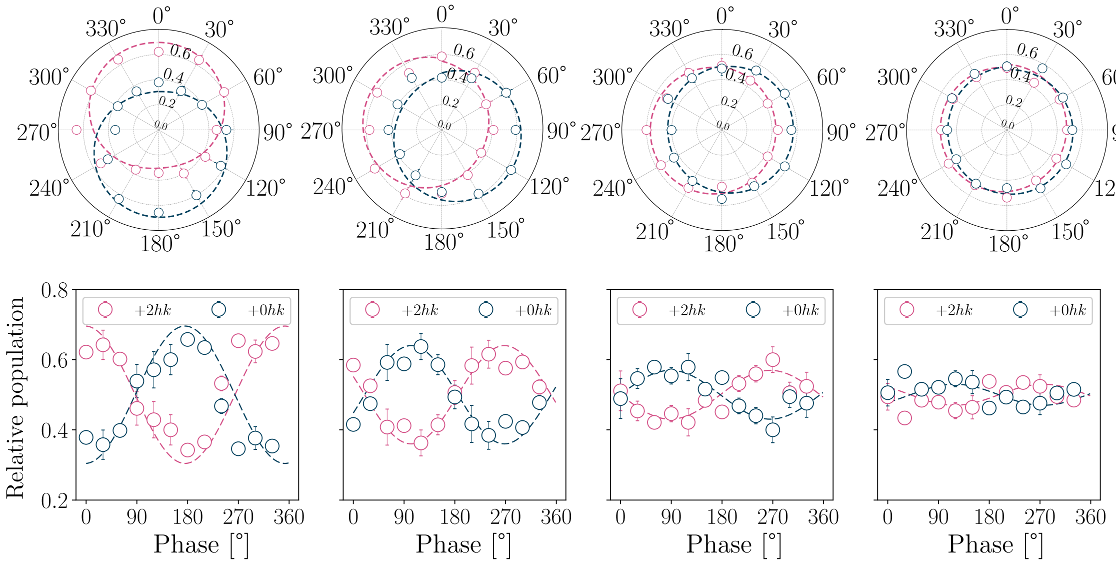

Figure 4.9: Results of the the scheme presented in Figure 4.7(b), where the $\pi/2$-pulses where applied at $\omega t = 0$ and $\omega t = 4\pi$, hence achieving relative phase control at $\omega t = 2\pi$. With this scheme coherence time of the system can be measured by decreasing the oscillation frequency in the optical dipole trap (from left to right), hence increasing the observed total coherence time (from left to right: $2\,\mathrm{ms}$, $2.5\,\mathrm{ms}$, $3\,\mathrm{ms}$ and $4\,\mathrm{ms}$). The bottom panels show the relative population of atoms in $0\hbar k$ and $2\hbar k$, where, as opposed to Figure 4.8, a clear phase dependence is observed and is damped for longer time evolution. The same data is presented in the above shown panel for visual representation in the radial diagrams. The dashed lines are results of nonlinear regression fits and show good agreement with the data.

trap oscillation frequency is the lowest corresponds to $\omega/2\pi = 498(3)\,\mathrm{Hz}$. Since the timing of the used Bragg $\pi/2$-pulses is linked to the start and finish of the oscillation period, the observed coherence times are naturally limited. Experimental results validate this approach, showing clear phase dependence, which decreases for longer separation times τ. A rotation of the axis between the two circles is attributed to a small asymmetry in the combined potentials.

It becomes apparent that, in order to maximize the readout of phase-sensitive data later in the main experimental work, temporal evolution of system parameters should be kept as short as possible and not exceed $3\,\mathrm{ms}$, as suggested by the data.

4.2 Quantum Simulation of the Periodic Quantum Rabi Model

In this section the main experimental results of the quantum simulation of the periodic quantum Rabi model are presented. In all measurements the prepared initial state is void of excitations $|N = 0\rangle$, while the qubit splitting ω_q was varied over a large frequency range. A subdivision of the measurement results is performed in the prepared states of the bases of the $\hat{\sigma}_x$ and $\hat{\sigma}_z$ operators, whereas the former, referred to as the *bare state* preparation, consists of a superposition state of the qubit eigenstates $|\pm 2\hbar k\rangle = 1/\sqrt{2}\,(|\uparrow\rangle \pm |\downarrow\rangle)$, and the latter, also designated as the *dressed state* in the following, represents the preparation in qubit eigenstates $|{\uparrow}\rangle = 1/\sqrt{2}\,(|{-2\hbar k}\rangle - |{+2\hbar k}\rangle)$ and $|{\downarrow}\rangle = 1/\sqrt{2}\,(|{-2\hbar k}\rangle + |{+2\hbar k}\rangle)$. Since the coupling strength depends on the frequency of the bosonic mode (see equation (2.17)), this parameter was mostly maintained at $g/\omega \simeq 6.5$, with the exception of the collapse and revival measurements, which were conducted at a slightly lower relative coupling strength of $g/\omega \simeq 4.8$.

4.2.1 Bare States Dynamics

For the bare states, absorption imaging in real- and momentum space, reveals atomic dynamics in mean position $\langle x\rangle$ and mean momentum $\langle p\rangle$, which then maps to the Bloch models quasimomentum $\langle q\rangle$ (see previous chapter 2). Particularly, the observed mean band occupation number $\langle \sigma_x\rangle$ and the expectation values for the bosonic excitation number $\langle N\rangle$ reveal counter-intuitive dynamics in the deep strong coupling regime.

Mean Position $\langle x\rangle$

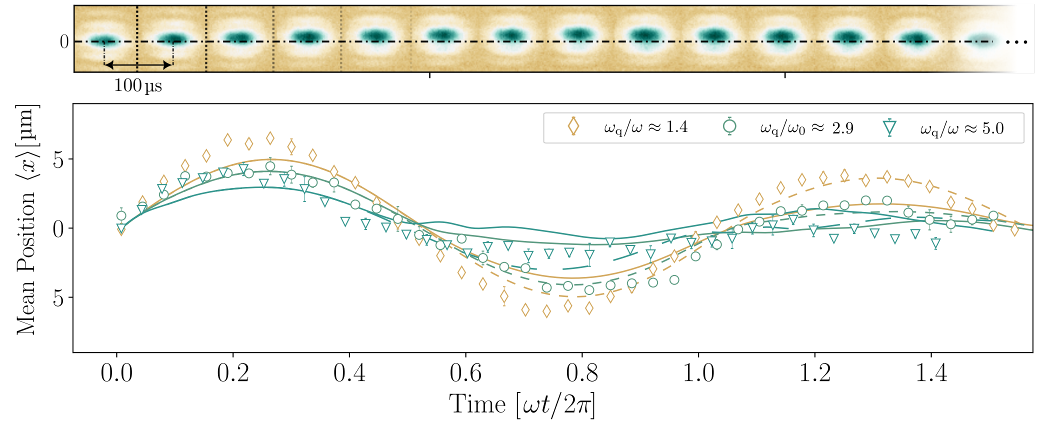

Figure 4.10: Observed temporal evolution of the mean position $\langle x\rangle$ of the atomic wavepacket prepared in the $-2\hbar k$ momentum state. The harmonic trap frequency is $\omega/2\pi = 346(8)\,\mathrm{Hz}$ resulting in a relative coupling strength of $g/\omega \simeq 6.53$. Different values of the qubit frequency $\omega_q/2\pi = 500(12)\,\mathrm{Hz}$ up to $\omega_q/2\pi = 1750(25)\,\mathrm{Hz}$ affect the depicted oscillation characteristics. While for a small ratio $\omega_q/\omega \simeq 1.4$ (yellow diamonds) the oscillation is nearly harmonic, increasing the qubit spacing up to $\omega_q/\omega \simeq 2.9$ (green circles) and $\omega_q/\omega \simeq 5.0$ (green triangles) demonstrates the emergence of the dispersive deep strong coupling regime, where the oscillation amplitude is damped and the dynamics become anharmonic. Theory lines represent numerical calculations of the mean positional dynamics in the (usual) quantum Rabi model (dashed lines) and periodic quantum Rabi model (solid lines).

In order to experimentally prepare the initial momentum state $|{-2\hbar k}\rangle = \frac{1}{\sqrt{2}}(|{\uparrow}\rangle - |{\downarrow}\rangle)$ and to analyze the temporal evolution of

$$\langle x\rangle = \sqrt{\frac{\hbar}{2m_{\mathrm{Rb}}\omega}}(\hat{a} + \hat{a}^\dagger), \tag{4.2}$$

a Bragg π-pulse is applied, to transfer the atoms in the $-2\hbar k$ momentum state. Subsequently, the atomic wavepacket is subjected to the combined potential of the harmonic trap and the periodic four-photon lattice potential. Due to limited imaging resolution ($\simeq 6\,\mu\mathrm{m}$), real space absorption images are deconvolved using the *Richardson-Lucy algorithm*, where the point-spread function (PSF) yields a density p_i, which can be used to calculate the positional expectation value $\langle x \rangle$, by summation over a vertical cut through the atomic ensemble

$$\langle x \rangle \simeq \frac{\sum_{i=0}^{N} p_i x_i}{\sum_{i=0}^{N} p_i}. \tag{4.3}$$

Here, x_i corresponds to the position, acquired by deconvolution calibration. For more details on this technique, the reader is kindly referred to the PhD thesis of J. Koch [53]. To reduce the impact of background noise, a background correction of the images was carried out prior to analysis. On top of Figure 4.10, exemplary real space images for a small qubit splitting of the atomic cloud are depicted, where each subsequent slice is $100\,\mu\mathrm{s}$ apart. Using the position of the first atomic cloud as a reference value, the temporal dynamics for different ratios of $\omega_{\mathrm{q}}/\omega$ are presented. Here the trap frequency is $\omega/2\pi = 346(8)\,\mathrm{Hz}$, yielding a relative coupling strength of $g/\omega \simeq 6.53$. The time axis is depicted in values of $\omega t/2\pi$, where $\omega t/2\pi = 1$ represents a full oscillation in the harmonic potential. While for a small qubit spacing $\omega_{\mathrm{q}}/\omega \simeq 1.4$ (yellow diamonds) a harmonic behavior is observed, increasing the ratio $\omega_{\mathrm{q}}/\omega$ from 1.4 up to 5.0, damps the oscillation amplitude and increases anharmonicity in the shown data (green triangles). This effect is understood as the emergence of the dispersive deep strong coupling regime, where the system dynamics are highly influenced by the dominating qubit energy. From another perspective the introduced localization phenomena in Section 2.2, Figure 2.10, is also a candidate for a possible explanation of the depicted dynamics. It is only due to the effect of the deep strong coupling regime, that it is possible at all to observe oscillatory dynamics, exceeding the expansion of the qubit. In other words, the macroscopic oscillation of the prepared qubit, demonstrates the strong interaction between harmonic oscillator and two level system, which was already introduced in chapter 2, Figure 2.6.

Mean Quasimomentum $\langle q \rangle$

Using the same initial state preparation and frequency values for $\omega/2\pi$ and $\omega_{\mathrm{q}}/2\pi$ as in the previous subsection, the temporal dynamics of the mean quasimomentum

$$\langle q \rangle = -i\sqrt{\frac{m_{\mathrm{Rb}}\omega}{2k}}(\hat{a} - \hat{a}^{\dagger}) \tag{4.4}$$

is also observed in momentum space. For this, after the evolution time in the superimposed potential, the atoms are free falling for a duration of $8\,\mathrm{ms}$, after the optical dipole trap potential is shut off.

Due to better separation of the atomic wavepacket in momentum space, no deconvolution of the image data is needed for this type of far field observation and the expectation value for the mean quasimomentum, which can be extracted out of the real momentum p

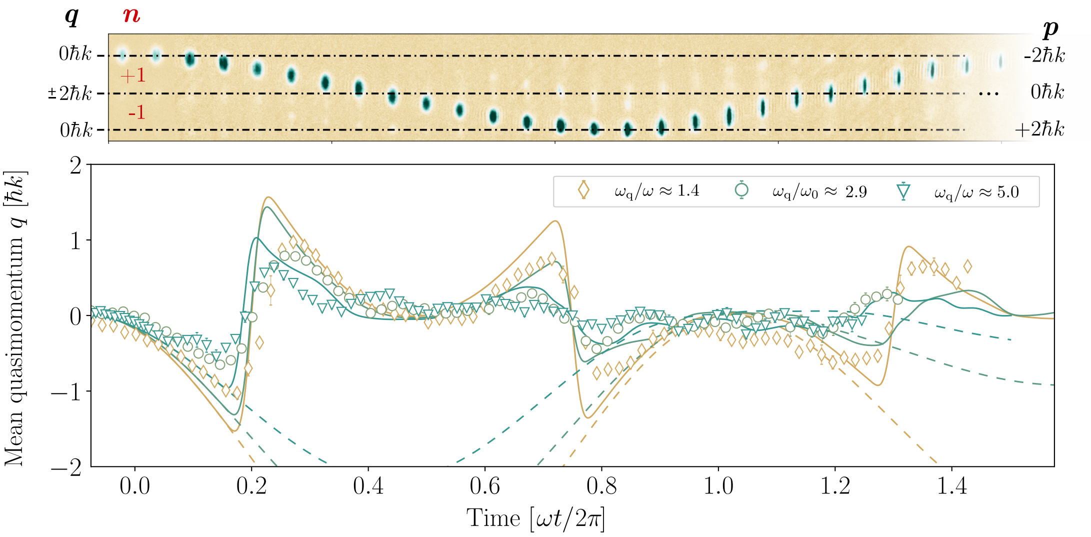

Figure 4.11: Temporal evolution of the mean quasimomentum $\langle q \rangle$ of the atomic wavepacket prepared in the $-2\hbar k$ momentum state. The same set of parameters was chosen for the qubit splitting ${}^{\omega_q}/_{2\pi}$ and harmonic trap frequency ${}^{\omega}/_{2\pi}$ as in Figure 4.10. The periodic character becomes apparent when observing the 'jump' of the mean quasimomentum at the edge of the first Brillouin zone. The magnitude of the dynamics decreases for larger values of ω_q. Theory lines represent numerical calculations of the mean momentum dynamics in the (usual) quantum Rabi model (dashed lines) and mean quasimomentum dynamics in the periodic quantum Rabi model (solid lines).

$(p = q \pm 2\hbar k)$, can be calculated with a vertical cut through the atomic ensemble

$$\langle q \rangle \simeq \frac{\sum_{i=0}^{N} p(i) q_i}{\sum_{i=0}^{N} p(i)}. \tag{4.5}$$

Again, the upper panel in Figure 4.11 shows exemplary absorption images, where each slice is again 100 µs apart in the superimposed potential. The oscillation of the atomic wavepacket starts at the real momentum $p = -2\hbar k$ (top right), which maps onto the quasimomentum $q = 0\hbar k$ (top left). Again, the temporal evolution of q was measured for the same parameter set of ${}^{\omega_q}/_{2\pi}$ as before. Here, the periodic character of the model becomes apparent, especially when comparing the theory lines in the shown data of the periodic QRM (solid lines) and the (usual) quantum Rabi model (dashed lines), for upon reaching the edge of the first Brillouin zone, the quasimomentum q jumps from $-2\hbar k$ to $+2\hbar k$. The Umklapp process of the quantum simulation is attributed to exiting the first Brillouin zone on one side and re-entering on the opposite side. Increasing the qubit spacing ${}^{\omega_q}/_{2\pi}$ again damps the magnitude of the observed dynamics, which increases the band gap energy binding the oscillatory dynamics of the system to the center of the dispersion relation at $q = 0$.

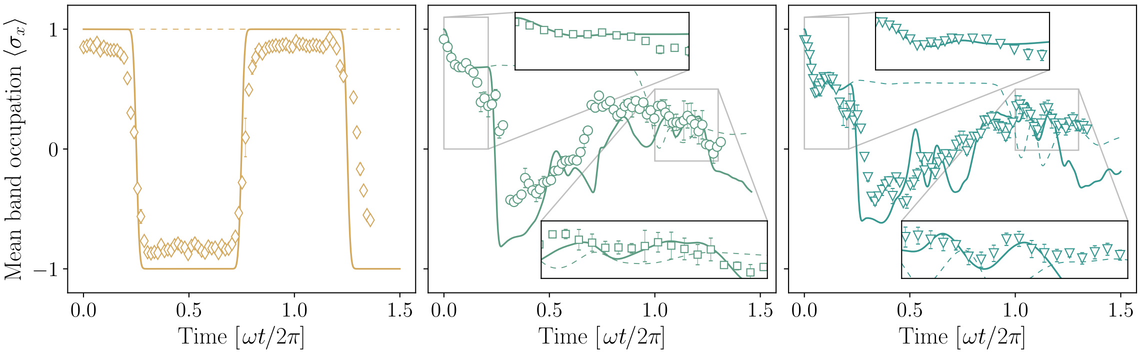

Figure 4.12: Temporal evolution of the mean band occupation $\langle\sigma_x\rangle$ for different values of the qubit splitting $\omega_\mathrm{q}/2\pi$ ranging from 0 (left panel), 1280(21) Hz (middle) and up to 1750(25) Hz (right panel). Again, the harmonic trap frequency is $\omega/2\pi = 346(8)$ Hz, resulting in a relative coupling strength of $g/\omega \simeq 6.53$. As the ratio between the qubit splitting and the harmonic trap frequency ω_q/ω increases, an oscillatory behavior can be observed between the two momentum states $\pm 2\hbar k$, which are highlighted via inset plots in the interesting regions. Theory lines are again numerical simulations for the (usual) quantum Rabi model (dashed lines) and the periodic quantum Rabi model (solid lines).

Mean Band Occupation $\langle\sigma_x\rangle$

Moving on, the temporal dynamics of the mean band occupation $\langle\sigma_x\rangle$ will be discussed by analyzing time of flight data in momentum space. Preparing the initial state as a bare state $-2\hbar k$ is in fact an eigenstate of the $\hat{\sigma}_x$ operator, which can be extracted by mapping the real measured momentum p onto the Bloch band index n as:

$$p = q + n \cdot 2\hbar k \tag{4.6}$$

where, $n = \pm 1$ is restricted to the two lowest bands (see. Figure 4.11 top left).
Figure 4.12 shows the temporal evolution of the mean band occupation for different values of the qubit splitting $\omega_\mathrm{q}/2\pi$. The harmonic trap frequency is, as in the subsections before, $\omega/2\pi = 346(8)$ Hz, resulting in a normalized coupling strength of $g/\omega \simeq 6.53$. At low lattice depths, for the small qubit approximation $\omega_\mathrm{q} \to 0$, the band index expectation value remains constant until the Brillouin zone's edge is reached, and band remapping occurs. However, at higher lattice depths, there is a significant reduction in the absolute value of the $\langle\sigma_x\rangle$ operator, leading to the emergence of the dispersive deep strong coupling regime characterized by oscillations between the momentum states. This behavior has been attributed to Rabi oscillations between the momentum states $\pm 2\hbar k$, and their most visible occurrence is at times $\omega t = 0$ and $\omega t/2\pi = 1$, which, for a more visual representation, are highlighted as inset plots. The oscillatory amplitude is significantly reduced at lower values of ω_q, where the coupling term, which is proportional to σ_x [125], becomes dominant over all other energy scales. The appearance of these oscillations is restricted to larger values of the qubit splitting, at which point the system enters the dispersive deep strong coupling regime. The data qualitatively corresponds well to the theory lines of the periodic quantum Rabi model (solid lines), especially in the areas of occurring Rabi oscillations ($\omega t = 0$ and

$^{\omega t}/_{2\pi} = 1$). In other areas, such as the edges of the Brillouin zone ($^{\omega t}/_{2\pi} \simeq 0.25; 0.75; 1.25$), a difference between theory and experimental data is observed, which is attributed to the readout process. The finite size of the atomic wavepacket, which is not included in the pQRM simulations, comes into play when the middle horizontal line in the upper panel of Figure 4.11 is reached. For vanishing qubit frequencies $\omega_\mathrm{q} \to 0$ (left panel), the sharp Umklapp process is damped. This occurs because in this case, the Bose-Einstein condensate does not instantaneously cross the boundary; instead, due to its finite size, there is a broadening of the transition. For larger qubit frequencies, the consequences are not trivial, and the behavior becomes more complex. Small changes in the wavepackets shape, which can occur due to strong lattice potentials, lead to significant deviations from the theoretical predictions, when the BEC is at the crossing region between bands.

Number of Bosonic Excitations $\langle N\rangle$

After observation of temporal dynamics in position and momentum space, a key feature of the deep strong coupling regime, namely the counter-intuitive rise of the bosonic excitation number $\langle N\rangle$

$$\hbar\omega\left(\langle N\rangle + \frac{1}{2}\right) = \frac{m\omega^2}{2}\langle x^2\rangle + \frac{1}{2m}\langle q^2\rangle \tag{4.7}$$

will be presented, where $\frac{1}{2}$ denotes the vacuum excitation in the system. Clearly $\langle N\rangle$ consists of a positional term $\langle N_x\rangle$

$$\langle N_x\rangle \simeq \frac{m\omega}{2\hbar}\frac{\sum_{i=0}^{N} p_{x,i}x_i^2}{\sum_{i=0}^{N} p_{x,i}} \tag{4.8}$$

and a (quasi-) momentum term $\langle N_q\rangle$

$$\langle N_q\rangle \simeq \frac{1}{2\hbar m\omega}\frac{\sum_{i=0}^{N} p_{q,i}q_i^2}{\sum_{i=0}^{N} p_{q,i}}, \tag{4.9}$$

which we can experimentally reveal by observing the system in real- and momentum space as shown in the previous measurements. Here $p_{x,i}$ and $p_{q,i}$ correspond to respective densities in real- and momentum space.

Previous work in our group has been conducted in the analysis of this observable for sub-cycle evolution time. Longer interaction times show predicted collapse and revival patterns of these excitations, which are presented in Figure 4.13. Here, as in the subsections before, a relative coupling strength of $^{g}/_{\omega} \simeq 6.53$ and different values for the qubit splitting $^{\omega_\mathrm{q}}/_{2\pi}$ ranging from 0 up to $1280(21)\,\mathrm{Hz}$ were applied (from left to right). Again, numerical simulations for the quantum Rabi model (dashed lines) and the periodic quantum Rabi model (solid lines) show theoretical predictions far in the deep strong coupling regime. Starting from the most left panel, the result for the case of the limit when the slow qubit approximation ($^{\omega_\mathrm{q}}/_{2\pi} \to 0$) applies is shown, for a time period of 1.5 full oscillation cycles, meaning for a harmonic trap frequency of $^{\omega}/_{2\pi} \simeq 350\,\mathrm{Hz}$ a measurement duration of

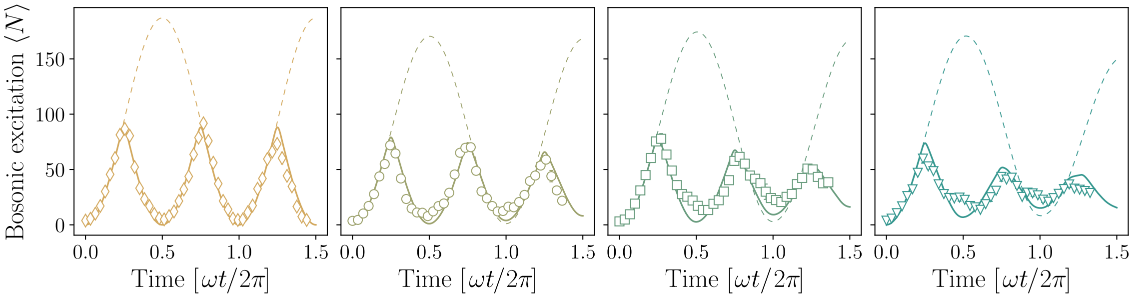

Figure 4.13: Temporal evolution of the number of excitation $\langle N \rangle$ for a qubit splitting (from left to right) $^{\omega_q}/_{2\pi} \to 0$, $^{\omega_q}/_{2\pi} = 500(12)\,\text{Hz}$, $^{\omega_q}/_{2\pi} = 800(14)\,\text{Hz}$ and $^{\omega_q}/_{2\pi} = 1280(21)\,\text{Hz}$ and a harmonic trap frequency $^{\omega}/_{2\pi} = 346(8)\,\text{Hz}$, again, resulting in a normalized coupling strength of $^{g}/_{\omega} \simeq 6.53$. Initially, atoms are prepared in a momentum state $-2\hbar k$ and the theory lines are numerical simulations of the (usual) quantum Rabi model (dashed lines) and the periodic quantum Rabi model (solid lines).

$t_{\text{meas}} \simeq 4.3\,\text{ms}$. In contrast to the well known Jaynes-Cummings regime, where the number of excitation $\langle N \rangle_{\text{JC}}$ is a conserved quantity (as can be seen Figure 2.3), a strong rise up to $\simeq 80$ excitations is observed in the experiment, representing excitation creation out of the vacuum. This is attributed as a direct consequence of the extremely strong coupled nature in this parameter regime, also confirming the discussed upper limit for the systems excitation in the previous chapter 2. Moving on, from left to right, the qubit splitting was increased up to values of $^{\omega_q}/_{2\pi} = 500(12)\,\text{Hz}$, $^{\omega_q}/_{2\pi} = 800(14)\,\text{Hz}$ and $^{\omega_q}/_{2\pi} = 1280(21)\,\text{Hz}$. Although it is technically possible to further increase the qubit splitting up to $(^{\omega_q}/_{2\pi})_{\text{max}} \simeq 5.5\,\text{kHz}$, undesired heating processes, due to scattering of near resonant laser light with the oscillating atoms in the trap, limit the applied four-photon potential during the long temporal evolution in this measurement. Nevertheless, the achieved observation time, is sufficiently long enough to demonstrate the predicted collapse and revival patterns for the bosonic excitation in the deep strong coupling regime, adding complementary results for longer interaction times to the already observed sub-cycle rise of $\langle N \rangle$ in earlier works [53]. Here, the periodicity of the presented model is laid bare, by oscillation patterns with half temporal period of the harmonic potential $T = {}^{2\pi}/_{\omega}$ (solid lines). Again, due to the remapping at the edge of the first Brillouin zone, the (usual) quantum Rabi model, shows oscillations with the full temporal period T. In each panel, the experimental data shows three peaks, representing the maximum achieved number of bosonic excitation $\langle N \rangle_{\text{max}}$ which confirms the predicted behavior for the simulated periodic quantum Rabi model, where for increasing qubit splitting $^{\omega_q}/_{2\pi}$ the observed magnitude of each peak drops. The periodic nature is once again apparent, and this observation is examined in greater detail presented in Figure 4.14.

The peak values are subjected to further analysis with respect to both time and qubit splitting $^{\omega_q}/_{2\pi}$. Subfigure 4.14(a) (bottom panel) shows the temporal evolution of the first three maximum peak values $\langle N \rangle_{\text{max}}$ for different values of the qubit splitting $^{\omega_q}/_{2\pi}$ (black data points), while the lines correspond to theoretical calculations. Experimental data qualitatively follows the predicted simulation for the periodic quantum Rabi model (solid

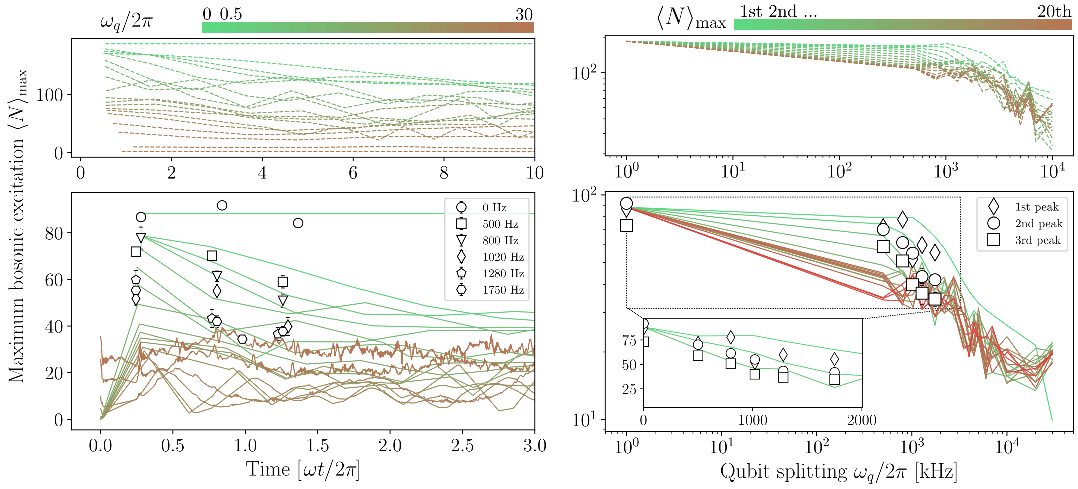

(a) **(b)**

Figure 4.14: (a) Maximum value of excitation number $\langle N\rangle_\mathrm{max}$ against time for different values of the qubit splitting. Three peaks of Figure 4.13 for each qubit splitting $\omega_\mathrm{q}/2\pi = 0$ to $\omega_\mathrm{q}/2\pi = 1750(25)$ Hz are shown along with numerical simulations for longer timescales of the periodic quantum Rabi model (lower panel, solid lines) and the (usual) quantum Rabi model (upper panel, dashed lines). The simulated data includes also larger qubit splittings up to $\omega_\mathrm{q}/2\pi = 30\,\mathrm{kHz}$. (b) $\langle N\rangle_\mathrm{max}$ versus different qubit splittings $\omega_\mathrm{q}/2\pi$, where now the behavior for each peak value is shown as a color gradient. Again theory lines show the behavior for further peak data with the numerical simulation in the periodic quantum Rabi model (solid line) and the (usual) quantum Rabi model (upper panel, dashed line). The first three peaks which can be observed in the experiment are highlighted as an inset plot with respective theory lines from the periodic quantum Rabi model.

lines), with further calculations up to 30 kHz, which are shown as a color gradient. This frequency range is currently not accessible in the experiment, nevertheless serving as a prospective illustration of system dynamics for extremely large qubit splittings. The upper panel in Figure 4.14(a) shows numerical simulations for the original quantum Rabi model, where the absolute values of $\langle N\rangle_\mathrm{max}$ are doubled, and the damping is smaller, which is attributed to the absence of the Umklapp process.

Figure 4.14(b) shows the individual behavior of each peak for different values of $\omega_\mathrm{q}/2\pi$ in double logarithmic scale. Now, the color gradient is chosen to depict the number of each peak ascending from green (first peak) to brown (20th peak). Again, in order to predict longer evolution times, up to 20 peaks are numerically simulated. The first three peaks, which are experimentally accessible and shown in Figure 4.13, are highlighted as an inset plot with linear axis, showing qualitative agreement with theory. The strong damping occurs when the qubit splitting ω_q reaches the magnitude of the coupling strength g, introducing the emergence of the dispersive deep strong coupling regime [27].

In summary, the results show that there is a weak dependence of the maximal achieved excitation numbers $\langle N\rangle$ on the energy gap for $\omega_\mathrm{q} \ll g$, but a significant reduction occurs for energies that approach the coupling strength. Prospective numerical simulations suggest a possible similarity to a known quantum phase transition and further theoretical investigations are needed to fully understand this effect [107, 126, 127].

4.2.2 Dressed State Dynamics

Having discussed several temporal dynamics of the initial state prepared in the bare states of the qubit, which are eigenstates of the $\hat{\sigma}_x$ operator, this section presents experimental results for eigenstates of the $\hat{\sigma}_z$ operator. Preparing such a state can be done by using a superposition of two bare states $\pm 2\hbar k$, resulting in initially prepared dressed states:

$$\psi_{\uparrow} = |N=0,\uparrow\rangle = |N=0\rangle \otimes \frac{1}{\sqrt{2}}(|-2\hbar k\rangle - |+2\hbar k\rangle) \text{ upper band} \tag{4.10}$$

$$\psi_{\downarrow} = |N=0,\downarrow\rangle = |N=0\rangle \otimes \frac{1}{\sqrt{2}}(|-2\hbar k\rangle + |+2\hbar k\rangle) \text{ lower band} \tag{4.11}$$

Again the number of prepared excitation is $N = 0$ as in the previous section. There are two aspects of interest in this context. Firstly, the states $|N = 0, \uparrow\rangle$ and $|N = 0, \downarrow\rangle$ that have been set up, are representative of the Jaynes-Cummings model, enabling better comparison of the results with those of established systems. Secondly, in contrast to the earlier considered states, these states have a distinct parity which is an essential property of the model because of the $\mathbb{Z}_2$ symmetry of the quantum Rabi Hamiltonian (as seen in Figure 2.1). Collapse and revival of an initially prepared eigenstate in the $\hat{\sigma}_z$ basis devoid of excitations ($|N = 0\rangle$) will be presented in this section, demonstrating quantum coherence for longer time interactions in the deep strong coupling regime of the periodic quantum Rabi model. Another observed phenomenon in the following section is the dependence of the periodic quantum Rabi evolution on the qubit eigenstate of preparation, showing phase dependent temporal dynamics of the bosonic excitation number $\hat{N}$ for the initial state prepared in the upper- and lower band described by equations (4.10) and (4.11), respectively.

Qubit Eigenstate Readout

In order to prepare an eigenstate of $\hat{\sigma}_z$, which are superposition states of the momentum picture eigenstates, atoms are simultaneously irradiated by two Bragg pulses of counter propagating momentum transfer. Figure 4.15 shows the preparation of such a state, where the amplitude of each Bragg beam is increased from $-17\,\mathrm{dBm}$ to $-11\,\mathrm{dBm}$ such that the population in $0\hbar k$ is transferred equally to the $+2\hbar k$ and $-2\hbar k$ momentum states. Due to the finite velocity distribution of atoms during preparation, a minor fraction (less than $5\,\%$) remains in the $0\hbar k$ momentum state within the trap center. Consequently, these residual atoms have the potential to collide with oscillating atoms during the temporal evolution, which may subsequently reduce the observed contrast in the experiment. The right panel shows time of flight absorption images, representing the preparation of the initial state. Depending on the relative phase between the atomic wavepackets in $+2\hbar k$ and $-2\hbar k$, the prepared initial qubit state changes from $|N = 0, \downarrow\rangle$ to $|N = 0, \uparrow\rangle$. This can be adjusted by changing the relative phase between the counter propagating Bragg pulses. Since the imaging resolution of $\simeq 6\,\mu\mathrm{m}$ does not allow for observation of fringe patterns in real space, an alternative route of extracting the state information using a $\pi/2$ four-photon Raman

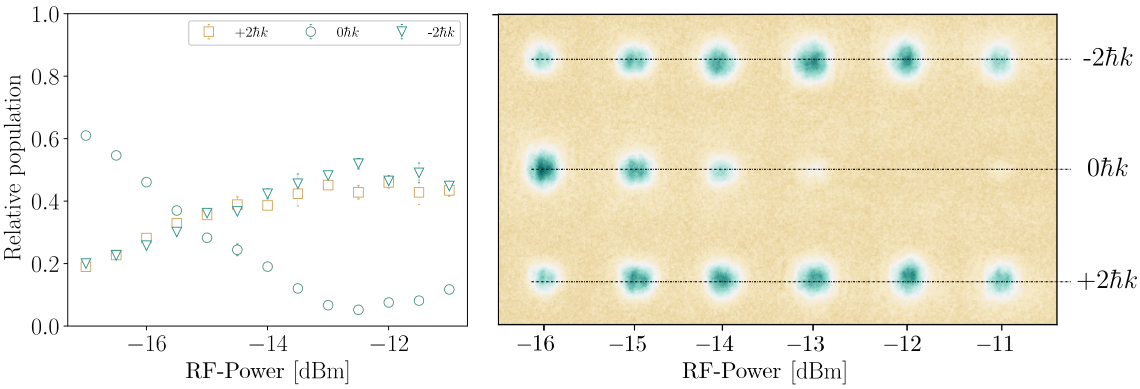

Figure 4.15: Preparation of the initial state using two counter propagating Bragg pulses with opposing momenta. The left panel shows the preparation by increasing the RF-power applied onto both AOM's used to control the Bragg beam intensities. Atoms from $0\hbar k$ (green circles) are transferred to the neighboring $+2\hbar k$ (yellow squares) and $-2\hbar k$ (green triangles) momentum states via the respective Bragg beam. The right panel shows absorption time of flight images for the corresponding data.

pulse, which gives insight into the eigenstate of $\hat{\sigma}_z$, has been experimentally implemented in the context of this work.

In order to demonstrate this, after preparing an initial state where the relative phase between the Bragg beams is $\varphi_{\text{prep}} = 0°$ a Raman readout pulse with a relative phase of $\varphi_{\text{readout}} = 90°$ ($^{\pi}/_{2}$-pulse) is applied. This Raman pulse is tuned to drive transfer between the momentum states $-2\hbar k$ and $+2\hbar k$, generating a maximum contrast in population difference for the case of $\Delta\varphi = \varphi_{\text{readout}} - \varphi_{\text{prep}} = 90°$. Varying the preparation phase, now results in an oscillatory behavior of atomic population in the momentum states, which is depicted in Figure 4.16. Here, the readout phase is kept constant, while the preparation phase is changed from 0 to 360°. The upper panel shows time of flight absorption images matching to the x-axis of the data below. Fitting sinusoidal functions to the data, shows also a small oscillation in the $0\hbar k$ momentum state, suggesting the presence of two photon processes, which can be suppressed by further increase of the two-photon detuning δ. It appears, that these oscillations are in phase with the $+2\hbar k$ momentum state, hinting at a slight asymmetry introduced into the system during the preparation phase. This assumed asymmetry effect is already observed during the coherence characteristics in earlier measurements shown in Figure 4.9. For this reason, it is chosen to increase the two photon detuning from $^{\delta}/_{2\pi} = 160\,\text{kHz}$ to $^{\delta}/_{2\pi} = 210\,\text{kHz}$ at the expense of the four-photon lattice potential (as introduced in section 4.1.1, Figure 4.1(b)). This results in further suppression of the $0\hbar k$ momentum state population depicted in the right panel of Figure 4.17(a). To ensure low inter-atomic collisions with residual atoms in the $0\hbar k$ momentum state, a high detuning value of $^{\delta}/_{2\pi} = 210\,\text{kHz}$ is crucial for the readout process and the application of the four photon lattice potential during temporal evolution measurements. This is necessary, as these collisions can cause undesired heating, which becomes more pronounced over extended duration of light-matter interaction.

Moving on, the same readout pulse is applied after a full time oscillation of the initially

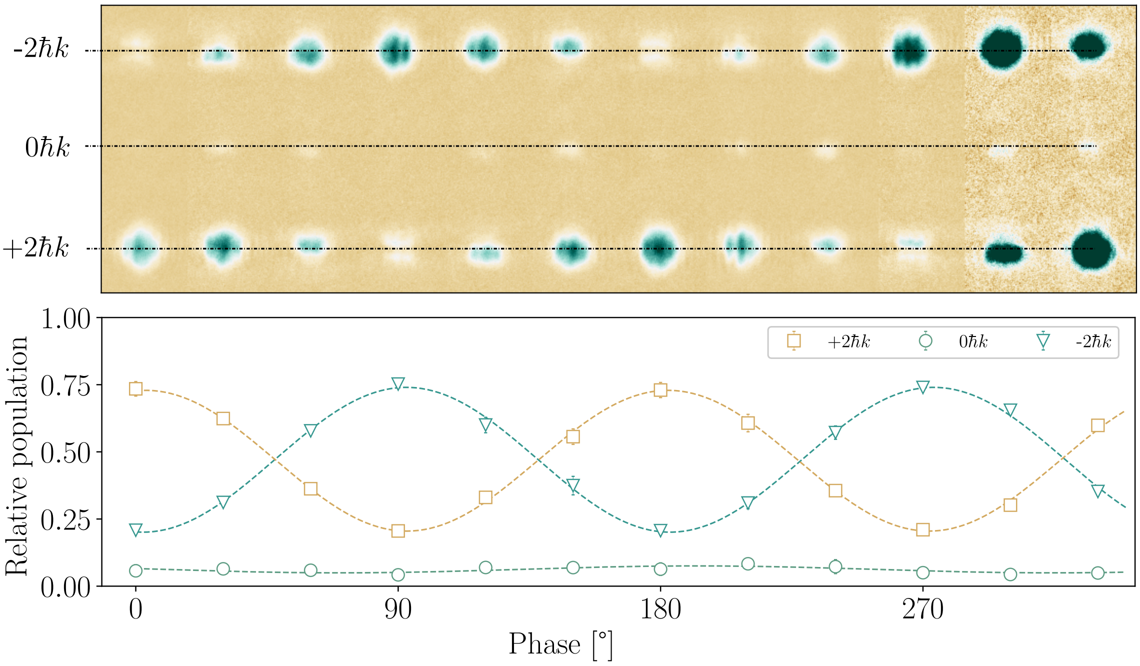

Figure 4.16: Analyzing the initial state by applying a $\pi/2$ four-photon Raman pulse with a fixed phase φ_{readout} and changing the relative preparation phase φ_{prep} between the used Bragg pulses. A clear expected oscillatory behavior is observed, where dependent on the prepared phase, different number of atoms are populating the momentum states $0\hbar k$ (green circles), $-2\hbar k$ (yellow squares) and $+2\hbar k$ (green triangles). The fitted curves are sinusoidal functions describing the process and the panel above shows corresponding absorption time of flight images.

prepared atoms in the harmonic trap potential. Figure 4.17(b) shows the results of such a measurement for a trap frequency of $\omega/2\pi = 656(22)\,\text{Hz}$. Here an expected revival at $t_{2\pi} \simeq 1500\,\text{ms}$ can be probed, by again varying the preparation phase at a fixed time $t_{2\pi}$. Despite the reduction in contrast of the data when compared to the left panels, there are still evident signs of phase dependence, indicating that the phase coherence has been preserved. This is particularly important in accurately measuring the eigenstate population of the qubit, as it allows for the observation of collapse and revival of an initially prepared eigenstate of $\hat{\sigma}_z$.

Collapse and Revival of the Qubit Eigenstate

After implementing the phase-dependent readout scheme for upcoming measurements, temporal dynamics for different qubit splittings ($\omega_q/2\pi$) of a state initially prepared in the eigenstate of $\hat{\sigma}_z$ are presented. As previously mentioned, the atoms are initially prepared in the qubit eigenstate $|N = 0, \downarrow\rangle$ described by equation (4.11), which is a superposition of the momentum states $\pm 2\hbar k$ with a relative phase between the two wavepackets $\varphi_{\text{prep}} = 0°$. After an evolution time t, where atoms are evolving in the superimposed lattice- and harmonic trapping potential, applying a four-photon readout pulse with $\varphi_{\text{readout}} = 90°$, a population difference $n_{p<0} = (N_{p<0} - N_{p>0})/(N_{p<0} + N_{p>0})$ between the two momentum

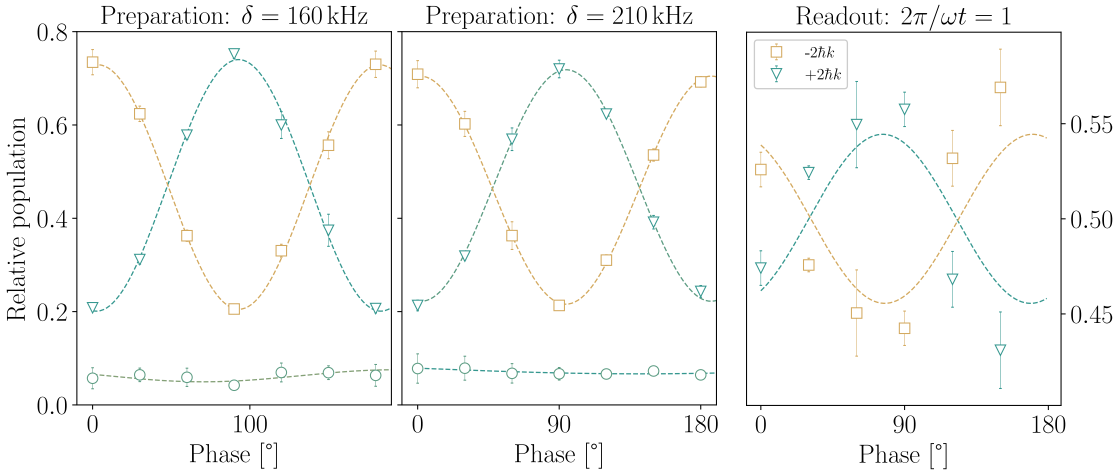

(a) **(b)**

Figure 4.17: (a) Preparation of the initial state (at time $t = 0$) with a two photon detuning $\delta/2\pi = 160\,\mathrm{kHz}$ and $\delta/2\pi = 210\,\mathrm{kHz}$ showing better suppression of two photon processes, evident in fewer atoms populating the $0\hbar k$ momentum state for higher values of $\delta/2\pi$. (b) The same initial preparation and readout pulse as in Figure 4.17(a) (right panel) is applied after a full oscillation of atoms ($t_{2\pi} \simeq 1500\,\mathrm{ms}$) in the harmonic trap with the frequency $\omega/2\pi = 656(22)\,\mathrm{Hz}$. The data shows reduced contrast for the population difference of atoms in $+2\hbar k$ (yellow squares) and $-2\hbar k$ (green triangles) when comparing it to the left data, nevertheless a clear oscillatory behavior is visible, proving phase coherence at full period of oscillation.

states is induced, where $N_{p<0}$ and $N_{p>0}$ depict atom numbers detected with momentum $p < 0$ and $p > 0$, respectively. During the analysis, these atoms are counted as depicted in the absorption images in the upper panel of Figure 4.18. Counting errors arise due to the finite size of the BEC at oscillation times of $\omega t/2\pi = 0.25$, when the atomic wavepackets are not distinguishable due to overlapping momentum states oscillating after a quarter period in the harmonic trap. To compensate for this, a background correction is implemented, where for each time step, an additional image is observed without the readout pulse and subsequently compared to the absorption image of the initial state. This provides a correlation factor that can be used for statistical weighting during the image analysis process. An exemplary result is depicted in the lower left plot of Figure 4.18, where the green and gray lines represent data with and without correction, respectively. Generally, both data sets show the same behavior, especially for the oscillation times when the atomic wavepackets are well distinguishable. However, a slight correction is applied at the edge of the counting region between $N_{p<0}$ and $N_{p>0}$.
After introducing the experimental tools of phase extraction and background correction, The bottom right panel in Figure 4.18 presents the experimental data of the temporal evolution for different qubit splittings $\omega_q/2\pi \in [0; 1280(21)\,\mathrm{Hz}]$. Considering the coherence times observed in the section 4.1.3, a higher harmonic trap frequency of $\omega/2\pi = 656(22)\,\mathrm{Hz}$ is selected to reduce the time required for observing a full oscillation period, resulting in a normalized coupling strength $g/\omega \simeq 4.8$.

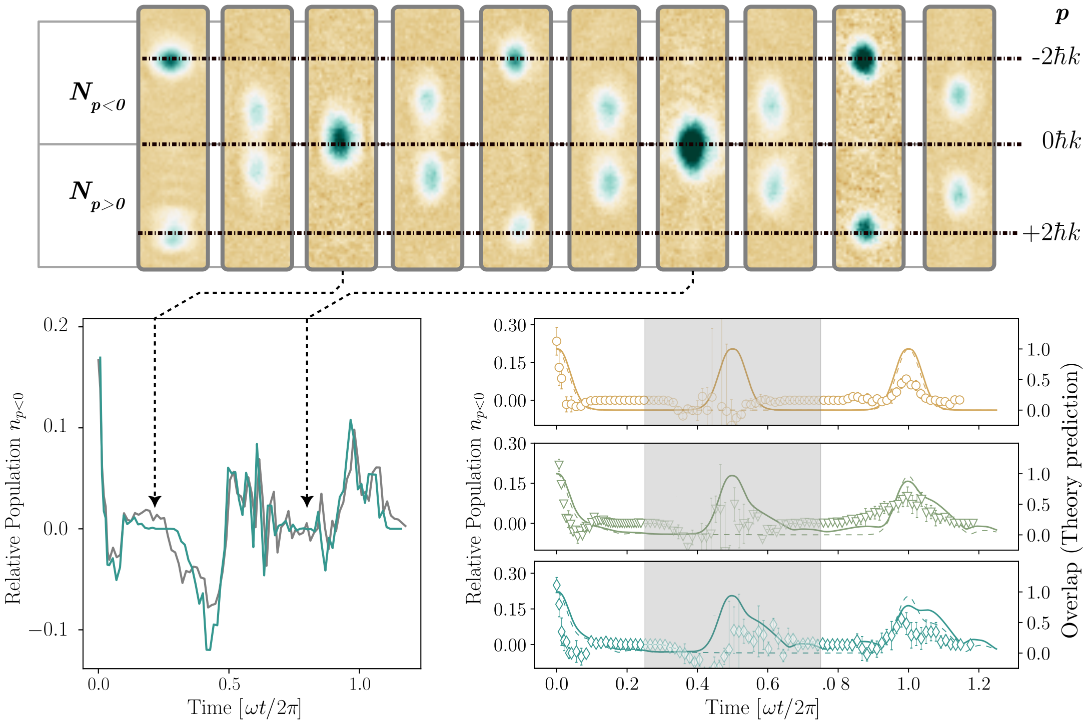

Figure 4.18: Upper panel: Exemplary absorption images taken for a qubit splitting of ${}^{\omega_\mathrm{q}}/_{2\pi} \to 0$ to illustrate the counting process (upper panel). Atoms above (below) the $0\hbar k$ line are counted as $N_{p<0}$ ($N_{p>0}$) resulting in large counting errors when the overlapping wavepackets are not distinguishable near zero line. The panel below on the left, shows results of the background corrected data (green) in comparison to no correction (gray). Lower right panel: Temporal evolution of the relative number of atoms $n_{p<0} = (N_{p<0} - N_{p>0})/(N_{p<0} + N_{p>0})$ (left vertical scale) for a harmonic trap frequency of ${}^{\omega}/_{2\pi} = 650(21)$ Hz and different qubit splittings ${}^{\omega_\mathrm{q}}/_{2\pi} \to 0$ (top), ${}^{\omega_\mathrm{q}}/_{2\pi} = 800(14)$ Hz (middle) and ${}^{\omega_\mathrm{q}}/_{2\pi} = 1280(21)$ Hz (bottom) show collapse and revival of an initially prepared state in the eigenbasis of $\hat{\sigma}_z$. Dashed and solid lines represent the theory of the (usual) quantum Rabi model and the periodic variant, respectively, while the corresponding vertical scale is on the right side. The shaded area indicates experimentally inaccessible regions due to instrumental phase fluctuations.

After a variable interaction time in the combined potential, the ${}^{\pi}/_{2}$ four-photon Raman pulse is applied. When the initial state is fully revived, a transfer of atoms to the momentum state $-2\hbar k$ occurs and $\sigma_z = 1$. The left vertical scale shows the experimental data for the relative population $n_{p<0}$, where the absolute contrast is reduced due to the finite momentum distribution of the atoms. The upper panel, representing the case for vanishing qubit splitting $\omega_\mathrm{q} \to 0$, demonstrates a rapid collapse of the initial state and a revival at full oscillation time ${}^{\omega t}/_{2\pi} = 1$, indicating a proof of principle and phase control of the experimental apparatus for such long interaction times. Increasing the qubit splitting up to ${}^{\omega_\mathrm{q}}/_{2\pi} = 800(14)$ Hz (middle panel) and ${}^{\omega_\mathrm{q}}/_{2\pi} = 1280(21)$ Hz (lowest panel) reveals visible substructures in the observed revival of the qubit state, where predicted partial revivals emerge in a more broadened area representing the interference of photon number wavepackets [109]. The collapse of the shown initial state verifies the predicted behavior for $\langle\sigma_z\rangle$, extracted with a phase-sensitive analysis method, demonstrating the presence of the perturbative deep strong coupling regime. The strongly coupled oscillatory modes promote the dominance of energy exchange between the qubit and harmonic potential, causing the collapse of the initial state within a small amount of time ($t \simeq 90\,\mu\mathrm{s}$).

The shaded region, shown approximately at half the revival time, is characterized by significant phase fluctuations as mentioned in previous Sections 4.1.3. These are attributed to mechanical vibrations of the lattice beams relative to the dipole trapping beam and are considered inaccessible to the experiment. However, when the atoms return to the starting position after $\omega t/2\pi = 1$, the relative phase becomes relevant, enabling the extraction of phase information.

The experimental data qualitatively agrees with predictions of the periodic quantum Rabi model (solid lines), for which the right vertical axis shows the numerically simulated overlap with the initial state $\langle\Psi_{\mathrm{ini}}(t=0)|\Psi(t)\rangle$. The dashed line shows the predictions of the (usual) quantum Rabi model, where it is noticeable that no revival at half the period of the oscillation time is predicted. The observation of collapse and revival of an initially prepared vacuum state prepared in the qubits eigenstate expands the observed temporal dynamics further than the edge of the first Brillouin zone, adding complementary results to previous works in our group [53].

Number of Bosonic Excitations for Dressed State Preparations

Moving on, final measurements regarding the bosonic excitation number $\langle N\rangle$, where this time the preparation is performed in both qubit eigenstates described by equations (4.10) and (4.11), will be presented. The same image analysis method is used as in the prior Section 4.2.1, this time utilizing the relative phase between the two Bragg pulses to prepare the initial states $|N=0,\uparrow\rangle$ ($\varphi_{\mathrm{prep}} = 90°$) and $|N=0,\downarrow\rangle$ ($\varphi_{\mathrm{prep}} = 0°$), respectively. The temporal evolution of both initial preparations are observed for different values of the qubit splitting $\omega_{\mathrm{q}}/2\pi \in [0{,}1280(21)]\,\mathrm{Hz}$ and a fixed value of the harmonic trap frequency $\omega/2\pi = 346(8)\,\mathrm{Hz}$, resulting in a normalized coupling of $g/\omega \simeq 6.53$.

The inset plot in the upper panel of Figure 4.19(a) shows numerical simulations for the temporal evolution of a state prepared in $|N=0,\downarrow\rangle$ (dashed) and $|N=0,\uparrow\rangle$ (solid) for the periodic quantum Rabi model with a qubit splitting of $\omega_{\mathrm{q}}/2\pi = 1280(21)\,\mathrm{Hz}$. An interesting behavior can be observed, when taking the difference between the reached bosonic excitation numbers, shown in the upper panel of Figure 4.19(a), where the left vertical axis corresponds to obtained data, showing the difference $\Delta N = N_\uparrow - N_\downarrow$ measured in the experiment. The solid line, which changes the color according to the positive (green) or negative (yellow) sign of ΔN, is the difference obtained by numerical simulations and has a corresponding vertical axis on the right side. As is attributed to collision and heating of atoms in the trap, especially for longer oscillation times, the observed magnitude, when comparing both vertical axes, is strongly reduced. This effect still remains, even when using low atom numbers, as explored in Section 4.1.3, Figure 4.8. Another reason, which makes this measurement challenging is the limited resolution of the image in real space, presenting a greater challenge in this scenario compared to the measurements described in Section 4.2.1. The two initially prepared wave packets move separately, cutting the

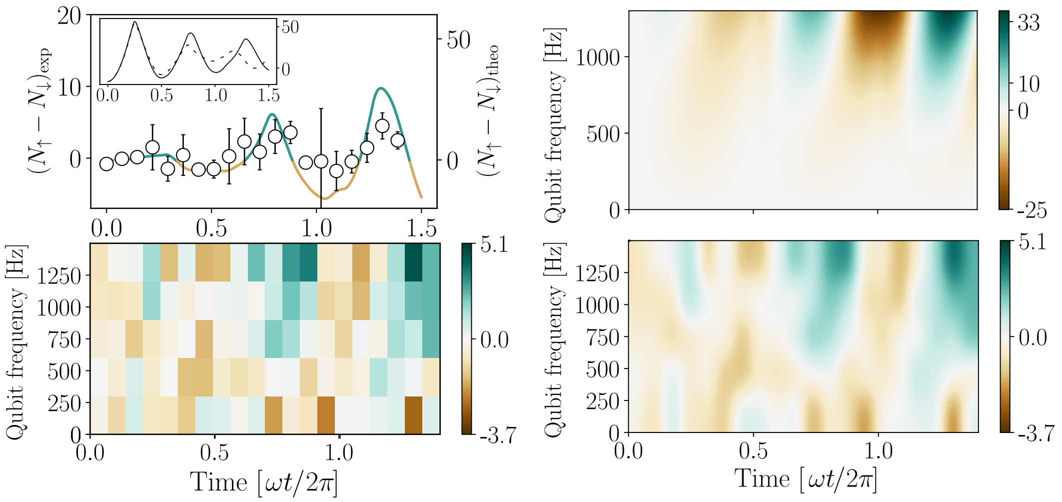

(a) **(b)**

Figure 4.19: (a) Temporal evolution of the bosonic excitations for an initially prepared state $|N=0,\downarrow\rangle$ (dashed line in the inset plot, upper panel) and $|N=0,\uparrow\rangle$ (solid line in the inset plot, upper panel) for a qubit splitting $^{\omega_q}/_{2\pi} = 1280(21)$ Hz and trap frequency $^{\omega}/_{2\pi} = 346(8)$ Hz. The upper panel shows the difference $\Delta N = N_\uparrow - N_\downarrow$ measured in the experiment (left vertical scale) along with theoretical prediction (right vertical axis). The lower panel shows the temporal evolution for various qubit splitting $^{\omega_q}/_{2\pi} \in [0{,}1280(21)]$ Hz with the difference ΔN depicted as a gradient from yellow (negative values) to green (positive values). (b) Comparison of the interpolated data from (a) (lower panel) with numerical simulations in the periodic quantum Rabi model (upper panel).

resolution in half, leading to uncertainty that results in an overestimation of the initial excitations and a reduction in the measured contrast between the two sets of measurements. Nevertheless the data qualitatively agrees with theory and further qubit splitting ranging from 0 up to the just discussed $^{\omega_q}/_{2\pi} = 1280(21)$ Hz are investigated in the lower panel of Figure 4.19(a). Here, the color gradient depicts the difference of excitations ΔN as a temporal evolution for different values of the qubit splitting. An interesting pattern arises, when crossing a qubit splitting of $^{\omega_q}/_{\omega} \simeq 700$ Hz, where the created difference in number of excitations is strongly dependent on the initial state of preparation, which introduces a transition region in which due to the emerging dominance of the qubit energy, the dispersive deep strong coupling regime is approached. This phenomenon of phase dependent creation of bosonic excitation has already been documented in earlier works of J. Koch [53], but due to limited sub-cycle observation times, the oscillatory nature of this dependency was not observed. In this work, the corresponding effects are observed beyond the first Brillouin, where the periodic quantum Rabi model applies. Since experimental cycle times limit the long-term stability, only a finite amount of qubit splittings and course time steps (150 µs) are used to complete the full diagram. Using Gaussian interpolation between the data points allows for better comparison of the experimental data (lower panel) with numerical simulations (upper panel), presented in Figure 4.19(b), again showing qualitatively good agreement with reduced magnitude.

CHAPTER 5

Conclusions

In the frame of this dissertation, an analog quantum simulation utilizing ultra-cold rubidium atoms has been employed to observe the deep strong coupling regime of the periodic quantum Rabi model. After performing preparatory measurements describing the accessible parameter range for the characteristic frequencies and verifying the system coherence preservation with interferometric measurements, the characteristics of the extremely strong coupled system is explored by observing the temporal dynamics in position and momentum space. A distinction was made in terms of initial state preparation, which are performed either in the qubit's superposition- $\Psi_{\text{ini}} = |\pm 2\hbar k\rangle$ or in the qubit's eigenstate preparation $\Psi_{\text{ini}} = |\uparrow\rangle, |\downarrow\rangle$. Previous results for short time interaction consisting of measurements of the bosonic excitation number $\hat{N}$ and the mean band occupation number $\hat{\sigma}_x$ have first been verified, and then extended to longer interaction times beyond the range of the first Brillouin zone, where in addition to the previously mentioned observables, now the collapse and revival of an initial vacuum state prepared in the $\hat{\sigma}_z$ basis is reported. When the temporal limitations within the first Brillouin zone are removed and the broad tunability range of qubit splitting comes into play, the previously reported difference in attained excitation count, $\Delta N = N_\uparrow - N_\downarrow$, displays oscillatory patterns. This is in contrast to the earlier presumed settled dynamics, contributing to an enhanced understanding of this phenomenon, which still poses a challenge to full comprehension.
In summary, the aforementioned measurement results could also be verified in the periodic quantum Rabi model. Further, with the ability to realize longer interaction times, the observation of the collapse and revival of an initially prepared vacuum state has been conducted. This stands as a direct proof of the perturbative deep strong coupling in the periodic quantum Rabi model, and while it being a periodic variant of the usual quantum Rabi model, an observed similarity in theoretical simulations shows a significant connection between the two models [109].

In the future, a quantum phase transition predicted in the quantum Rabi model [107, 126, 127], as can be achieved by the relative coupling strength within the system and addressed through qubit splitting, could serve as intriguing options for exploration. While the achievement of the former has been demonstrated in a trapped ion setup [128], applying the latter pathway to the present system holds significant promise for this experimental configuration, due to its highly tunable qubit splitting range and larger possible relative coupling strength. Another interesting choice of exploration could be using Feshbach resonances to tune the interaction when using the Rubidium 85 isotope (or Kalium 39 isotopes), introducing variable interactions onto the system. Further, as already described in the main text, a striking similarity of the relevant Hamiltonian to superconducting qubit systems could be further explored in the future as an interesting platform for simulating quantum information processing applications [36, 129].

A Further Calculations on Superconducting Qubits

A.1 Derivation of the Fluxonium Hamiltonian for Arbitrary Phase Values

Consider the Schrödinger equation

$$H = 4E_c \left(\frac{Q}{2e}\right)^2 + \frac{1}{2}E_L\varphi^2 - E_J\cos\left(\varphi - \varphi_{\text{ext}}\right) \tag{A.1}$$

We can then separate a solution of the Schrödinger equation, into rapidly varying and slowly varying parts. Exponential functions may be used to describe rapidly varying parts and the slowly varying parts are $\Psi_{\uparrow}\left(\varphi,t\right)$ and $\Psi_{\downarrow}\left(\varphi,t\right)$ for "right" and "left" movers, respectively:

$$i\frac{\partial}{\partial t}\left[\Psi_{\uparrow}\left(\varphi,t\right)\exp\left(-i\frac{\varphi}{2}\right) + \Psi_{\downarrow}\left(\varphi,t\right)\exp\left(i\frac{\varphi}{2}\right)\right] =$$

$$-4E_c\frac{\partial^2}{\partial\varphi^2}\left[\Psi_{\uparrow}\left(\varphi,t\right)\exp\left(-i\frac{\varphi}{2}\right) + \Psi_{\downarrow}\left(\varphi,t\right)\exp\left(i\frac{\varphi}{2}\right)\right] +$$

$$\frac{1}{2}E_L\varphi^2\left[\Psi_{\uparrow}\left(\varphi,t\right)\exp\left(-i\frac{\varphi}{2}\right) + \Psi_{\downarrow}\left(\varphi,t\right)\exp\left(i\frac{\varphi}{2}\right)\right] -$$

$$\frac{E_J}{2}\left[\exp\left(i\left(\varphi-\varphi_{\text{ext}}\right)\right) + \exp\left(-i\left(\varphi-\varphi_{\text{ext}}\right)\right)\right]\left[\Psi_{\uparrow}\left(\varphi,t\right)\exp\left(-i\frac{\varphi}{2}\right) + \Psi_{\downarrow}\left(\varphi,t\right)\exp\left(i\frac{\varphi}{2}\right)\right]$$

Different powers of the exponential $\exp\left(i\frac{\varphi}{2}\right)$ are linearly independent, so we can separate the above equation into two equations

---

Some details

$$-\frac{\partial^2}{\partial\varphi^2}\left[\Psi_{\uparrow}\left(\varphi,t\right)\exp\left(-i\frac{\varphi}{2}\right)\right] = -\exp\left(-i\frac{\varphi}{2}\right)\frac{\partial^2\Psi_{\uparrow}\left(\varphi,t\right)}{\partial\varphi^2} + i\exp\left(-i\frac{\varphi}{2}\right)\frac{\partial\Psi_{\uparrow}\left(\varphi,t\right)}{\partial\varphi} +$$

$$\frac{1}{4}\exp\left(-i\frac{\varphi}{2}\right)\Psi_{\uparrow}\left(\varphi,t\right)$$

$$i\frac{\partial}{\partial t}\Psi_{\uparrow}\left(\varphi,t\right) = -4E_c\frac{\partial^2\Psi_{\uparrow}\left(\varphi,t\right)}{\partial\varphi^2} + 4iE_c\frac{\partial\Psi_{\uparrow}\left(\varphi,t\right)}{\partial\varphi} + E_c\Psi_{\uparrow}\left(\varphi,t\right) +$$

$$\frac{1}{2}E_L\varphi^2\Psi_{\uparrow}\left(\varphi,t\right) + \frac{E_J}{2}\exp\left(i\varphi_{\text{ext}}\right)\Psi_{\downarrow}\left(\varphi,t\right)$$

$$i\frac{\partial}{\partial t}\Psi_{\downarrow}(\varphi,t) = -4E_c\frac{\partial^2\Psi_{\downarrow}(\varphi,t)}{\partial\varphi^2} - 4iE_c\frac{\partial\Psi_{\downarrow}(\varphi,t)}{\partial\varphi} + E_c\Psi_{\downarrow}(\varphi,t) +$$
$$\frac{1}{2}E_L\varphi^2\Psi_{\downarrow}(\varphi,t) + \frac{E_J}{2}\exp(-i\varphi_{\text{ext}})\,\Psi_{\uparrow}(\varphi,t)$$

where the oscillatory terms are neglected. Substituting the coordinate operator $\varphi = i\frac{\partial}{\partial p}$, we obtain the Hamiltonian in the p representation,

Or in more compact form

$$i\frac{\partial}{\partial t}\begin{pmatrix}\Psi_{\uparrow}\\ \Psi_{\downarrow}\end{pmatrix} = H\begin{pmatrix}\Psi_{\uparrow}(\varphi,t)\\ \Psi_{\downarrow}(\varphi,t)\end{pmatrix}, \tag{A.2}$$

where

$$H = \left(-\frac{E_L}{2}\frac{\partial^2}{\partial x^2} + 4E_c x^2\right)\mathbb{1} + 4xE_c\sigma_z + \frac{E_J}{2}\left(\sigma_x\cos\varphi_{\text{ext}} - \sigma_y\sin\varphi_{\text{ext}}\right),$$

and

$$\mathbb{1} = \begin{pmatrix}1 & 0\\ 0 & 1\end{pmatrix}$$

After rotation about z axis

$$\sigma_x\cos\varphi_{\text{ext}} - \sigma_y\sin\varphi_{\text{ext}} = \exp\left(-i\frac{\varphi_{\text{ext}}}{2}\sigma_z\right)\sigma_x\exp\left(i\frac{\varphi_{\text{ext}}}{2}\sigma_z\right),$$

The Schrodinger equation takes the form

$$i\frac{\partial}{\partial t}\begin{pmatrix}\Psi_{\uparrow}\\ \Psi_{\downarrow}\end{pmatrix} = \exp\left(-i\frac{\varphi_{\text{ext}}}{2}\sigma_z\right)H_{eff}\exp\left(i\frac{\varphi_{\text{ext}}}{2}\sigma_z\right)\begin{pmatrix}\Psi_{\uparrow}\\ \Psi_{\downarrow}\end{pmatrix},$$

where

$$H_{eff} = -\frac{E_L}{2}\frac{\partial^2}{\partial x^2} + 4E_c x^2 + 4xE_c\sigma_z + \frac{E_J}{2}\sigma_x.$$

By the gauge transformation

$$\begin{pmatrix}\Phi_{\uparrow}\\ \Phi_{\downarrow}\end{pmatrix} = \exp\left(i\frac{\varphi_{\text{ext}}}{2}\sigma_z\right)\begin{pmatrix}\Psi_{\uparrow}\\ \Psi_{\downarrow}\end{pmatrix} \tag{A.3}$$

we arrive at the following Schrodinger equation

$$i\frac{\partial}{\partial t}\begin{pmatrix}\Phi_{\uparrow}\\ \Phi_{\downarrow}\end{pmatrix} = H_{\text{eff}}\begin{pmatrix}\Phi_{\uparrow}\\ \Phi_{\downarrow}\end{pmatrix}$$

Hence we see that the phase does not play a role, i.e. it can be eliminated by the gauge transformation (A.3).

With a simple comparison of the Eq. (A.1) and Eq. (1) introduced in [109] one obtains

$$E_c = \frac{2\hbar k_0^2}{m}, \omega_q = E_J, E_L = \frac{m\omega_0^2}{16k_0^2\hbar}$$

we obtain

$$k_0^2 = \frac{E_c m}{2\hbar}, \omega_0^2 = \frac{16E_L k_0^2\hbar}{m} = \frac{16E_L\hbar}{m}\left(\frac{mE_c}{2\hbar}\right) = 8E_L E_c$$

$$\omega_0 = \sqrt{8E_L E_c}$$

then

$$g = 2k_0\sqrt{\frac{\hbar\omega_0}{2m}} = 2\sqrt{\frac{k_0^2\hbar\omega_0}{2m}} = \sqrt{\sqrt{8E_L E_c}E_c}$$

Bibliography

[1] I. I. Rabi. 'On the process of space quantization'. In: *Physical Review* 49.3 (1936), p. 324 (cit. on p. 1).

[2] I I Rabi, J R Zacharias, and S Millman. 'Space quantization in a gyrating magnetic field'. In: *Physical Review* 51.7 (1937), p. 652 (cit. on p. 1).

[3] Felix Bloch and Arnold Siegert. 'Phys. Rev.' In: 57 (1940), p. 522 (cit. on p. 1).

[4] E. T. Jaynes and F. W. Cummings. 'Comparison of quantum and semiclassical radiation theories with application to the beam maser'. In: *Proceedings of the IEEE* 51.1 (1963), p. 89 (cit. on pp. 1, 28).

[5] P. L. Knight and P. W. Milonni. 'The Rabi frequency in optical spectra'. In: *Physics Reports* 66 (1980), p. 21 (cit. on p. 1).

[6] B. W. Shore and P. L. Knight. 'The Jaynes-Cummings model'. In: *Journal of Modern Optics* 40 (1993), p. 1195 (cit. on p. 1).

[7] J. H. Eberly, N. Narozhny, and J. Sanchez-Mondragon. 'Periodic spontaneous collapse and revival in a simple quantum model'. In: *Physical Review Letters* 44 (1980), p. 1323 (cit. on p. 1).

[8] H. Häffner, C.F. Roos, and R. Blatt. 'Quantum computing with trapped ions'. In: *Physics Reports* 469.4 (2008), pp. 155–203 (cit. on p. 1).

[9] P. Forn-Díaz, L. Lamata, E. Rico, J. Kono, and E. Solano. 'Ultrastrong coupling regimes of light-matter interaction'. In: *Rev. Mod. Phys.* 91 (2 June 2019), p. 025005 (cit. on p. 1).

[10] N. K. Langford, R. Sagastizabal, M. Kounalakis, C. Dickel, A. Bruno, F. Luthi, D. J. Thoen, A. Endo, and L. Dicarlo. 'Experimentally simulating the dynamics of quantum light and matter at deep-strong coupling'. In: *Nature Communications* 8 (2017), p. 1715 (cit. on p. 1).

[11] D. Marković, S. Jezouin, Q. Ficheux, S. Fedortchenko, S. Felicetti, T. Coudreau, P. Milman, Z. Leghtas, and B. Huard. 'Demonstration of an effective ultrastrong coupling between two oscillators'. In: *Physical Review Letters* 121 (2018), p. 040505 (cit. on p. 1).

[12] C. Ciuti, G. Bastard, and I. Carusotto. 'Quantum vacuum properties of the intersubband cavity polariton field'. In: *Physical Review B* 72 (2005), p. 115303 (cit. on p. 1).

[13] J. Casanova, G. Romero, I. Lizuain, J. J. García-Ripoll, and E. Solano. 'Deep strong coupling regime of the Jaynes-Cummings model'. In: *Physical Review Letters* 105 (2010), p. 263603 (cit. on p. 1).

[14] B. Peropadre, P. Forn-Díaz, E. Solano, and J. J. García-Ripoll. 'Switchable ultrastrong coupling in circuit QED'. In: *Physical Review Letters* 105 (2010), p. 023601 (cit. on p. 1).

[15] Daniel Braak. 'Symmetries in the Quantum Rabi Model'. In: *Symmetry* 11.10 (2019) (cit. on pp. 1, 29).

[16] D. Braak. 'Integrability of the Rabi model'. In: *Physical Review Letters* 107 (2011), p. 100401 (cit. on p. 1).

[17] A. A. Anappara and et al. 'Signatures of the ultrastrong light-matter coupling regime'. In: *Physical Review B* 79 (2009), p. 201303 (cit. on p. 1).

[18] G. Günter and et al. 'Sub-cycle switch-on of ultrastrong light–matter interaction'. In: *Nature* 458 (2009), p. 178 (cit. on p. 1).

[19] Y. Todorov and et al. 'Ultrastrong light-matter coupling regime with polariton dots'. In: *Physical Review Letters* 105 (2010), p. 196402 (cit. on p. 1).

[20] T. Schwartz, J. A. Hutchison, C. Genet, and T. W. Ebbesen. 'Reversible switching of ultrastrong light-molecule coupling'. In: *Physical Review Letters* 106 (2011), p. 196405 (cit. on p. 1).

[21] P. Forn-Díaz and et al. 'Observation of the Bloch-Siegert Shift in a Qubit-Oscillator System in the Ultrastrong Coupling Regime'. In: *Physical Review Letters* 105 (2010), p. 237001 (cit. on pp. 1, 29).

[22] D. Z. Rossatto, C. J. Villas-Bôas, M. Sanz, and E. Solano. 'Spectral Classification of Coupling Regimes in the Quantum Rabi Model'. In: *Physical Review A* 96 (2017), p. 013849 (cit. on pp. 1, 29).

[23] F. Yoshihara and et al. 'Superconducting qubit–oscillator circuit beyond the ultrastrong-coupling regime'. In: *Nature Physics* 13 (2017), p. 44 (cit. on p. 1).

[24] D. Lv and et al. 'Quantum simulation of the quantum Rabi model in a trapped ion'. In: *Physical Review X* 8 (2018), p. 021027 (cit. on p. 1).

[25] A. Dareau, Y. Meng, P. Schneeweiss, and A. Rauschenbeutel. 'Observation of ultrastrong spin-motion coupling for cold atoms in optical microtraps'. In: *Physical Review Letters* 121 (2018), p. 253603 (cit. on p. 1).

[26] M. Halbhuber and et al. 'Non-adiabatic stripping of a cavity field from electrons in the deep-strong coupling regime'. In: *Nature Photonics* 14 (2020), p. 675 (cit. on p. 1).

[27] J. Koch, G.R. Hunanyan, and T. et al. Ockenfels. 'Quantum Rabi dynamics of trapped atoms far in the deep strong coupling regime'. In: *Nature Communications* 14 (2023), p. 954 (cit. on pp. 2, 33, 37, 80).

[28] Geram R. Hunanyan, Johannes Koch, Stefanie Moll, Enrique Rico, Enrique Solano, and Martin Weitz. *Periodic quantum Rabi model with cold atoms at deep strong coupling*. 2023 (cit. on p. 2).

[29] R. Feynman. ‘Path integrals and the Schrödinger equation in quantum mechanics’. In: *International Journal of Theoretical Physics* 21.6/7 (1982), pp. 467–488 (cit. on p. 2).

[30] Thomas Monz, Philipp Schindler, Julio T. Barreiro, Michael Chwalla, Daniel Nigg, William A. Coish, Maximilian Harlander, Wolfgang Hänsel, Markus Hennrich, and Rainer Blatt. ‘14-Qubit Entanglement: Creation and Coherence’. In: *Phys. Rev. Lett.* 106 (13 Mar. 2011), p. 130506 (cit. on p. 2).

[31] J. I. Cirac and P. Zoller. ‘Quantum Computations with Cold Trapped Ions’. In: *Phys. Rev. Lett.* 74 (20 May 1995), pp. 4091–4094 (cit. on p. 2).

[32] I. Pogorelov et al. ‘Compact Ion-Trap Quantum Computing Demonstrator’. In: *PRX Quantum* 2 (2 June 2021), p. 020343 (cit. on p. 2).

[33] D. Kielpinski, C. Monroe, and D. Wineland. ‘Architecture for a large-scale ion-trap quantum computer’. In: *Nature* 417.6890 (2002), pp. 709–711 (cit. on p. 2).

[34] J. Kelly, R. Barends, A. Fowler, and et al. ‘State preservation by repetitive error detection in a superconducting quantum circuit’. In: *Nature* 519.7541 (2015), pp. 66–69 (cit. on p. 2).

[35] F. Arute, K. Arya, R. Babbush, and et al. ‘Quantum supremacy using a programmable superconducting processor’. In: *Nature* 574.7779 (2019), pp. 505–510 (cit. on p. 2).

[36] Vladimir E. Manucharyan, Jens Koch, Leonid I. Glazman, and Michel H. Devoret. ‘Fluxonium: Single Cooper-Pair Circuit Free of Charge Offsets’. In: *Science* 326 (2009), pp. 113–116 (cit. on pp. 2, 45, 90).

[37] A.A. Houck, J. Koch, M.H. Devoret, and et al. ‘Life after charge noise: recent results with transmon qubits’. In: *Quantum Information Processing* 8.1 (2009), pp. 105–115 (cit. on p. 2).

[38] R. Barends et al. ‘Coherent Josephson Qubit Suitable for Scalable Quantum Integrated Circuits’. In: *Phys. Rev. Lett.* 111 (8 Aug. 2013), p. 080502 (cit. on p. 2).

[39] Shicheng Xu, Anup L. Dadlani, Shinjita Acharya, Peter Schindler, and Fritz B. Prinz. ‘Oscillatory barrier-assisted Langmuir–Blodgett deposition of large-scale quantum dot monolayers’. In: *Applied Surface Science* 367 (2016), pp. 500–506 (cit. on p. 2).

[40] R. Ashoori. ‘Electrons in artificial atoms’. In: *Nature* 379.6563 (1996), pp. 413–419 (cit. on p. 2).

[41] P. Senellart, G. Solomon, and A. White. ‘High-performance semiconductor quantum-dot single-photon sources’. In: *Nature Nanotechnology* 12.11 (2017), pp. 1026–1039 (cit. on p. 2).

[42] J. Cui, Y.E. Panfil, S. Koley, and et al. ‘Colloidal quantum dot molecules manifesting quantum coupling at room temperature’. In: *Nature Communications* 10 (2019) (cit. on p. 2).

[43] U. Banin, Y. Cao, D. Katz, and et al. ‘Identification of atomic-like electronic states in indium arsenide nanocrystal quantum dots’. In: *Nature* 400.6739 (1999), pp. 542–544 (cit. on p. 2).

[44] Jan Klaers, Julian Schmitt, Frank Vewinger, and Martin Weitz. 'Bose-Einstein condensation of photons in an optical microcavity'. In: *Nature* 468 (Nov. 2010), pp. 545–8 (cit. on pp. 2, 5).

[45] M. B. Dahan, E. Peik, J. Reichel, Y. Castin, and C. Salomon. 'Bloch oscillations of atoms in an optical potential'. In: *Physical Review Letters* 76.25 (1996), pp. 4508–4511 (cit. on p. 2).

[46] T. Salger, C. Grossert, S. Kling, and M. Weitz. 'Klein tunneling of a quasirelativistic Bose-Einstein condensate in an optical lattice'. In: *Physical Review Letters* 107.24 (2011), p. 240401 (cit. on p. 2).

[47] M. Leder, C. Grossert, and M. Weitz. 'Veselago lensing with ultracold atoms in an optical lattice'. In: *Nature Communications* 5 (2014), p. 4019 (cit. on p. 2).

[48] M. Leder, C. Grossert, F. Hannibal, S. Christ, I. Bloch, and M. Weitz. 'Real-space imaging of a topologically protected edge state with ultracold atoms in an amplitude-chirped optical lattice'. In: *Nature Communications* 7 (2016), p. 13112 (cit. on p. 2).

[49] W Hofstetter and T Qin. 'Quantum simulation of strongly correlated condensed matter systems'. In: *Journal of Physics B: Atomic, Molecular and Optical Physics* 51.8 (Mar. 2018), p. 082001 (cit. on p. 2).

[50] M. Greiner, O. Mandel, T. Esslinger, T. W. Hänsch, and I. Bloch. 'Quantum phase transition from a superfluid to a Mott insulator in a gas of ultracold atoms'. In: *Nature* 415.6867 (2002), pp. 39–44 (cit. on p. 2).

[51] Bo-Ye Sun, Nathan Goldman, Monika Aidelsburger, and Marin Bukov. 'Engineering and Probing Non-Abelian Chiral Spin Liquids Using Periodically Driven Ultracold Atoms'. In: *PRX Quantum* 4 (2 May 2023), p. 020329 (cit. on p. 2).

[52] M. Weitz and et al. 'Optical multiphoton lattices'. In: *Physical Review A* 70.4 (2004), p. 043414 (cit. on pp. 2, 20, 23).

[53] J. Koch. 'Quanten-Rabi Dynamik ultrakalter Atome im Bereich der tiefen starken Kopplung'. PhD thesis. Rheinische Friedrich-Wilhelms-Universität Bonn, 2022 (cit. on pp. 2, 27, 33, 38, 49, 59, 60, 67, 75, 79, 86, 87).

[54] R.K. Pathria. *Statistical Mechanics*. International series of monographs in natural philosophy. Elsevier Science Technology Books, 1972 (cit. on p. 5).

[55] Franco Dalfovo, Stefano Giorgini, Lev P. Pitaevskii, and Sandro Stringari. 'Theory of Bose-Einstein condensation in trapped gases'. In: *Rev. Mod. Phys.* 71 (3 Apr. 1999), pp. 463–512 (cit. on pp. 5, 7–9).

[56] C. J. Pethick and H. Smith. *Bose–Einstein Condensation in Dilute Gases*. 2nd ed. Cambridge University Press, 2008 (cit. on p. 5).

[57] Bose. 'Plancks Gesetz und Lichtquantenhypothese'. In: *Zeitschrift für Physik* 26 (1924), pp. 178–181 (cit. on p. 5).

[58] A. Einstein. 'Quantentheorie des einatomigen idealen Gases'. In: *Albert Einstein: Akademie-Vorträge*. John Wiley Sons, Ltd, 2005, pp. 237–244 (cit. on p. 5).

[59] N. N. Bogolyubov. ‘On the theory of superfluidity’. In: *J. Phys. (USSR)* 11 (1947), pp. 23–32 (cit. on p. 7).

[60] E. P. Gross. ‘Structure of a quantized vortex in boson systems’. In: *Il Nuovo Cimento* 20.3 (May 1961), pp. 454–477 (cit. on p. 8).

[61] Lev P Pitaevskii. ‘Vortex lines in an imperfect Bose gas’. In: *Sov. Phys. JETP* 13.2 (1961), pp. 451–454 (cit. on p. 8).

[62] John Weiner, Vanderlei S. Bagnato, Sergio Zilio, and Paul S. Julienne. ‘Experiments and theory in cold and ultracold collisions’. In: *Rev. Mod. Phys.* 71 (1 Jan. 1999), pp. 1–85 (cit. on p. 8).

[63] Frank Pobell. *Matter and Methods at Low Temperatures*. Springer, 2007 (cit. on p. 10).

[64] Aron E Leanhardt, Thomas A Pasquini, Michele Saba, André Schirotzek, Yong-il Shin, David Kielpinski, David E Pritchard, and Wolfgang Ketterle. ‘Cooling Bose-Einstein condensates below 500 picokelvin’. In: *Science* 301.5639 (2003), pp. 1513–1515 (cit. on p. 10).

[65] Tim Kovachy, Jason M. Hogan, Alex Sugarbaker, Susannah M. Dickerson, Christine A. Donnelly, Chris Overstreet, and Mark A. Kasevich. ‘Matter Wave Lensing to Picokelvin Temperatures’. In: *Phys. Rev. Lett.* 114 (14 Apr. 2015), p. 143004 (cit. on p. 10).

[66] T.W. Hänsch and A.L. Schawlow. ‘Cooling of gases by laser radiation’. In: *Optics Communications* 13.1 (1975), pp. 68–69 (cit. on p. 10).

[67] Steven Chu, L. Hollberg, J. E. Bjorkholm, Alex Cable, and A. Ashkin. ‘Three-dimensional viscous confinement and cooling of atoms by resonance radiation pressure’. In: *Phys. Rev. Lett.* 55 (1 July 1985), pp. 48–51 (cit. on p. 10).

[68] D. A. Steck. *Rubidium 87 D Line Data*. `http://steck.us/alkalidata`. (Besucht am 25. 08. 2021). 2021 (cit. on pp. 12, 50, 52, 53).

[69] A. A. Radzig and B. M. Smirnov. *Reference data on atoms, molecules and ions*. Springer, 1985 (cit. on p. 11).

[70] M. P. Bradley et al. ‘Penning Trap Measurements of the Masses of 133Cs, 87,85Rb, and 23Na’. In: *Phys. Rev. Lett.* 83.22 (1999), p. 4510 (cit. on p. 12).

[71] C. Adams and E. Riis. ‘Laser cooling and trapping of neutral atoms’. In: *Progress in Quantum Electronics* 21.1 (1997), pp. 1–79 (cit. on p. 12).

[72] A. Ashkin. ‘Acceleration and trapping of particles by radiation pressure’. In: *Physical Review Letters* 24.4 (1970), p. 156 (cit. on p. 13).

[73] A. Ashkin. ‘Atomic-beam deflection by resonance-radiation pressure’. In: *Physical Review Letters* 25.19 (1970), p. 1321 (cit. on p. 13).

[74] J. Dalibard and C. Cohen-Tannoudji. ‘Dressed-atom approach to atomic motion in laser light: the dipole force revisited’. In: *Journal of the Optical Society of America B* 2.11 (1985), pp. 1707–1720 (cit. on p. 13).

[75] R. Grimm, M. Weidemüller, and Y. B. Ovchinnikov. 'Optical dipole traps for neutral atoms'. In: *Advances in Atomic, Molecular, and Optical Physics* 42 (2000), p. 95 (cit. on pp. 13, 14, 17, 18).

[76] A. Khadjavi, A. Lurio, and W. Happer. 'Stark Effect in the Excited States of Rb, Cs, Cd, and Hg'. In: *Physical Review* 167 (1968), pp. 128–135 (cit. on p. 13).

[77] Hendrik Antoon Lorentz. *The Theory of Electrons and Its Applications to the Phenomena of Light and Radiant Heat*. Vol. Bd. 29. OCLC 535812. New York; Leipzig: B.G. Teubner, 1909 (cit. on p. 14).

[78] J. D. Jackson. *Classical Electrodynamics*. New York: Wiley, 1962 (cit. on p. 14).

[79] J. Larmor. 'LXIII. On the theory of the magnetic influence on spectra; and on the radiation from moving ions'. In: *Philosophical Magazine* 5.44 (1897), pp. 503–512 (cit. on p. 14).

[80] L. Allen and J. Eberly. *Optical Resonance and Two-Level Atoms*. New York: Wiley, 1975 (cit. on p. 15).

[81] R. Shankar. *Principles of Quantum Mechanics*. Springer, 1994 (cit. on p. 16).

[82] H. Haken and H. C. Wolf. *Atom-und Quantenphysik - Eine Einführung in die experimentellen und theoretischen Grundlagen*. Springer, 1980 (cit. on p. 17).

[83] H. F. Hess et al. 'Magnetic trapping of spin-polarized atomic hydrogen'. In: *Physical Review Letters* 59.6 (June 1987), p. 0672 (cit. on p. 18).

[84] C. S. Adams et al. 'Evaporative cooling in a crossed dipole trap'. In: *Physical Review Letters* 74.16 (1995), p. 3577 (cit. on p. 18).

[85] Felix Bloch. 'Über die Quantenmechanik der Elektronen in Kristallgittern'. In: *Zeitschrift für Physik* 52.7-8 (1929), pp. 555–600 (cit. on pp. 19, 23).

[86] Charles Kittel. *Einführung in die Festkörperphysik*. Oldenbourg Verlag, 2013 (cit. on p. 19).

[87] Oliver Morsch and Markus Oberthaler. 'Dynamics of Bose-Einstein condensates in optical lattices'. In: *Reviews of Modern Physics* 78.1 (2006), p. 179 (cit. on p. 19).

[88] Immanuel Bloch and Markus Greiner. 'Exploring quantum matter with ultracold atoms in optical lattices'. In: *Advances in Atomic, Molecular, and Optical Physics* 52.1 (2005), p. 1 (cit. on p. 20).

[89] S. Fölling and et al. 'Direct observation of second-order atom tunnelling'. In: *Nature* 448.7156 (2007), pp. 1029–1032 (cit. on p. 20).

[90] G. Ritt. 'Fourier-Synthese von asymmetrischen optischen Potentialen für Atome'. PhD thesis. Universität Tübingen, 2007 (cit. on p. 21).

[91] I. V. Pechenezhskiy, R. A. Mencia, L. B. Nguyen, et al. 'The superconducting quasicharge qubit'. In: *Nature* 585 (2020), pp. 368–371 (cit. on pp. 27, 42, 45, 48).

[92] Christopher Gerry and Peter Knight. *Introductory Quantum Optics*. Cambridge University Press, 2004 (cit. on p. 27).

[93] R. Miller, T. E. Northup, K. M. Birnbaum, A. Boca, A. D. Boozer, and H. J. Kimble. 'Trapped Atoms in Cavity QED: Coupling Quantized Light and Matter'. In: *J. Phys. B* 38 (2005), S551 (cit. on p. 29).

[94] H. Walther, B. T. H. Varcoe, B. G. Englert, and T. Becker. 'Cavity Quantum Electrodynamics'. In: *Rep. Prog. Phys.* 69 (2006), p. 1325 (cit. on p. 29).

[95] J.-M. Raimond and S. Haroche. *Exploring the Quantum: Atoms, Cavities, and Photons*. Oxford: Oxford University Press, 2006, pp. 151–161 (cit. on p. 29).

[96] H. Ritsch, P. Domokos, F. Brennecke, and T. Esslinger. 'Cold Atoms in Cavity-Generated Dynamical Optical Potentials'. In: *Rev. Mod. Phys.* 85 (2013), p. 553 (cit. on p. 29).

[97] R. Hanson, L. P. Kouwenhoven, J. R. Petta, S. Tarucha, and L. M. K. Vandersypen. 'Spins in Few-Electron Quantum Dots'. In: *Rev. Mod. Phys.* 79 (2007), p. 1217 (cit. on p. 29).

[98] A. Wallraff, D. I. Schuster, A. Blais, L. Frunzio, R.-S. Huang, J. Majer, S. Kumar, S. M. Girvin, and R. J. Schoelkopf. 'Strong Coupling of a Single Photon to a Superconducting Qubit Using Circuit Quantum Electrodynamics'. In: *Nature (London)* 431 (2004), p. 162 (cit. on p. 29).

[99] M. H. Devoret and R. J. Schoelkopf. 'Superconducting Circuits for Quantum Information: An Outlook'. In: *Science* 339 (2013), p. 1169 (cit. on p. 29).

[100] D. M. Meekhof, C. Monroe, B. E. King, W. M. Itano, and D. J. Wineland. 'Generation of Nonclassical Motional States of a Trapped Atom'. In: *Phys. Rev. Lett.* 76 (1996), p. 1796 (cit. on p. 29).

[101] D. Leibfried, R. Blatt, C. Monroe, and D. J. Wineland. 'Quantum Dynamics of Single Trapped Ions'. In: *Rev. Mod. Phys.* 75 (2003), p. 281 (cit. on p. 29).

[102] H. Häffner, C. F. Roos, and R. Blatt. 'Quantum Computing with Trapped Ions'. In: *Phys. Rep.* 469 (2008), p. 155 (cit. on p. 29).

[103] D. Lv, S. An, M. Um, J. Zhang, J.-N. Zhang, M. S. Kim, and K. Kim. 'Reconstruction of the Jaynes-Cummings Field State of Ionic Motion in a Harmonic Trap'. In: *Phys. Rev. A* 95 (2017), p. 043813 (cit. on p. 29).

[104] R. Graham and M. Höhnerbach. 'Two-state system coupled to a boson mode: quantum dynamics and classical approximations'. In: *Zeitschrift für Physik B Condensed Matter* 57 (1984), p. 233 (cit. on p. 29).

[105] Daniel Z. Rossatto, Celso J. Villas-Bôas, Mikel Sanz, and Enrique Solano. 'Spectral classification of coupling regimes in the quantum Rabi model'. In: *Phys. Rev. A* 96 (1 July 2017), p. 013849 (cit. on p. 31).

[106] A. F. Kockum, A. Miranowicz, S. De Liberato, S. Savasta, and F. Nori. 'Ultrastrong Coupling between Light and Matter'. In: *Nature Reviews Physics* 1 (2019), p. 19 (cit. on p. 29).

[107] M.-J. Hwang, R. Puebla, and M. B. Plenio. 'Quantum phase transition and universal dynamics in the Rabi model'. In: *Physical Review Letters* 115.18 (2015), p. 180404 (cit. on pp. 30, 81, 89).

[108] J. Casanova, G. Romero, I. Lizuain, J. J. García-Ripoll, and E. Solano. 'Deep Strong Coupling Regime of the Jaynes-Cummings Model'. In: *Phys. Rev. Lett.* 105 (26 Dec. 2010), p. 263603 (cit. on p. 31).

[109] S. Felicetti and et al. 'Quantum Rabi model in the Brillouin zone with ultracold atoms'. In: *Physical Review A* 95.1 (2017), p. 013827 (cit. on pp. 35, 86, 89, 93).

[110] Immanuel Bloch, Jean Dalibard, and Wilhelm Zwerger. 'Many-body physics with ultracold gases'. In: *Rev. Mod. Phys.* 80 (3 July 2008), pp. 885–964 (cit. on p. 41).

[111] Long B. Nguyen, Gerwin Koolstra, Yosep Kim, Alexis Morvan, Trevor Chistolini, Shraddha Singh, Konstantin N. Nesterov, Christian Jünger, Larry Chen, Zahra Pedramrazi, Bradley K. Mitchell, John Mark Kreikebaum, Shruti Puri, David I. Santiago, and Irfan Siddiqi. 'Blueprint for a High-Performance Fluxonium Quantum Processor'. In: *PRX Quantum* 3 (3 Aug. 2022), p. 037001 (cit. on p. 45).

[112] T. Salger. 'Quantentransport ultrakalter Atome in Fourier-synthetisierten optischen Gitterpotentialen'. PhD thesis. Rheinische Friedrich-Wilhelms-Universität Bonn, 2010 (cit. on p. 49).

[113] M. Leder. 'Quantensimulation von relativistischen Effekten mit ultrakalten Atomen in variablen optischen Gitterpotentialen'. PhD thesis. Rheinische Friedrich-Wilhelms-Universität Bonn, 2016 (cit. on pp. 49, 53, 58, 59).

[114] C. Grossert. 'Atomarer Transport und die Kontrolle von Transportresonanzen in optischen Gitterpotentialen'. PhD thesis. Rheinische Friedrich-Wilhelms-Universität Bonn, 2015 (cit. on pp. 49, 59).

[115] E. Catanzaro, T. J. Murphy, E. Garner, and W.-R. Shields. 'Absolute isotopic abundance ratio and atomic weight of terrestrial rubidium'. In: *Journal of Research of the National Bureau of Standards. Section A, Physics and Chemistry* 73 (1969), p. 511 (cit. on p. 50).

[116] I. M. Villa, P. De Bièvre, N. Holden, and P. Renne. 'IUPAC-IUGS recommendation on the half-life of 87Rb'. In: *Geochimica et Cosmochimica Acta* 164 (2015), p. 382 (cit. on p. 50).

[117] X. Baillard, A. Gauguet, S. Bize, P. Lemonde, Ph. Laurent, A. Clairon, and P. Rosenbusch. 'Interference-filter-stabilized external-cavity diode lasers'. In: *Optics Communications* 266.2 (2006), pp. 609–613 (cit. on p. 51).

[118] P. Pokrowsky, W. Zapka, F. Chu, and G. Bjorklund. 'High frequency wavelength modulation spectroscopy with diode lasers'. In: *Optics Communications* 44 (1983), p. 175 (cit. on p. 51).

[119] G. Ritt. 'Fourier-Synthese von asymmetrischen optischen Potentialen für Atome'. PhD thesis. Universität Tübingen, 2007 (cit. on pp. 51, 53).

[120] L. Sitta. ‘Observation of an edge state in ultra cold atoms with spatially variable optical lattice potentials’. MA thesis. Rheinische Friedrich-Wilhelms-Universität Bonn, 2015 (cit. on p. 54).

[121] S. Z. Hassan. ‘Realization of the Quantum Rabi Model with Ultracold Rubidium Atoms in an Optical Lattice’. MA thesis. Rheinische Friedrich-Wilhelms-Universität Bonn, 2017 (cit. on p. 56).

[122] J. Plumhof. ‘Bose-Einstein-Kondensation von Rubidiumatomen in variablen optischen Gittern’. Diplomarbeit. Rheinische Friedrich-Wilhelms-Universität Bonn, 2008 (cit. on p. 57).

[123] H. Haken and H. C. Wolf. *Atom- und Quantenphysik: Einführung in die experimentellen und theoretischen Grundlagen*. Springer-Verlag, 2001, p. 209 (cit. on p. 58).

[124] K. O’hara, M. E. Gehm, S. Granade, and J. Thomas. ‘Scaling laws for evaporative cooling in time-dependent optical traps’. In: *Physical Review A* 64 (2001), p. 051403 (cit. on p. 61).

[125] F. A. Wolf, M. Kollar, and D. Braak. ‘Exact real-time dynamics of the quantum Rabi model’. In: *Physical Review A* 85 (2012), p. 053817 (cit. on p. 77).

[126] M. Heyl. ‘Dynamical quantum phase transitions: a review’. In: *Reports on Progress in Physics* 81 (2018), p. 054001 (cit. on pp. 81, 89).

[127] Y.-T. Yang and H.-G. Luo. ‘Characterizing superradiant phase of the quantum rabi model’. In: *Chinese Physics Letters* 40 (2023), p. 020502 (cit. on pp. 81, 89).

[128] ML Cai, ZD Liu, WD Zhao, et al. ‘Observation of a quantum phase transition in the quantum Rabi model with a single trapped ion’. In: *Nature Communications* 12 (2021) (cit. on p. 89).

[129] L. Lamata, A. Parra-Rodriguez, M. Sanz, and E. Solano. ‘Digital-analog quantum simulations with superconducting circuits’. In: *Advances in Physics: X* 3 (2018), p. 1457981 (cit. on p. 90).

Danksagungen

An dieser Stelle möchte ich mich bei den Menschen bedanken, die mich in den letzten fünf Jahren während meiner Doktorarbeit begleitet haben. Ich hatte die Gelegenheit, sowohl fachlich als auch persönlich enorm zu wachsen, zu erleben und zu entdecken. Die Verfassung dieser Arbeit wäre ohne die Unterstützung der folgenden Personen nicht möglich gewesen:
Zunächst möchte ich mich bei Prof. Dr. Martin Weitz für die Möglichkeit bedanken, an diesem spannenden Projekt arbeiten zu dürfen. Des Weiteren möchte ich einen besonderen Dank für die Übernahme des Zweitgutachtens an Herrn Prof. Dr. Michael Köhl aussprechen.
Ein herzliches Dankeschön gilt auch der gesamten Arbeitsgruppe, die sich natürlich im Laufe dieser fünf Jahre der Doktorarbeit zwar verändert hat, bei der man dennoch stets von Menschen umgeben war, mit denen die Pausen aber auch die Arbeitsstunden gerne verbracht wurden. Besonders hervorheben möchte ich meinen langjährigen Laborpartner Dr. Johannes Koch, der sich nicht nur durch seine herausragenden naturwissenschaftlichen Fähigkeiten auszeichnet, sondern vor allem dank seiner zwischenmenschlichen Kompetenz mittlerweile zu einem guten Freund geworden ist. Weiterer Dank gebührt natürlich auch anderen Kolleginnen und Kollegen, wie Stefanie Moll, die an unserem Experiment vorerst als Masterstudentin angefangen hat, um nun als Doktorandin weiterzuforschen.
Der wohl wichtigste Dank gebührt meiner Familie, ohne deren bedingungslose Unterstützung, ihre Liebe und ihr Vertrauen, diese Dissertation nicht möglich gewesen wäre. Ihre Opferbereitschaft und Ermutigung machen diese Arbeit nicht nur zu meinem, sondern auch zu ihrem Erfolg.